



HAL
open science

A multicellular actin star network underpins epithelial organization and connectivity

Barai Amlan, Soleilhac Matis, Xi Wang, Lin Shao-Zhen, Karnat Marc, Bazellières Elsa, Richelme Sylvie, Berrebi Dominique, Rümmele Frank, Théry Manuel, et al.

► To cite this version:

Barai Amlan, Soleilhac Matis, Xi Wang, Lin Shao-Zhen, Karnat Marc, et al.. A multicellular actin star network underpins epithelial organization and connectivity. *BioRxiv*, 2024, 10.1101/2024.07.26.605277 . hal-04778200v1

HAL Id: hal-04778200

<https://hal.science/hal-04778200v1>

Submitted on 12 Nov 2024 (v1), last revised 22 Nov 2024 (v2)

HAL is a multi-disciplinary open access archive for the deposit and dissemination of scientific research documents, whether they are published or not. The documents may come from teaching and research institutions in France or abroad, or from public or private research centers.

L'archive ouverte pluridisciplinaire **HAL**, est destinée au dépôt et à la diffusion de documents scientifiques de niveau recherche, publiés ou non, émanant des établissements d'enseignement et de recherche français ou étrangers, des laboratoires publics ou privés.

Copyright

1 **A multicellular actin star network underpins epithelial organization** 2 **and connectivity**

3
4

5 **AUTHORS**

6

7 Barai Amlan ^{1,2,3} &, Soleilhac Matis ^{1,2,3} &, Xi Wang ³, Lin Shao-Zhen ⁴ #, Karnat Marc ⁴ #,
8 Bazellères Elsa ¹, Richelme Sylvie ¹, Berrebi Dominique ^{5,6}, Rümmele Frank ⁷, Théry Manuel
9 ^{8,9}, Rupprecht Jean-François ⁴ and Delacour Delphine ^{1,2,3*}

10

11 ¹ Aix Marseille Université, CNRS, UMR 7288, IBDM, Turing Center for Living Systems,
12 Marseille, France

13 ² Equipe labellisée Fondation ARC

14 ³ Université Paris Cité, CNRS, Institut Jacques Monod, F-75013 Paris, France

15 ⁴ Aix Marseille Université, CNRS, CPT (UMR 7332), Turing Centre for Living Systems,
16 Marseille, France

17 ⁵ Paediatric Anatomic-Pathology Department, Hôpital Necker-Enfants Malades, Sorbonne
18 Paris Cité, F-75015 Paris, France

19 ⁶ UFR de Médecine, Université Paris Cité, France

20 ⁷ Paediatric Gastroenterology Department, Hôpital Necker-Enfants Malades, Sorbonne Paris
21 Cité, F-75015 Paris, France

22 ⁸ Université Paris Sciences et Lettres, CEA/CNRS, UMR8132, Ecole Supérieure de Physique
23 et Chimie Industrielles de la Ville de Paris, Institut Pierre Gilles De Gennes, Paris France

24 ⁹ Université Grenoble-Alpes, CEA/INRA/CNRS, UMR5168, Interdisciplinary Research
25 Institute of Grenoble, Grenoble, France

26 &# Authors participated equivalently

27

28

29 * Corresponding author:

30 delphine.delacour@univ-amu.fr

31

32

33 **KEYWORDS:** epithelial morphogenesis, actomyosin, cell shape, supracellular cytoskeleton

34

35

36 **SUMMARY**

37 Epithelial tissues serve as physical barriers against various external pressures yet remarkably
38 maintain structural stability. Various cellular apparatus including bicellular junction and
39 actomyosin network contribute to the epithelial integrity, packing and remodelling. Although
40 their role in morphogenetic and mechanical processes have been extensively studied during
41 embryogenesis and disease development, their synergistic effects in maintaining tissue
42 organization and connection remain poorly understood. In this study, we discovered a tissue-
43 scale actomyosin network connected through bicellular junctions and manifested in the villi of
44 adult murine intestinal tissue. Later we reproduced such supracellular structure in the
45 differentiated compartment of *ex vivo* intestinal epithelium model. The self-organized
46 actomyosin networks comprised individual actin nodes in each hexagonal cell at the epithelial
47 base with six radial actin branches, presenting an 'actin star' unit. The repeated units were
48 connected through the bicellular junctions, forming a large, multicellular array covering the
49 differentiated domains. Functionally, actin stars contribute to epithelial morphological stability
50 by maintaining cell hexagonality and packing, thereby preserving the solid-like order of the
51 epithelium. Laser ablation experiments validate a modified vertex theoretical model that
52 connects the emergence of such solid-like order to the onset of tension along the actin star
53 branches. Actin stars also acted as locks at the basal side minimizing protrusive activity in the
54 epithelial layer, hindering cell migration and disorganization of the epithelial tissue. The large
55 actomyosin array also enhanced the long-range connectivity that ensure overall tissue
56 integrity. Altogether, the supracellular actin star network constitutes a basal biomechanical
57 apparatus coordinating epithelial tissue stability and organization.

58

59 INTRODUCTION

60

61 The actomyosin network ensures numerous morphogenetic processes through the generation
62 and transmission of tension forces ^{1,2,3}, which are primarily facilitated by the presence and
63 activation of the molecular motor myosin-II (non-muscle myosin-II, NM-II) along actin filaments
64 ⁴. The pivotal functions of the contractile apparatus are particularly emphasized in epithelial
65 tissues, which form resilient cellular assemblies lining the body surfaces. Monolayered
66 epithelial behave as crucial interfaces between the internal milieu and the external
67 environment, orchestrating essential physiological processes such as protection, secretion,
68 and absorption. Thus, the preservation of epithelial tissue integrity stands as a paramount
69 concern. Any disruptions in this integrity can yield profound consequences, including
70 compromised organ formation and functionality, and potential tumorigenesis ^{5,6}.

71 Epithelial monolayers possess distinct characteristics, marked by the polarization of densely
72 packed cells into cohesive sheets. Hence, hexagonal packing represents an efficient way of
73 covering a surface and distributing force equally among epithelial cells ⁷. Moreover, cell
74 polarization gives rise to discrete apical and basolateral domains, each endowed with unique
75 molecular compositions and functions that dictate directional epithelial functions ^{8,6}. To
76 maintain epithelial monolayer cohesion and coordination, cells establish robust intercellular
77 junctions, notably adherens junctions mediated by cadherins and linked to actomyosin
78 network via catenins, particularly enriched in the actin belt on apical side ^{9,10,11}. It is now clear
79 that the apical coupling of E-cadherin, catenin and actomyosin is a powerful component for
80 tissue mechanics, as it serves as a mechanosensor unit by responding to applied forces ^{11,12,13}.
81 Therefore, the integration of mechanical information at the tissue level, achieved through
82 adaptation of the actomyosin cytoskeleton or junctions themselves, is a major component of
83 epithelial morphogenesis ^{11,13}. For instance, the apical-medial actomyosin drives apical
84 constriction during mesoderm invagination in *Drosophila* embryos for apical area deformation.
85 Apical constriction allows apical area deformation and ultimately tissue folding through
86 mechanical forces applied on adherens junctions ^{14,15, 16,17,18}. In addition, anisotropic changes
87 of tension along the cell surface control cell deformation that result in cell intercalation. During
88 this process, cells remodel their junctions with neighbouring cells to permit cellular
89 rearrangement during tissue elongation ¹⁹. Altogether, these morphogenetic events directly
90 impact the tissue physical state or tissue fluidity. Tissues in a solid-like state are barely
91 remodelled and able to resist mechanical stress to maintain their architecture, while tissues in
92 a fluid-like state are more prompt to remodelling due to exerted forces ²⁰.

93

94 Here, we used the mammalian intestinal tissue to address mechanisms that control epithelial
95 stability. We revealed the development of a multicellular star-shaped actomyosin lattice in the
96 basal domain of differentiated epithelial cells, that behaves as a new mechanical unit at play
97 for morphological and functional stability in the intestinal tissue.

98

99

100 **RESULTS**

101

102 **Differentiated intestinal epithelial cells develop basal actin star-like structures**

103 The mouse intestinal tissue is a suitable working model for investigating the collective
104 organization of an adult mammalian epithelium. Its functional unit, known as the crypt-villus
105 axis, exhibits distinct compartments: a proliferative domain represented by the crypt (in blue,
106 Figure 1A) and a differentiated domain comprising the villus (in yellow, Figure 1A).
107 Examination of adult mouse villi offered a direct glimpse into the *in vivo* organization of this
108 columnar epithelium (Figure 1B). Through actin labelling in whole-mount tissue, we achieved
109 a clear visualization of the brush border at the apical pole and the basolateral cell contacts
110 (Figure 1B a,d). Notably, our observations revealed a regular actin meshwork located beneath
111 the nuclei on the basal side of epithelial cells along the villus (Figure 1B b-d, Video S1). This
112 meshwork comprised a dense actin core centrally located in each cell basal side, with discrete
113 branches of actin bundles seemingly linking to cell-cell contacts (Figure 1B b-c). These 'star-
114 shaped' actin-based structures were prevalent in the majority of epithelial cells along the villus,
115 excluding those at the villus tip (not shown). Additionally, such 'actin stars' (AcSs) were
116 conspicuously absent in crypt cells (Supplementary Figure 1A-C, Video S2), underscoring
117 their specificity to the intestinal differentiated domain.

118 To delve deeper into the characterization of AcS structures and enhance their spatial
119 resolution, we embarked on reproducing such network within a previously established 2D
120 intestinal organoid culture ²¹. In brief, organoid-derived monolayers were grown on soft
121 substrates made of cross-linked (CL) Matrigel[®] matrix, on which they mimicked the patterning
122 of intestinal tissue *in vitro* (Figure 1C). These include self-organizing crypt-like domains
123 enriched with proliferative cells (i.e. EdU-positive cells, Supplementary Figure 1D), encircled
124 by large villus-like domains with differentiated cells (i.e. cytokeratin-20- and ezrin-positive
125 cells, Supplementary Figure 1E-F) ^{22,23,21}. Within the differentiated domain, we noticed a
126 discernible brush border at the apical surface (Figure 1D a, Supplementary Figure 1F) and a
127 similar star-shaped actin structure at the basal surface of each individual cell (Figure 1D b-c,
128 Supplementary Figure 1F), mirroring our *in vivo* observations (Figure 1Bb-d). AcSs were
129 notably absent in the crypt-like domain, like in the *in vivo* tissue (Figure 1D b,d, Supplementary
130 Figure 1F). Thus, the development of basal AcSs network in the 2D differentiated domains

131 emulated those in the intestinal villi. The development of basal AcSs emerged as a significant
132 hallmark of the differentiated domain in intestinal epithelium, alongside the apical brush
133 border.

134

135 **The assembly of basal actin stars creates an epithelial supracellular cytoskeletal** 136 **network**

137 Further structural analysis using high-resolution microscopy revealed that each epithelial cell
138 of the differentiated domain exhibited a single AcS unit, featuring an actin node positioned at
139 the centre of mass of the basal surface (Figure 2A,C) and accompanied by ~ 6 actin branches
140 extending from it (Figure 2A-B,D). AcS branches measured approximately 5 μm in length
141 (Figure 2E) and exhibited a regular radial organization, with a mean angle of $\alpha = 60 \pm 1.2^\circ$
142 between actin branches (Figure 2F). Moreover, the actin branch was oriented perpendicular
143 ($\beta = 89 \pm 2^\circ$) to an adjacent bicellular contact (Figure 2A,B,F), and appeared to maintain
144 directional continuity with a branch of the neighbouring cell's AcS (Figure 2B, insert).
145 Consequently, the collective disposition of AcSs within the differentiated epithelial layer
146 delineates a triangular network (Figure 2A-B) with AcS playing the role of a Delaunay
147 tessellation of the Voronoi-like cell membrane network.

148 We could not detect canonical focal adhesion components, such as paxillin (Supplementary
149 Figure 2A-B) or talin (not shown) at the AcS branches. While paxillin-positive focal adhesions
150 were detected along actin fibres in cells located at the periphery of crypt-like domains, only
151 faint and small paxillin dot patterns were observed in differentiated cells (Supplementary
152 Figure 2A-B), suggesting that AcS branches are not primarily dedicated to cell-substrate
153 adhesion. Subsequently, we examined the spatial arrangement of AcS branches at basal cell
154 contacts. AcS branches from neighbouring cells did not exhibit physical continuity nor
155 penetrate the plasma membrane (Figure 2B, insert). Instead, AcS branches snugly fit into
156 finger-like medial membrane folds of bicellular membranes (Figure 2G-H, Supplementary
157 Figure 2C), wherein E-cadherin-based adhesion sites and actin cross-linkers were localized
158 (Figure 2Hc-e,I-J, Supplementary Figure 2C-E). This arrangement of finger-like and adhesive
159 membranes at the extremities of AcS branches suggested a “zippering” effect at this level,
160 potentially providing structural and architectural stability to the AcS network that connects each
161 epithelial cell within the differentiated domain (Figure 2K).

162

163 **Actin star formation relies on significant cell contractility and minimal substrate** 164 **adhesion**

165 Similar self-organizing structures resembling AcSs have been shown to emerge *in vitro* within
166 minimal actin cortices on supported lipid layers, upon the addition of myosin-II filaments and

167 permissive contractility^{24,25}. Consequently, we speculated that cell contractility might be a
168 prerequisite in our system for the generation of AcSs. Analyses of myosin-IIA-KI-GFP organoid
169 monolayers revealed a concentrated GFP signal at the AcS node and its surrounding area
170 (Figure 3A-B). This finding was confirmed with endogenous phosphorylated myosin light chain
171 2 (P-MLC2) in 2D organoid monolayers (Figure 3C-D) and with endogenous myosin-IIA in
172 adult mouse intestine (Supplementary Figure 3A). Notably, a substantial proportion of total
173 cell contractility localised at the AcS level in the basal domain (Figure 3E), with approximately
174 61.5% of myosin-IIA-GFP and 61.3% of P-MLC2 signal intensity (Figure 3F). This suggests
175 that the bulk of cell contractility accumulates at basal AcS structures. Furthermore, the
176 contractile capacity of the differentiated cell type was particularly elevated compared to the
177 proliferative cells of the crypt-like domain (Figure 3G), with myosin-IIA-GFP and P-MLC2
178 signal intensities averaging 1.30 and 2.37 times higher, respectively (Figure 3H). Similarly, P-
179 MLC2 signal intensity was significantly lower in crypts compared to villi in adult small intestine
180 (Supplementary Figure 3B-C). These data highlighted a distinct tissue patterning of
181 contractility levels within this epithelium. Interestingly, live imaging analysis indicated that
182 AcSs formed from actin foci that rapidly coalesced in cells that transverse the periphery of the
183 crypt-like domain into the differentiated domain (Supplementary Figure 3D; Video S3). Thus,
184 the emergence of AcS coincided with the transition of cells into a highly contractile tissue
185 domain. Furthermore, we directly probed the necessity of contractility for AcS formation.
186 Treating organoid-derived monolayers with blebbistatin, an inhibitor of actomyosin activity,
187 resulted in the disappearance of typical AcS structures from the basal surface (Figure 3I).
188 Under this condition, the actin cytoskeleton mainly organized along the lateral membranes
189 and formed thin cables of stress fibers (Figure 3I). Similarly, inducible myosin-IIA-KO caused
190 a significant dismantling of AcSs (Supplementary Figure 3E). In addition, restoring contractility
191 in blebbistatin treated cells through subsequent wash-out led to the reformation of AcSs in
192 approximately 30 min (Figure 3 J-K; Video S4). Live recording of actin cytoskeleton dynamics
193 during this process revealed an active reorganization of actin cables (Video S5). Local inward
194 contraction within each cell triggered the massive coalescence of actin into central foci and
195 the accumulation of small actin bundles into thick radially arranged actin bundles, i.e. the
196 forming AcS node and branches, respectively (Figure 3J; Video S5). Collectively, these
197 findings pointed out the pivotal role of contractility in AcS generation and suggested that the
198 star-like organization of the actomyosin network may be mechanically sensitive.
199 We then manipulated the mechanical environment of the organoid-derived monolayer by
200 varying substrate rigidities using various polyacrylamide substrates (Matrigel-coated PAA
201 gels)²⁶. AcSs grew on soft substrates with a rigidity of 300 Pa (Figure 4A-B), a rigidity
202 comparable to the *in vivo* condition²¹. However, stiffer substrates caused basal actin network
203 remodelling, leading to the disappearance of AcSs (Figure 4A-B). Specifically, on 2.4 kPa

204 substrates, there was a shift towards the formation of numerous interconnected actin foci
205 instead of a single actin node, while on 5.2 kPa substrates, stress fibre-like actin bundles
206 predominated (Figure 4A-B). Thus, the mechanical properties of the cell substrate and
207 subsequent cell-substrate adhesion level seem to be important for AcS formation.

208 To directly validate this hypothesis *in vitro*, we turned to a well-established intestinal epithelial
209 cell line, adenocarcinoma Caco2 cells, in which the formation of AcS has not been previously
210 documented. Initially, we grew Caco2 cells on stiff adhesion permissive substrates such as
211 glass, and found canonical stress fibres instead of AcSs (Figure 4C, upper left panel). While
212 Caco2 cells on soft CL-Matrigel substrates ²¹ (~300 Pa, comparable with the PAA gels used
213 in Figure 4A) show significant loss of stress fibres (Figure 4C, upper right panel), AcS
214 organization was still absent. We then elevated actomyosin contractility through calyculin-A
215 treatment and discovered while no discernible modulation of the basal actin arrangement on
216 the glass substrates (Figure 4C, lower left panel), the enhanced contractility caused the
217 formation of AcS-like structures on soft CL-Matrigel substrates (Figure 4C, lower right panel).
218 Of note, we found Caco2 cells developed large FAs (paxillin staining) on stiff substrates which
219 were largely absent on soft crosslinked Matrigel substrates (Figure 4C). Along this line, we
220 then tested if weakening cell-substrate adhesion might facilitate the development of AcS
221 networks. We cultured these cells on micropatterned substrates featuring alternating adhesive
222 and non-adhesive regions (Figure 4D). While Caco2 cells displayed conventional stress fibres
223 on the adhesive areas, intriguingly, they developed patterns resembling AcSs on the non-
224 adhesive regions (Figure 4E). These results suggest that lack of conventional cell-substrate
225 adhesion facilitates the AcS network formation. Altogether, these results highlighted the
226 critical roles of both mechanical properties of epithelial cells and their environment in AcS
227 development, and suggested the existence of a critical force balance between the AcS lattice
228 and cell-substrate adhesion. We concluded that the development of star-like actin structures
229 likely arose from a combination of mechanical properties inherent to the intestinal epithelium:
230 low adhesion to the substrate and high capacity for contractility.

231

232 **The actin star network provides epithelial morphological and dynamical stability**

233 What are AcS' functions in the epithelial tissue? We found that inhibition of AcS formation with
234 blebbistatin treatment in the organoid derived monolayer induced a decrease in cell height
235 (Figure 5A-B), indicating a shift from a columnar to a cuboid cell shape in the absence of the
236 AcS network. Moreover, the treatment increased basal cell area (Figure 5C-D) and reduced
237 cellular hexagonality, as quantified through a decrease in local triangular order (see Methods;
238 Figure 5G). In addition, local inhibition of AcSs via light-inducible blebbistatin activation
239 resulted in similar cell area modifications (Figure 5E-F). Conversely, the gradual re-

240 establishment of AcSs following blebbistatin treatment wash-out coincided with basal cell
241 shape remodelling, characterized by the reduction of cell area and the acquisition of a more
242 circular and hexagonal form (Supplementary Figure 4A-C; Video S6). Consistently, we
243 observed an enhanced cell density within the epithelial tissue (Supplementary Figure 4D).
244 Hence, AcSs likely contributed to the maintenance of a tightly packed columnar epithelial
245 monolayer. Moreover, as shown in Figure 2B, 2G-J, AcSs contained in each epithelial cell
246 were mechanically connected to each other via finger-like E-cadherin-based junctions on the
247 basal surface, and we thus hypothesized that the AcS network may place the differentiated
248 tissue under a homogenous tension.

249 To test this, we next incorporated our experimental observations into a computational model
250 of the cellular assembly, called vertex model (see Supplementary Information). We first
251 considered a coarse-grained model, where AcS formation triggers a homogeneous contractile
252 response, through a reduction of the preferred cell area and cell perimeter (Figure 5G-H;
253 Supplementary Information, Section I, Figure S1), in proportion set by experiments. As in
254 experiments, we observed an increase in the level of hexagonality, as measured through the
255 triangular order, within the cells undergoing the contractile stresses as compared to other cells
256 (Figure 5I-K; Supplementary Information, Figure S6G; see Methods, section Computational
257 modelling). This effect was reversible upon the removal of the contractile stress, thus
258 mimicking the effect of blebbistatin. We also considered a second model where AcSs are
259 modelled by a discrete set of force dipoles between the cell-cell junction midpoint and the cell
260 barycentre (Supplementary Information, Section II, Figure S3). Such a second model leads to
261 a similar path in the preferred area and perimeter space (see Supplementary Information,
262 section II). These simulations also suggested that the resulting tissue was under high tension.
263 To experimentally assess the level of tissue tension, we next laser-dissected a single AcS and
264 then monitored the behaviour of surrounding AcSs (labelled as actin nodes N1-6) (Figure 6A-
265 B; Video S6). We found an almost immediate recoil of neighbouring AcS nodes after the
266 ablation and existence of a visible recoil at large distances (Figure 6A-C). This indicated that,
267 in the differentiated epithelial area, the AcSs of neighbouring cells were interconnected and
268 allowed the transmission of tension beyond several rows of cells. Based on our vertex model
269 simulation, in which a cell is ablated within a tensile tissue, we justified that the recoil speed is
270 informative of the cell-substrate friction (Figure 6D-E). In our simulations, the delay in the strain
271 propagation scaled with the distance to the ablated cell according to $\tau \sim L^2/K$, i.e. with K an
272 effective diffusion of elasticity that is inversely proportional to the friction to the substrate
273 (Figure 6F). These results showed a diffusion effect of the initial local elastic response after
274 laser dissection and the existence of a mechanical diffusion of elasticity away from the ablation
275 site, testifying of the large-scale connectivity provided by the AcS lattice.

276 Furthermore, we observed that the blebbistatin-treated organoid-derived monolayer displayed
277 numerous and large basal cell protrusions resembling lamellipodia in the villus-like domain
278 (pseudo-coloured in green, Figure 7A-B, $t = 0$ min). Upon recovery of contractility following
279 blebbistatin wash-out, AcSs re-growth occurred (as discussed earlier), which was
280 accompanied by the gradual disappearance of basal lamellipodia (Figure 7A-B $t = 2$ to 25 min;
281 Video S5). We thus propose that AcSs might play a role in inhibiting basal cell dynamics. To
282 directly test this hypothesis, we proceeded to laser dissection of a specific AcS and monitored
283 its impact on the basal cell surface (Figure 7D). At 125s after AcS removal, the actin network
284 reorganized and exhibited multiple actin foci within the cell which was targeted by laser
285 dissection, indicating that AcS did not yet reformed. During this period, the basal cell surface
286 expanded and exhibited actin-positive cell protrusions. Indeed, the perimeter of basal
287 protrusive extension in the laser-dissected cell increased from $2.6 \pm 2.6 \mu\text{m}$ in the pre-ablation
288 condition to $75.8 \pm 3.7 \mu\text{m}$ after the ablation (Figure 7C; Video S7). Based on these findings,
289 we concluded that the AcS lattice restricted epithelial basal protrusive activity by placing the
290 tissue under tension. These data prompted us to explore the participation of the AcS network
291 to global epithelial tissue behaviour. As compared to the control condition, a blebbistatin
292 treatment led to more persistent cell trajectories (Figure 7E), and more correlated velocities,
293 both temporally (D , see Methods, Figure 7F-I), and spatially (λ , see Methods, Figure 7J).
294 These observations were coherent within the generic theory of Henkes et al.²⁷, in which the
295 increase of the protrusion persistence time τ drives an increase in the persistence of cell
296 trajectories, as well as an increase in the velocity correlations D and λ . Collectively, these data
297 demonstrated the functional impact of the AcS network which provides to the epithelial tissue
298 a morphological stability, a mechanical connectivity and a long-range coordination.

299

300

301 DISCUSSION

302

303 Actomyosin star-shaped assemblies develop in differentiated intestinal epithelial cells

304 In this study, we unveil a supracellular star-shaped organization of actin network in mammalian
305 intestinal epithelial cells and demonstrated its implication in various cellular and tissue
306 functions (Figure 7K). To our knowledge, such actin meshwork development has not been
307 previously documented in mammals, and contrast to the conventional basal actin organization,
308 which predominantly exhibit stress fibres and/or lamellipodia^{28,29,30}. However, some studies
309 have reported unusual basal actin organization in specific contexts. In rat embryonic cells,
310 geodesic-like arrangements of multiple actin foci transiently form before the formation of stress
311 fibres, under the control of actin cross-linking factors (i.e. alpha-actinin, tropomyosin)³¹.

312 Similar polygonal actin meshes, named cross-linked actin network (CLANs), organize in
313 individual human trabecular meshwork cells^{32,33}. In the same line, super-resolution imaging
314 has shown a multitude of actin foci cortex organization within individual mouse embryonic
315 stem cells³⁴. Importantly, these structures did not denote a multicellular organization and were
316 not regulated by myosin-II-mediated contractility; instead, they relied on actin polymerization.
317 In addition, when mouse embryonic fibroblasts were cultured on non-adhesive/adhesive
318 micropatterns, dynamic actin foci network developed on non-adhesive areas and were
319 exacerbated under inhibition of actin polymerization³⁵. Bershadsky and colleagues then
320 showed through modelling that in this model system, myosin II-mediated contractility propels
321 small actin assemblies towards each other, converging into a single large actin node³⁵.
322 Authors then hypothesized that multiple actin foci network may provide cytoskeletal
323 connectivity to distal parts of the cell³⁵. Furthermore, star-like actin networks have been
324 previously reported *in silico* cell-free systems^{24,36,37}, where authors demonstrated that
325 incorporation of myosin-II-based contractility on an F-actin monolayer induces the formation
326 of a star-shaped actomyosin network and places the actin array under a 'dynamical steady
327 state'^{24,36,37}. Altogether, these studies underline how plastic the basal actin network can be in
328 response to environmental factors³⁸. They also pinpoint two pivotal factors: contractility and
329 competition with cell-substrate adhesion, which may explain why AcS organization has not
330 been observed yet in mammals *ex vivo*. One possibility is that the conventional substrates
331 employed in routine cell culture experiments are glass or plastic, which are exceedingly rigid
332 and foster robust focal adhesions^{39,40,41}, impeding the formation of AcSs. In our experiments,
333 we cultivated organoid-derived monolayers under conditions that closely emulate the *in vivo*
334 rigidity, significantly softer than a typical cell culture dish²¹. However, using soft substrates
335 alone was not enough to facilitate the formation of AcSs in the cancerous Caco2 cell line
336 (Figure 4C). Another critical factor is the degree of contractility activation. Indeed, elevating
337 contractility on a soft substrate provoked the appearance of AcSs in Caco2 cells. Similarly,
338 intestinal differentiated compartments with heightened contractility, developed the AcS
339 network, while low-contraction crypt compartments lacked AcSs (Figure 3G-H, Supplementary
340 Figure 3B-C). Moreover, the AcS network was exclusively formed when organoid-derived
341 monolayers were grown on soft substrates that hinder geodesic-like arrangements of multiple
342 actin foci or mature focal adhesion formation (Figure 4A-B). Additionally, Caco2 monolayers
343 displayed AcS formation under weakly adherent culture conditions solely when elevated
344 contractility activation is induced via calyculin-A treatment (Figure 4E). It is tempting to suggest
345 that these transformed/cancerous cells might have lost their innate capacity to promote
346 optimal contractility, at least on the basal side when grown on soft substrate and in a weakly

347 adherent state. Subsequent experiments will be imperative for definitely clarifying this
348 hypothesis.

349

350 **The basal actin star assembly generates a supracellular connecting network**

351 The AcS network may represent a distinctive multicellular mechanical entity within the basal
352 region of differentiated epithelial cells. AcS self-organized structures were reminiscent of the
353 apico-medial actomyosin, well-described in the *Drosophila* epithelium and which is required
354 for cell shape remodeling through apical constriction^{14,15,16,17,18}. Here, while the apical actin
355 network remained localized to the subcortical zone behind adherent and tight junctions¹¹, the
356 basal contractile AcS network extended in a more centripetal manner in intestinal epithelial
357 cells at equilibrium, yet remained interconnected with E-cadherin-based junctions (Figure 2).
358 When tension increases on the apical side, an apical-medial actomyosin network orchestrates
359 tissue folding^{14,15,16,17,18}. During intestinal development, apical constriction also occurs in
360 mammalian intestine for crypt invagination^{42,43,44}. It might be tempting to draw parallels with
361 basal AcSs in differentiated intestinal epithelial cells, which naturally colonize curved geometry
362 of villi in adults (Figure 1A), but AcSs also developed on flat surfaces in *in vitro* cultures (Figure
363 1D). This implies that they must serve functions beyond differentiated tissue folding.

364 In contrast to other epithelia, we and others showed that the majority of cell contractility is
365 localized on the basal side of differentiated intestinal cells⁴⁴ (Figure 3E-F; Supplementary
366 Figure 3B-C). Among the main differentiated gut cell types, the epithelial apical side gets
367 specialized for nutrient absorption with the creation of a brush border of microvilli in
368 enterocytes or for mucus secretion in goblet cells^{45,46}. Although brush border anchors in the
369 terminal web composed of actomyosin and intermediate filaments, this is a robust apical
370 assembly that undergoes little remodelling in physiological conditions once formed, and for
371 which a role for its contractile property outside of the context of brush border formation remains
372 elusive^{47,46,48}.

373 Star-shaped actomyosin assemblies on the basal cell surface have only rarely been described
374 in epithelia. An ultrastructural study conducted by M. De Ceccatty in 1986 focusing on
375 morphological investigations of sponge epithelial cytoskeletons, reported a similar star-shaped
376 cytoskeletal organization on the basal epithelial layer⁴⁹. Interestingly, our study echoes a
377 recent study conducted by Harvey and colleagues⁵⁰. These authors have also shown the
378 presence of a basal-medial actomyosin network in *Drosophila* epithelium, which appears to
379 be related to our AcS network. However, this study lacks a detailed characterization of basal
380 actomyosin structures and their multicellular connectivity property, as the primary focus was
381 on investigating a newly identified basal cell-cell adhesion complex named 'basal spot
382 junctions'⁵⁰. In the differentiated intestinal epithelium, AcS branches connected E-cadherin-
383 based basal contacts that localized at structures between engulfed fingers and intercellular

384 bridges with basolateral cell-cell contacts, such as discussed by Svitkina and colleagues ⁵¹,
385 testifying that AcS and basal contacts were under substantial tension. In addition, the
386 presence of mechanosensitive elements like E-cadherin, β -catenin, α -catenin, vinculin, and
387 α -actinin further hints towards the mechano-responsive nature of this network. The actin star
388 network may thus represent a new way to create a more elastic communication system to
389 transmit force imbalance through the tissue.

390

391 **The actin star network constitutes a new mechanical apparatus for epithelial tissue** 392 **organization and coordination**

393 The AcS network represents a mechanical subunit at the basal cell side that connects
394 surrounding epithelial cells. As such, it exerted functions at cellular and multicellular levels.
395 At the cellular level, the AcS cytoskeletal lattice conferred morphological and functional
396 stability to cells. It modulated cell shape by constraining the basal cell surface, thereby
397 enhancing the columnar appearance and refining cell shape (Figure 5A-F; Supplementary
398 Figure 4A-D). Additionally, it maximized epithelial cell packing and order (Figure 5G-K), which
399 represents an important factor for stabilizing the epithelial assembly and optimizing the
400 intestinal surface for nutrient absorption. Moreover, the disappearance of basal cell protrusive
401 activity upon the formation of the AcS network suggested that AcSs restricted lamellipodia
402 formation. Thus, the AcS network may facilitate cell transition from a motile, fluid-like, to a
403 static, solid-like, morphology, as observed in mature epithelia ²⁰. To characterize this
404 transition, we first considered the hexatic order which is a well-known measure in condensed
405 matter ⁵². Nevertheless, here we found that the triangular order, rather than the hexatic one,
406 was the best probe of the AcS formation in experiments, and increased in active stresses in
407 simulations (see Supplementary Information).

408 Beyond its cellular functions, the AcS network adopted a central role in orchestrating tissue
409 architecture and homeostasis. By enhancing spatial coupling of differentiated epithelial cell
410 clusters, it ensured the mechanical continuity of the epithelial monolayer, thereby upholding
411 tissue integrity. Furthermore, the cytoskeletal network regulated cell shape, promoting a
412 uniform cell hexagonalization that modulates established an epithelial order akin to a close-
413 to-solid phase ²⁰. By constraining lamellipodia, AcSs hampered cell dynamics, pivotal for the
414 formation of a tissue at equilibrium. This restriction mitigated random cell movement within the
415 monolayer, leading to a relatively homeostatic and uniformly structured tissue architecture. In
416 addition, at a broader tissue scale, the AcS network interconnected differentiated cells within
417 the villus-like domain, and may facilitate the controlled collective cell movement observed
418 along the crypt-villus axis ⁵³. An earlier study on gut epithelia turnover reported it to be
419 mediated by actin-rich basal protrusions driven collective cell migration ⁵⁴. There, it was also

420 suggested that front-back polarity in the migrating cell is mediated by basal protrusions. Here,
421 while observing the endogenous basal actin along the villi, we were unable to detect
422 lamellipodial structures in the enterocytes. The majority of enterocytes were uniformly
423 hexagonal and lacked front-back polarity. There was merely an evolution of the enterocyte
424 basal cell shape at the very tip of the villus, which could resemble lamellipodial activity at that
425 point (not shown) and might represent some active migrating cells.

426 In summary, we describe here a unique tissue-spanning multicellular organization of star-
427 shaped actin networks in differentiated basal mammalian epithelium. Along the line of the De
428 Ceccatty' hypothesis of "histoskeleton" in sponge ⁴⁹, we believe that the AcSs represent a
429 cytoskeletal network for coordination of mammalian epithelial tissue organization and its
430 functioning. Our *in vivo* observations, as well as *ex vivo* and *in vitro* experiments, further
431 confirmed the presence of this network in the intestinal epithelium, its mechanism of formation,
432 and its essential role in tissue organization. We demonstrated that this network emerged under
433 a high contractility / low cell-substrate adhesion state that naturally existed in the differentiated
434 intestinal epithelium. We further showed its importance in regulating various functions from
435 cell to tissue levels, that ensured tissue homeostasis and maintain healthy epithelial
436 architecture. Together, this hints towards a mechanism of AcS network-mediated complex
437 self-organization of the differentiated tissue.

438

439 **Limitations of the study**

440 While we showed the formation of actin stars in intestinal tissue, it is yet to be seen whether
441 related structured networks also exist in other mammalian tissues. Notably, similar networks
442 have been reported in sponge basal epithelium ⁴⁹ and very recently in *Drosophila* epithelium
443 ⁵⁰. Moreover, the only way to challenge AcSs at the moment is to modulate contractility.
444 Although contractility is highly enriched at AcSs in differentiated intestinal cells, further
445 characterization of these actomyosin structures will require the identification of core molecular
446 components of AcS node and cables to specifically target them.

447 This study also raises the questions of how the dynamics of actin cables are coupled to the
448 cell-cell junction rearrangement. While we show the network to be mechanoresponsive, further
449 investigation would enlighten us about to what extent the network may regulate tissue
450 mechanotransduction through basal junctions compared to apical mechanical apparatus.
451 Furthermore, in-depth characterization of the contractile property of the AcS with optimal
452 spatio-temporal resolution will be required to define whether these self-organized actomyosin
453 assemblies are pulsatile or persistent, as described for the apico-medial actomyosin network
454 in *Drosophila* ¹⁴.

455

456 **Acknowledgments**

457 We thank Ana-Maria Lennon-Dumenil, Robert S. Adelstein and Danijela Vignjevic for
458 providing mice. We thank Arnaud Echard (Institut Pasteur, Paris), Guillaume Salbreux
459 (UNIGE, Geneva), Benoit Ladoux, René-Marc Mège, Guillaume Romet-Lemonne and Antoine
460 Jegou (IJM, Paris) for helpful discussions. Confocal microscopy and spinning-disc analyses
461 were performed in the ImagoSeine microscopy facility (IJM) and PICS� imaging facility
462 (IBDM). This work was supported by grants from the Groupama Foundation – Research Prize
463 for Rare Diseases 2017 (to D.D), France 2030, the French Government program managed by
464 the French National Research Agency (ANR-16-CONV-0001) and from the Excellence
465 Initiative of Aix-Marseille University - A*MIDEX (to J.F.R.), as well as by ANR-20-CE30-0023
466 (COVFEFE) (to J.F.R.), the Fondation ARC (to M.S., J.S. and D.D), the Fondation pour la
467 Recherche Médicale FRM (to A.B.), the Marie Skłodowska-Curie Actions, Postdoctoral
468 Fellowships, project 101108750 (to A.B.), the Marie Skłodowska-Curie Actions Postdoctoral
469 Fellowship, project 846449 (to W.X.), the Université de Paris IdEx UP 2021-I-050 funded by
470 the French Government through its “Investments for the Future” (to D.D.), the ANR-19-CE13-
471 0014-01 (to D.D.), the ANR-20-CE13-0015 (to D.D.), the Human Frontier Science Program
472 (RGP0038/2018) (to D.D.), and the INCA PLBIO20-150 – Cancéropole Ile-de-France (to D.D.)
473 and the CNRS through the MiTi interdisciplinary programs (to D.D.).

474

475 **Supplemental Information:** Supplementary Figures S1-S4, Videos S1-S7, and
476 Supplementary Information file detailing the vertex model simulation procedure are in the
477 online version of the paper.

478

479 **Author contributions:** A.B., M.S., W.X., S.Z.L., M.K., E.B., S.R., D.B., M.T., J.F.R. and D.D.
480 designed and performed experiments and required analyses. A.B., M.S., S.Z.L., M.K., D.B.,
481 F.R., M.T., J.F.R. and D.D. coordinated the overall research and experiments, and wrote the
482 manuscript.

483

484 **Conflict of interest:** The authors declare no conflict of interest.

485

486

487 **FIGURE LEGENDS**

488

489 **Figure 1: Differentiated intestinal epithelial cells display star-shaped actin**
490 **cytoskeleton. (A)** Scheme showing the functional organization of the mouse small intestinal
491 tissue where the proliferative crypt domains are shown in blue and the differentiated villus
492 compartment in yellow. **(Ba-d)** Confocal analysis of actin distribution in the villus domain.
493 Nuclei are stained in blue in (d). Green arrowheads point to actin stars (AcSs). Scale bars, (a)
494 50 μm , (b-d) 10 μm . **(C)** Scheme showing the self-organization of intestinal organoid-derived
495 monolayer with the proliferative crypt-like domains in blue and the differentiated villus-like
496 compartment in yellow. **(Da-d)** Confocal analysis of actin distribution in the apical or basal side
497 of an organoid-derived monolayer. xz view is presented in (d). Crypt-like domains are delimited
498 in blue. Green arrowheads point to actin stars. C, crypt-like domain. Scale bars, (a-b) 100 μm ,
499 (c) 10 μm , (d) 50 μm .

500

501 **Figure 2: Basal actin star assembly creates a multicellular connecting network. (A)**
502 Airyscan confocal microscopy and depth-coded z-projection of actin, membranes and DNA
503 localization in the basal side of organoid-derived monolayers. Scale bar, 10 μm . **(B)** N-SIM
504 microscopy analysis of basal actin distribution in organoid-derived monolayers. Scale bar, 15
505 μm , insert 2 μm . **(C)** Statistical analysis of the distance between the AcS node and the cell
506 center of mass in organoid-derived monolayers. Mean distance = 1.48 ± 0.14 μm
507 (mean \pm S.E.M). N = 3 experiments, n = 113 cells. **(D)** Statistical analysis of the number of actin
508 branches per AcS. Mean number of actin branches per star = 6.04 ± 0.07 (mean \pm S.E.M). N =
509 3 experiments, n = 90 cells. **(E)** Statistical analysis of the actin cable length in AcSs. Mean
510 length = 5.16 ± 0.06 (mean \pm S.E.M). N = 4 experiments, n = 331 cells. **(F)** Statistical analysis of
511 the angle formed between actin cables (α) or between actin cables and plasma membranes
512 (β). Mean $\alpha = 59 \pm 1.24^\circ$ (mean \pm S.E.M), mean (β) = $89.3 \pm 1.78^\circ$. N = 4 experiments, n (α) = 162
513 cells, n (β) = 55. **(G)** Airyscan confocal analysis of actin (green), membranes (magenta) and
514 DNA (blue) in organoid-derived monolayers. Scale bar upper row 5 μm , low row 2 μm . **(Ha-e)**
515 Transmission electron microscopy analysis of the basal domain of differentiated cells in
516 organoid-derived monolayers. Actin cables are pseudo-colored in green, adherens junction-
517 like adhesions in light blue. ECM, extracellular matrix. Non-pseudo-colored images are shown
518 in Supplementary Figure 2 C. Scale bars, (a) 5 μm , (b-c) 2 μm , (d-e) 0.5 μm . **(I-J)** Confocal
519 analysis of E-cadherin and α -actinin-1 at the basal side of organoid-derived monolayers. Scale
520 bar, 5 μm . **(K)** Scheme describing the architecture of AcS network (green) and cell membranes
521 (magenta) in the basal side of organoid-derived monolayers. E-cadherin-based complexes
522 observed in (H-I) are depicted in blue.

523

524 **Figure 3: Cell contractility triggers actin star formation. (A)** Confocal analysis of myosin-
525 IIA-KI-GFP (magenta) localization in AcSs (green). Scale bar, 5 μ m. **(B)** Statistical analyses
526 of the signal intensity level of myosin-IIA-GFP in nodes and cables of AcSs. Normalized
527 myosin-IIA-GFP signal intensity in AcS nodes = 0.666 ± 0.01 (mean \pm S.E.M), in AcS cables =
528 0.034 ± 0.001 . N = 3 experiments, n = 154 cells. Mann-Whitney test, ****p<0.0001. **(C)** N-SIM
529 analysis of P-MLC2 (magenta) localization in AcSs (green). Scale bar, 5 μ m. **(D)** Statistical
530 analyses of the signal intensity level of P-MLC2 in nodes and cables of AcSs. P-MLC2 signal
531 intensity in AcS nodes = 0.743 ± 0.038 (mean \pm S.E.M), in cables = 0.417 ± 0.026 . N = 3
532 experiments, n = 98 cells. Unpaired t-test, ****p<0.0001. **(E)** Confocal analysis of the apico-
533 basal distribution of myosin-IIA-GFP (green) or P-MLC2 (magenta) in organoid-derived
534 monolayers. Scale bar, 10 μ m. **(F)** Statistical analyses of the signal intensity level of myosin-
535 IIA-GFP and P-MLC2 in the apical and basal domain of differentiated cells. Mean apical
536 myosin-IIA-GFP signal intensity in differentiated compartments = 725 ± 48 (mean \pm S.E.M),
537 basal myosin-IIA-GFP = 1159 ± 72 , apical P-MLC2 = 1314 ± 63 , basal P-MLC2 = 2078 ± 135 . N
538 = 3 experiments, n (cells in differentiated compartments) = 23 cells. Two-way ANOVA,
539 ****p<0.0001. **(G)** Confocal analysis of myosin-IIA-GFP (green) and P-MLC2 (magenta)
540 distribution in an organoid-derived monolayer. Nuclei (DNA) are stained with Hoechst33342
541 (blue). Crypt-like domains (c) are delimited with a dotted blue line. Scale bar, 20 μ m. **(H)**
542 Statistical analyses of the relative signal intensity level of myosin-IIA-GFP and P-MLC2 in
543 differentiated and crypt-like compartments. Mean myosin-IIA-GFP signal intensity in
544 differentiated compartments = 2049 ± 128 (mean \pm S.E.M), in crypt-like compartments =
545 1572 ± 163 , mean P-MLC2 signal intensity in differentiated compartments = 3644 ± 224 , in crypt-
546 like compartments = 1536 ± 176 . N = 3 experiments, n (cells in differentiated compartments) =
547 23 cells, n (cells in crypt-like compartments) = 19 cells. Two-way ANOVA, *p = 0.012,
548 ****p<0.0001. **(I)** Confocal analysis and z-projection of actin distribution in the basal domain
549 of control or blebbistatin-treated organoid-derived monolayers. Scale bar, left panel 20 μ m,
550 right panel 10 μ m. **(J)** Time-lapse images of CellMask actin (green) in tdTomato (magenta)
551 organoid-derived monolayer after 1h blebbistatin treatment and then wash-out (t = 0min).
552 Crypt-like domains (c) are delimited with a dotted blue line. Scale bar, 10 μ m. **(K)** Statistical
553 analysis of the mean time of AcS re-formation after blebbistatin treatment and wash-out. Mean
554 time (min) = 51.41 ± 1.67 (mean \pm S.E.M). n = 101 cells.

555

556 **Figure 4: Epithelial mechanical properties and its environment condition on actin stars**
557 **development. (A)** Confocal analysis of the basal actin arrangement in organoid-derived
558 monolayer grown on 300Pa, 2.4 or 5.2kPa PAA gels. Scale bar, 10 μ m. **(B)** Statistical

559 analyses of basal actin-based structures formed on different rigidity PAA gels. Mean AcS
560 proportion at 300Pa = $33 \pm 10\%$, (mean \pm S.E.M), at 2.4kPa = $5.14 \pm 3.38\%$, at 5.2kPa = 0%.
561 Mean actin aster lattice proportion at 300Pa = $2 \pm 1.16\%$, at 2.4kPa = $14.14 \pm 3.95\%$, at 5.2kPa
562 = $12 \pm 3.34\%$. Mean actin stress fiber proportion at 300Pa = $0.67 \pm 0.67\%$, at 2.4kPa =
563 $3.57 \pm 2.38\%$, at 5.2kPa = $16.62 \pm 6.36\%$. N = 3 experiments, n (300Pa) = 107 cells, n (2.4kPa)
564 = 160 cells, n (5.2kPa) = 229 cells. Two-way ANOVA, $**p < 0.01$. **(C)** Confocal analysis of basal
565 actin (green), paxillin (red) and E-cadherin (magenta) in Caco2 cells grown on glass
566 coverslips, uncoated or on cross-linked Matrigel, and treated with either DMSO (control) or
567 20nM calyculin-A. Cells stained with phalloidin and paxillin show actin (green) or focal-
568 adhesion (red) organization respectively. Nuclei (blue) are stained with Hoechst33342. Scale
569 bar, 5 μ m. Blue arrows show AcS nodes in Caco2 cells. Scale bar, 2 μ m. **(D)** Scheme showing
570 the micropatterned substrates used for Caco2 monolayer culture in adhesive / non-adhesive
571 conditions. **(E)** Confocal analysis basal distribution of actin (green) and E-cadherin (magenta)
572 in Caco2 cells grown on adhesive / non-adhesive micro-patterns. Red dotted lines delimit the
573 adhesive from the non-adhesive areas. Blue arrows in the inset indicate AcS nodes. Nuclei
574 (blue) are stained with Hoechst33342. Scale bars, upper row 10 μ m, lower row 5 μ m.

575

576 **Figure 5: The actin star network ensures epithelial morphological stability.** **(A)** Confocal
577 analysis and xz view of actin distribution in DMSO-treated or blebbistatin-treated organoid-
578 derived monolayers. Nuclei (gray) are shown. Green arrowheads point to AcSs. Scale bar, 10
579 μ m. **(B)** Statistical analysis of mean cell height in control or blebbistatin-treated cells. Mean
580 cell height in control = $10.79 \pm 0.33 \mu\text{m}^2$ (mean \pm S.E.M), in blebbistatin-treated = 8.03 ± 0.26 . N
581 = 3 experiments, n (control) = 60 cells, n (blebbistatin-treated) = 65 cells. Unpaired t-test,
582 $****p < 0.0001$. **(C)** Statistical analysis of mean basal cell area in control or blebbistatin-treated
583 cells. Mean basal cell area in control = $69.56 \pm 1.25 \mu\text{m}^2$ (mean \pm S.E.M), in blebbistatin-treated
584 = 83.69 ± 1.96 . N = 3 experiments, n (control) = 675 cells, n (blebbistatin-treated) = 585 cells.
585 Unpaired t test, $****p < 0.0001$. **(D)** Confocal analysis of actin distribution in DMSO-treated or
586 blebbistatin-treated organoid-derived monolayers. Nuclei (gray) are shown. Scale bar, 20 μ m.
587 **(E)** Time-lapse of membranes-tdTomato before (green) and after (red) photo-activation of
588 azidoblebbistatin. Scale bar, 5 μ m. **(F)** Statistical analysis of the basal cell area modification
589 after photo-activation of azidoblebbistatin. Mean basal cell area fold change in pre-activation
590 condition = 1.015 ± 0.03 (mean \pm S.E.M), in post-activation condition = 2.353 ± 0.21 . N = 3
591 experiments, n (pre-activation) = 23 cells, n (post-activation) = 10 cells. Unpaired t-test,
592 $****p < 0.0001$. **(G)** Mechanical description of the AcS network contractility within a cell by active
593 stresses. Here, $T_i = \zeta s_i$ (with $\zeta > 0$) is the active tension mimicking the active contractility of actin
594 bundles. This can be further simplified to be active tensions T along the cell contour and active

595 cellular bulk stresses σ_a . **(H)** Theoretical analysis of cell anisotropy dictated by the active
596 pulling stress α and the active tension χ . The black solid line represents the theoretically
597 predicted critical rigidity transition line; see Eq. (S19) in Supplementary Information. The
598 symbols and arrow denote a possible path of cell differentiation. **(I)** Variation of the local
599 triangular order parameter map upon AcS formation and subsequent optimal cell
600 differentiation, or AcS inhibition under blebbistatin treatment and deficient cell differentiation.
601 **(J)** Statistical quantification of the local triangular and hexatic order *in silico*. **(K)** Statistical
602 quantification of the local triangular and hexatic order from experiments.

603

604 **Figure 6: The actin star network provides mechanical connectivity and long-range**
605 **coordination. (A)** Color-coded time-lapse analysis of AcS displacement after laser ablation
606 of a given AcS (white circle). The first image ($t = -10s$) is false-colored green, the image at a
607 given time, i.e. before ($t = 0s$) or after ($t = 1, 25$ or $60s$) laser ablation is false-colored in red.
608 Masks of AcS nodes are also presented in the lower panel. Scale bar, $10 \mu m$. **(B)** Scheme
609 showing the site of laser ablation with dotted circle in the AcS lattice (green) within the
610 epithelial monolayer (magenta), and depicting the AcS nodes (N) annotation for quantification.
611 **(C)** Average radial displacement of AcS nodes that neighbour the laser ablation point. N0,
612 point of AcS laser-ablation. **(D)** Upper panel, sketch of the active vertex model with cell-cell
613 junction viscosity. Lower panel, laser ablation protocol: the cell at the model ablation site has
614 its activity set to zero. **(E)** Average radial displacement of cell barycentres at the N -th row as
615 a function of time t after ablation (see Methods). **(F)** Time to reach $0.20 \mu m$ radial
616 displacement, $t_{0.2\mu m}$, (mean \pm S.E.M) as a function of the row of cells (i.e., distance to the laser
617 ablation site), in experiments (blue, $n = 13 - 18$ tracked AcS nodes) and simulations (red,
618 averaged over $n = 5$ independent simulations).

619

620 **Figure 7: The actin star assembly restricts epithelial dynamics. (A)** Time-lapse of
621 CellMaskActin (white) and membranes-tdTomato (red) organoid-derived monolayer after 1h
622 blebbistatin treatment and then wash-out ($t = 0$ min). Actin-based protrusive structures are
623 outlined in green, and also shown in the lower black and white panel. Yellow arrowheads point
624 to actin-based protrusive extension. Scale bars, $10 \mu m$. **(B)** Statistical analysis of cell perimeter
625 protrusive before and after blebbistatin wash-out. Mean perimeter protrusive before =
626 42.37 ± 1.92 (mean \pm S.E.M), after = 3.64 ± 0.78 . $N = 4$ experiments, $n = 100$ cells. Paired t-test,
627 **** $p < 0.0001$. **(C)** Statistical analysis of the perimeter of basal protrusive cell extension after
628 laser ablation of the AcS node. Mean perimeter in pre-ablation condition = 2.612 ± 2.61
629 (mean \pm S.E.M), in post-ablation condition = 75.83 ± 3.69 . $N = 3$ experiments, $n = 8$ cells.
630 Unpaired t-test, **** $p < 0.0001$. **(D)** Time-lapse of CellMaskActin (green) and membranes-

631 tdTomato (red) before or after laser ablation (blue dotted circle) of an AcS node. Cell perimeter
632 is outlined before ablation in yellow dotted line and after ablation in red dotted line. Yellow
633 arrowheads point to actin-based protrusive extension. Nuclei are stained in blue. Scale bar,
634 5 μ m. **(E)** Automated cell tracking in DMSO- or blebbistatin-treated tdTomato organoid-derived
635 monolayers, and t-projection of 20 frames time-lapse series. Monolayer background
636 corresponds to t = 0. Scale bar, 20 μ m. **(F)** Statistical analysis of the mean cell strain in DMSO-
637 treated or blebbistatin-treated organoid-derived monolayers. Mean cell strain in DMSO-treated
638 cells = 0.159 ± 0.0003 (mean \pm S.E.M), in blebbistatin-treated = 0.187 ± 0.0007 . n (DMSO-treated
639 cells) = 95863, n (blebbistatin-treated cells) = 21950. Mann-Whitney test, ****p<0.0001. **(G)**
640 Statistical analysis of the mean cell velocity in DMSO-treated or blebbistatin-treated organoid-
641 derived monolayers. Mean velocity in DMSO-treated cells = 0.123 ± 0.002 μ m/min
642 (mean \pm S.E.M), in blebbistatin-treated = 0.183 ± 0.004 . n (DMSO-treated cells) = 3116, n
643 (blebbistatin-treated cells) = 1622. Mann-Whitney test, ****p<0.0001. **(H)** Statistical analysis
644 of the mean diffusion coefficient in DMSO-treated or blebbistatin-treated organoid-derived
645 monolayers. Mean diffusion coefficient in DMSO-treated cells = 0.015 ± 0.003 (mean \pm S.E.M),
646 in blebbistatin-treated = 0.044 ± 0.009 . n (DMSO-treated cells) = 4, n (blebbistatin-treated cells)
647 = 3. Unpaired t-test, *p=0.0159. **(I-J)** Analysis of velocity correlations in DMSO-treated or
648 blebbistatin-treated organoid-derived monolayers: **(I)** autocorrelations, as a function of time,
649 **(J)** same-time correlations, as a function of the point-to-point distance (see Methods). N = 4
650 in DMSO-treated and N = 3 in blebbistatin-treated experiments. **(K)** Scheme depicting the
651 proposed model of AcS development in the mammalian intestinal epithelium.
652

653 **SUPPLEMENTARY FIGURE LEGENDS**

654

655 **Supplementary Figure 1: (A-C)** Confocal analysis of actin distribution in the mouse crypt
656 compartment. Crypt side view (B) and bottom view (C) are shown. Crypt domains are delimited
657 with blue line. L, crypt lumen. Scale bar A 100 μm , B-C 10 μm . **(D-E)** Confocal analysis of EdU
658 (D) and cytokeratin-20 (E) distribution in organoid-derived monolayers. Nuclei are shown in
659 gray. Crypt-like domains are delimited in blue. C, crypt-like domain. Scale bar (D), 20 μm , (E)
660 30 μm . Scale bar, 100 μm . **(F)** Confocal analysis of actin (green), ezrin (magenta) and DNA
661 (gray) in the apical or basal side of organoid-derived monolayers. Crypt-like domains are
662 delimited in blue. C, crypt-like domain. Scale bar, 20 μm .

663

664 **Supplementary Figure 2: (A-B)** Airy scan confocal analysis of paxillin (magenta) and actin
665 (green) in the area of crypt- / villus-like boundary or in the differentiated compartment. Crypt-
666 like domains are delimited in blue. C, crypt-like domain. Scale bar, 10 μm . **(Ca-e)** Transmission
667 electron microscopy analysis of the basal domain of differentiated cells in organoid-derived
668 monolayers. ECM, extracellular matrix. Scale bars, (a) 5 μm , (b-c) 2 μm , (d-e) 0.5 μm . **(D-E)**
669 Confocal analysis of β -catenin (magenta) or α -catenin (magenta) and actin (green) in the
670 differentiated compartment of organoid-derived monolayers. Scale bar, 5 μm .

671

672 **Supplementary Figure 3: (A)** Confocal analysis of actin (green) and myosin-IIA (magenta) in
673 the basal domain of differentiated cells along the villus of the mouse small intestine. Scale bar,
674 5 μm . **(B)** Confocal analysis of P-MLC2 distribution in the human intestinal tissue. Areas boxed
675 in yellow are presented on the right. Scale bar, 200 μm . **(C)** Statistical analyses of the signal
676 intensity of P-MLC2 in the villus epithelium and the crypt epithelium in the human small
677 intestine. Mean normalized signal intensity in the villus epithelium = 1, in the crypt epithelium
678 = 0.5691 ± 0.021 . N (intestinal biopsies) = 3. Unpaired t-test, **** $p < 0.0001$. **(D)** Time-lapse
679 analysis of AcS formation at exit of the crypt-like domain in organoid-derived monolayers.
680 Actin (green) and membranes (red) are shown. Yellow arrowheads point toward one AcS
681 formation. Crypt-like domains are delimited in blue. C, crypt. Scale bar, 10 μm . **(E)** Confocal
682 analysis of actin distribution in mosaic myosin-IIA-KO organoid-derived monolayers. Myosin-
683 IIA-KO-induced cells are positive for membranes-mG (green). Crypt-like domains are
684 delimited in blue. C, crypt. Areas boxed in yellow are presented on the right. Scale bar, 20 μm .

685

686 **Supplementary Figure 4: (A)** Time-lapse of CellMaskActin and membranes-tdTomato
687 organoid-derived monolayer after 1h blebbistatin treatment and then wash-out (t = 0min).
688 Color-coded t-projection of time-lapse series of membranes-tdTomato signal at the basal
689 domain during contractility recovery in organoid-derived monolayer is shown (t=0min in green,

690 t = 46 min in red). Scale bar, 10 μm . **(B)** Statistical analysis of basal cell area before and after
691 blebbistatin wash-out. Mean basal area before = 141.75 ± 5.67 (mean \pm S.E.M), after =
692 95.67 ± 3.69 . N = 4 experiments, n = 100 cells. Paired t-test, ****p < 0.0001. **(C)** Statistical
693 analysis of basal cell circularity before and after blebbistatin wash-out. Mean basal circularity
694 before = 0.70 ± 0.01 (mean \pm S.E.M), after = 0.79 ± 0.01 . n = 100 cells. Paired t-test,
695 ****p < 0.0001. **(D)** Statistical analysis of cell density before and after blebbistatin wash-out.
696 Mean cell density before = 7.65 ± 0.79 (mean \pm S.E.M), after = 9.40 ± 0.93 . Paired t-test,
697 **p = 0.004.

698

699

700

701

702 SUPPLEMENTARY VIDEOS

703

704 **Video S1:** Z-stack confocal imaging of actin distribution through the differentiated epithelial
705 monolayer of the villus compartment in the adult mouse small intestine. Left panel, distance
706 between z-slices, 0.42 μm . Scale Bar, 20 μm . Right panel, distance between z-slices, 0.23
707 μm . Scale bar, 5 μm .

708

709 **Video S2:** Z-stack confocal imaging of actin distribution through the proliferative epithelial
710 monolayer of the crypt compartment in the adult mouse small intestine. Distance between z-
711 slices, 0.23 μm . Scale bar, 10 μm .

712

713 **Video S3:** Time-lapse imaging of CellMask-Actin-GFP (green) and Membranes-tdTomato
714 (magenta) during cell exit from the crypt-like domain and cell entry in the differentiated domain
715 of organoid derived-monolayers. White arrowheads point toward one AcS formation. Crypt-
716 like domains are delimited in yellow circle. Right side shows magnified region of interest. Scale
717 bars, 10 μm (left) and 5 μm (right). Images were acquired every 3 min. Frame rate is 4 fps.

718

719 **Video S4:** Time-lapse imaging of CellMask-Actin-GFP (green) and Membranes-tdTomato
720 (magenta) in organoid derived-monolayers after blebbistatin treatment and subsequent wash-
721 out. Scale bar, 20 μm . Images were acquired every 120 s. Frame rate is 10 fps.

722

723 **Video S5:** Time-lapse imaging of CellMask-Actin-GFP (inverted grey or green) and
724 Membranes-tdTomato (magenta) in organoid derived-monolayers after blebbistatin treatment
725 and subsequent wash-out. Scale Bar, 10 μm . Images were acquired every 120 s. Frame rate
726 is 10 fps.

727

728 **Video S6:** Time-lapse imaging of CellMask-Actin-GFP (grey) in organoid derived-monolayers
729 after laser ablation of around a single AcS node along the yellow circle. Tracked AcS nodes
730 trajectories from ablation center are indicated with colored lines, with node '1' (N1) in red
731 indicating immediate neighbour to the ablated node, N2 in green neighbouring N1, N3 in cyan
732 neighbouring N2, N4 in blue neighbouring N3, N5 in magenta neighbouring N4, N6 in yellow
733 neighbouring N5. Scale bar, 10 μm . Images were acquired every 1.1 s. Frame rate is 10 fps.

734

735 **Video S7:** Time-lapse imaging of CellMask-Actin-GFP (inverted grey or green) and
736 Membranes-tdTomato (red) and Hoechst 33342 stained nucleus (blue) in organoid derived-
737 monolayers after laser ablation around a single AcS node indicated with orange circle. Scale
738 bar 10 μm . Images were acquired every 1.56 s. Frame rate is 10 fps.

739

740

741

742

743

744

745 **STAR METHOD**

746

747 **RESOURCE AVAILABILITY**

748

749 ***Lead contact***

750 Further information and requests for resources and reagents should be directed and will be
751 fulfilled by the lead contact Delphine Delacour (delphine.delacour@univ-amu.fr).

752

753 ***Materials availability***

754 Materials generated in the current study are available from the lead contacts upon request.
755 There are restrictions to the availability of due to collaborations or MTAs.

756

757 ***Data and code availability***

758 Source data files have been deposited at XXX and are publicly available as of the date of
759 publication. The DOI is listed in the key resources table. Microscopy data reported in this paper
760 will be shared by the lead contact on request. Any additional information required to re-analyze
761 the data reported in this paper is available from the lead contact upon request.

762

763

764 **EXPERIMENTAL MODEL AND SUBJECT DETAILS**

765

766 ***Organoid cultures and transfection***

767 Wild-type C57/Bl6 adult male mice were provided by the animal house facility of the Institut
768 Jacques Monod and by Charles River company (France). Mice were housed in EOPS
769 (Environment without Specific Pathogenic Organisms) environment, and handled in
770 accordance with French regulation for animal care. VillinCreERT2-tdTomato organoids were
771 generated from mice provided by Danijela Vignjevic (Institut Curie, Paris)⁵⁴. Myosin-IIA-GFP-
772 knock-in mice⁵⁵ were provided by Robert S. Adelstein (NHLBI, Bethesda) and Ana-Maria
773 Lennon-Dumesnil (Institut Curie, Paris). Myosin-IIA-KO/mTmG mice were kindly provided by
774 Danijela Vignjevic (Institut Curie, Paris)^{54,56}. Cre recombinase for Myosin-IIA-KO was induced
775 with 100nM of 4-hydroxytamoxifen for 24h (#SML1666, Sigma-Aldrich).

776

777 **METHOD DETAILS**

778

779 ***Organoid preparation***

780 6 to 12 weeks-old mice were used for organoid generation. After euthanization by cervical
781 dislocation, the small intestine was harvested, flushed with PBS to discard luminal content and
782 cut longitudinally open. The tissue was then cut into small pieces of 3-5 mm and further
783 washed in PBS.

784 For organoid preparation, the pieces of intestinal tissue were then incubated on ice for 10 min
785 in a tube containing 5 mM EDTA. The tube was then vortexed for 2 min to release villi from
786 the tissue. After EDTA removal, the intestinal pieces were placed in cold PBS and vortexed
787 vigorously for 3 min to ensure crypt release. This process was repeated 3 times, with each
788 fraction recovered. The third and fourth fractions are usually concentrated in crypts, so these
789 are combined and passed through a 70- μ m cell strainer to remove remaining villi and
790 centrifuged at 1000 RPM for 5 min. The pellet (crypts) was then washed in advanced
791 DMEM/F12 (#12634010 Thermo Fisher Scientific, Waltham, Massachusetts, USA) and
792 centrifuged. The final pellet is resuspended in 50 μ l of 1:1 ratio of advanced DMEM/F12 and
793 ice-cold Matrigel (#734-1100 VWR, Radnor, PA, USA) and plated as domes. Incubation at
794 37°C for 20-30 min allowed Matrigel polymerization. 3D organoid culture was performed in
795 IntestiCult™ Organoid Growth medium (#06005 StemCell Technologies, Vancouver,
796 Canada), from here on termed ENR medium. Organoid stocks were routinely grown in Matrigel
797 with IntestiCult™ Organoid Growth medium and passaged every 7 to 10 days. Medium was
798 changed every 2 days.

799 For 2D organoid monolayer preparation, 3D organoids were cultured in L-WRN conditioned
800 media for at least 3 days before use. Organoids were harvested with cold advanced
801 DMEM/F12 and transferred in a falcon tube. Organoids were mechanically broken through a
802 P200-filtered tip 150 times. The solution of broken organoids was centrifuged at 72g for 3 mins
803 at 4°C. The supernatant was removed and 5 mL of fresh F12 was added. The breaking step
804 and centrifugation were repeated once. Then the cell pellet was filtered through a 30 μ m cell
805 strainer. The pellet was resuspended in warm L-WRN conditioned media + 10 μ M Y27632
806 (StemCell #72302) and 150 μ L of were gently seeded on the crosslinked Matrigel substrate
807 (18 mm coated coverslips on a 12 well plate) making sure the solution stays on the coverslip.
808 After 4h of incubation in a 37°C incubator, more L-WRN conditioned media + 10 μ M Y27632
809 (up to 1 mL/well) were added for the first 24h culture. After 24h, cells were subsequently grown
810 on L-WRN conditioned media (without Y27632). Culture media were replaced every 24-48
811 hours with fresh L-WRN conditioned media and the organoid-derived monolayers were
812 cultured for 10 days before immunostaining or live imaging.

813

814 ***Preparation of L-WRN conditioned medium***

815 The L-WRN conditioned media was prepared from L-WRN cells, acquired from ATCC (ATCC
816 CRL-3276), according to Miyoshi and Stappenbeck⁵⁷. L-WRN cells were cultured in L-Cell

817 medium (DMEM high glucose (Sigma-Aldrich, cat. no. D6429) supplemented with FBS (10%
818 v/v), Glutamax (2 mM) and penicillin/streptomycin (100 units/mL). After the first day, selection
819 media was added, containing Geneticin (500 µg/mL) and hygromycin (500 µg/mL). Once
820 confluent cells were passed into five T175 flask and cultured in L-cells media until confluency.
821 Then cells were cultured in Primary Cells Medium (PCM) (Advanced DMEM/F12
822 supplemented with FBS (20% v/v), Glutamax (2 mM) and penicillin/streptomycin (100 units/mL).
823 The PCM supplemented with Wnt-3a, R-spondin and Noggin secreted by the L-WRN cells
824 was collected every 24h and mixed with freshly made PCM at a 1:1 ratio and was vacuum
825 filtered through 0.22 µm membrane membrane to make EM.

826

827 **Human biopsies and preparation of tissue samples**

828 Tissue samples of human duodenum were provided by Necker-Enfants Malades Hospital
829 (Paris, France) and were collected from the Necker Paediatric Anatomic-Pathology
830 Department for retrospective analyses. The biopsies analyzed here comprised 1 patient with
831 gastralgia, 1 patient with anemia, and 1 patient with coeliac disease under gluten-free diet.
832 Duodenal biopsies were collected during endoscopic procedures for diagnosis and/or
833 monitoring of patients. All parents signed informed consent forms approved by the local ethics
834 committee for biopsy exploitation (Unité de Recherche Clinique (URC) of Necker Hospital,
835 URC). For immunohistochemical analyses, biopsies were fixed for 2 h in 4% formaldehyde.
836 The samples were then paraffin embedded. 5 µm sections were de-waxed in a xylene bath,
837 rehydrated in isopropanol and in solutions with decreasing ethanol concentrations, and were
838 processed for immunostaining. De-waxed tissue sections were blocked in 1.5% donkey serum
839 (Sigma-Aldrich, St Louis, Missouri, USA) for 1 h. Primary antibody incubations were performed
840 at 4°C overnight and secondary antibody incubations at room temperature for 2 h, both in
841 1.5% donkey serum solution. Hoechst 33342 staining (Life Technologies, Paisley, UK) was
842 used to detect nuclei. Tissue sections were mounted in home-made Mowiol 488 solution.

843

844 ***Caco2 cell culture***

845 Caco2 cells, originally acquired from ATCC, were kindly provided by Dr. S. Robine (Curie
846 Institute, Paris). Caco2 cells were routinely grown in DMEM 4.5 g/l glucose supplemented with
847 20% fetal bovine serum and 1% penicillin-streptomycin (Gibco, Thermo Fischer Scientific,
848 Waltham, MA, USA) for a maximum of 9 passages. The culture medium was renewed every
849 2-days.

850

851 ***Cross-linked Matrigel substrates (CL-Matrigel)***

852 To produce cross-linked Matrigel (CL-Matrigel) substrates, a fresh-made cross-linker solution
853 was prepared by mixing 100 mM NHS (Sigma-Aldrich) and 400 mM EDC (Sigma-Aldrich) in

854 cold PBS 4°C. Glass coverslips ($\varnothing = 18$ mm) were plasma treated and then were cooled in a
855 fridge (-20°C, 3 min). Cross-linker solution then was mixed well with thawed pure Matrigel at
856 a ratio of 1:10 (v/v) and 50 μ L drops of the mixture were then poured on top of the cooled
857 plasma treated coverslip and were spread by tilting the coverslips. Subsequently, the
858 coverslips were placed in a 37°C incubator in a 12 well plate for 2h to form CL-Matrigel layers.
859 While incubation, PBS were poured in 2 empty wells of the 12 well plate ware to prevent gel
860 dehydration. The CL-Matrigel substrates were washed with PBS once and incubated in PBS
861 at 37°C for 24 h to remove unreacted EDC and NHS. The substrates can be stored up to a
862 week in incubator 1X PBS for future utilization. Before use, the coverslips were washed 2
863 times with 1X PBS.

864

865 ***Glass coverslip micropatterning with deep UV and cell seeding***

866 The micropatterning protocol was adapted from ⁵⁸. For polystyrene coating, 20x20 glass
867 coverslips (1304369, Schott) were cleaned for 10min in acetone then for 10min in isopropanol
868 in a bath sonicator and then dried with compressed-clean air under a laminar flow hood. They
869 were first coated with adhesion promoter Ti-Prime (MicroChemicals) using a spin-coater (WS-
870 650m2-23NPPB, Laurell) at 3000 rpm for 30s and baked on top heater for 2min at 120°C.
871 Then a 1% polystyrene (MW 260,000, 178891000, Acros Organic) solution in toluene (179418,
872 Sigma-Aldrich) was spin-coated on the coverslip at 1000 rpm.

873 For coverslip passivation, polystyrene layer was oxidized by exposure to air-plasma as
874 described above and immersed into a solution of poly(L-lysine)-graft-poly(ethylene glycol)
875 (PLL-g-PEG) (ZZ241PO22, JenKem Technology, Beijing) at 0.1 mg/mL in HEPES (10mM, pH
876 7.4) for 1 hour at room temperature. Coverslips were then washed in HEPES buffer and air
877 dried.

878 For coverslip micropatterning, passivated coverslips were put in tight contact with a chromed
879 etched photomask (Toppan Photomask). Tight contact was maintained using a homemade
880 vacuum holder. The PLL-PEG layer was burned with deep UV ($\lambda=190$ nm) through the etched
881 windows of the photomask, using UVO cleaner (Model No. 342A-220, Jelight), at a distance
882 of 1cm from the UV lamp with a power of 6mW/cm², for 3 min. Exposed coverslips were then
883 incubated with a solution of 10 μ g/ml fibronectin (F1141, Sigma) in carbonate buffer (100 mM
884 NaHCO₃ buffer, pH 8.5) for 30min at room temperature. Micropatterned coverslips were then
885 washed with the carbonate buffer. Caco2 cells were directly seeded on these micropatterned
886 coverslips on a 35 mm petri dish and were grown for 4 – 5 days.

887

888 ***Immunostaining***

889 Routinely, organoid-derived monolayers were fixed using 4% paraformaldehyde for 30 min,
890 then permeabilized using 0.1% triton-x-100 in PBS for 10-15 min. The blocking step was

891 performed in 4% goat serum /1% BSA solution for 1 hour, before proceeding to incubation
892 with primary antibody at 4°C overnight. The next day, the primary antibody was removed and
893 the monolayers were washed 3 times in PBS for 10 min each, before adding the secondary
894 antibody and left to incubate for 2h at room temperature. Finally, monolayers were washed 3
895 times again for 10 minutes before incubating in Hoechst 33342 for 15 min to stain nuclei.
896 Immunostained samples were mounted in homemade Mowiol solution. For F-actin staining,
897 fluorescently labelled phalloidin was added during secondary antibody incubation.
898 For immunostaining of *in vivo* mouse intestine, 1-mm pieces of mouse jejunum were fixed in
899 4% PFA overnight under shaking for 1 hour. After PBS wash, tissue permeabilization was
900 performed in 1% Triton X-100 / PBS solution for 1 h, before blocking in 1% BSA / 4% goat
901 serum / 0.2% Triton X-100 / PBS solution for 1 h. Incubations with primary and secondary
902 antibodies were done in 0.1% BSA / 0.3 % goat serum / 0.2 % Triton X-100 / PBS overnight
903 at 4°C. Hoechst33342 staining was used to detect nuclei. Immunostained samples were
904 mounted in Vectashield (Vector Laboratories, Burlingame, CA).

905

906 ***Antibodies and reagents***

907 Mouse monoclonal antibody directed against X (clone X, IF dilution, 1:100) was purchased
908 from Sigma-Aldrich. Mouse monoclonal antibody directed against E-cadherin (clone 36,
909 #610181, IF dilution, 1:50) was from BD Biosciences. Rabbit polyclonal antibody directed
910 against Phospho-Myosin Light Chain 2 (Ser19, #3671, IF dilution, 1:100) and rabbit
911 monoclonal antibody directed against E-cadherin (clone 24E10, #3195S, IF dilution 1:100)
912 were from Cell Signaling Technology. Rabbit polyclonal antibody directed against non-muscle
913 myosin heavy chain II-A antibody (clone poly19098, #909801, WB dilution 1:500) was from
914 Biologend. Goat anti-mouse-Alexa-488, 568, anti-rabbit-Alexa488, 568 or 647 were from Life
915 Technologies (Paisley, UK). Nuclei were stained with Hoechst 33342 solution incubation (Life
916 Technologies) at a 1:1000 dilution. Blebbistatin, Y-27632 and nocodazole were from Sigma
917 Aldrich (Saint-Louis, MO, USA). CellMask Actin Deep Red actin tracking stain (#A57245) was
918 from Invitrogen (Thermo Fisher Scientific). Azidoblebbistatin (#MPH-198) was from
919 MotorPharma (Budapest, Hungary).

920

921 ***Drug treatments***

922 Organoids were incubated in 10µM blebbistatin for 1.5h, then washed out with PBS and
923 prepared for immunostaining or live-imaging. Cells were incubated for 1.5h in DMSO as
924 controls. For live blebbistatin photo-activation organoid derived monolayer were first stained
925 with CellMask actin GFP and then were incubated with 10µM azidoblebbistatin (Cat#DR-A-
926 081, Motor pharma) or DMSO controls for 1h. The samples were then was taken for live
927 imaging in a LSM 980 scanning probe microscope equipped with a multiphoton setup.

928 Azidoblebbistatin was photoactivated in the selected ROI using a 2-photon 800 nm laser
929 irradiation⁵⁹ and live images were acquired.

930

931 ***Laser ablation experiments***

932 For Laser ablation experiments, F-actin was first labelled in live organoid-derived monolayers
933 by incubating with CellMask™ Green Actin Tracking stain (Invitrogen) for 1 hour in culture
934 media. Labelled monolayer was then taken in a live imaging setup on a spinning disc confocal
935 microscope (CSU-XI) equipped with laser ablation setup. The ablation was done using a
936 pulsed 355 nm UV at a power of 25% using an iLas system (Roper Scientific) in Metamorph
937 and images were obtained using a 40x or 100X oil objective. Node displacement was manually
938 tracked using TrackMate in imageJ.

939

940 ***Live imaging***

941 Dynamics experiments on live organoid-derived monolayers were performed on a live imaging
942 setup on an inverted Zeiss microscope equipped with a CSU-X1 spinning disk head
943 (Yokogawa – Andor), using Zeiss 40X and 63X objectives.

944

945 ***Segmentation and analyses***

946 Segmentation - We used CellPose 2.0 (<https://www.cellpose.org/>; ⁶⁰) to perform cell
947 segmentation. Mask dilatation was used to extract the cell contours and location of tricellular
948 junctions, called vertices.

949

950 Hexatic order analysis- For each cell (indexed by $J = 1, 2, 3, \dots, N$ with N the total number of
951 cells), we define a hexatic order parameter value:

$$952 \quad \psi_{6,J} = \frac{1}{N_J} \sum_{K \in \text{neighbors}} \exp(i6\theta_{JK}),$$

953 where $\theta_{JK} = \arg(r_K - r_J)$, is the angle between the considered cell center, denoted r_J , and
954 the one of its neighbour, r_K ; N_J is the number of neighbor cells of the J -th cell. The overall

955 hexatic order is then defined as $\psi_6 = \frac{|\sum_{J=1}^N \psi_{6,J}|}{N}$.

956 Triangular order We define a triangular order parameter value:

$$957 \quad \psi_{3,i} = \frac{1}{3} \sum_{j \in \text{neighbors}} \exp(i3\theta_{ij}),$$

958 where $\theta_{ij} = \arg(r_j - r_i)$, is the angle of the cell-cell junction ij . The overall triangular order
959 is then defined as $\psi_3 = \frac{\sum_{i=1}^{N_v} |\psi_{3,i}|}{N_v}$.

960 Strain For each detected cells, we estimate a cell shape tensor Λ whose xx components read:

961
$$\Lambda_{xx} = \sum_{n \in \text{boundary}} (x_n - x^-)^2$$

962 where (x_n, y_n) is the coordinate of the boundary pixels n and $(x^-, y^-) = \sum_n \frac{(x_n, y_n)}{n}$ is the cell
963 barycenter; the xy and yy components are defined similarly. The matrix Λ has positive
964 eigenvalues Λ_1 and Λ_2 with $\Lambda_1 \geq \Lambda_2$. We then define the cellular strain as:

965
$$\varepsilon_{el} = \frac{1}{2} \log \left(\frac{\Lambda_1}{\Lambda_2} \right)$$

966 In the strain quantification, we exclude detected objects with an area smaller than 2 microns.

967 Tracking We used StarDist in TrackMate (Fiji⁶¹) for cell tracking analyses. We used a Kalman
968 tracker parameterized with a search radius of approximately half the cell typical size, an initial
969 search radius 10% higher, and a maximum frame gap of 2^{62,63}.

970

971 Velocity Correlation Functions For every cells, with position r_i , we compute the velocity
972 autocorrelation function:

973
$$C_t(\tau) = C(r_i, t) = v(r_i, t) \cdot v \frac{(r_i, t + \tau)}{|v(r_i, t)|^2},$$

974 where τ is the delay time. We also evaluate the spatial velocity correlation function:

975
$$C_s(r) = C(r, t) = v(r_i, t) \cdot v \frac{(r_i + r, t)}{|v(r_i, t)|^2},$$

976 where $r = r_j - r_i$ and r_j is the position of the cell j . For each experiment, we estimate the
977 average correlation function $\langle C_s(r) \rangle$ over all tracks and all times (see Figure 7E-J in the
978 main text).

979 Practically, in our evaluation of the velocity functions, we discarded every track which was
980 shorter than 4 frames.

981

982 **Computational model**

983 We employed a cell-based computational model, called the vertex model^{64,65,66}, to simulate
 984 the multicellular response of cell differentiation, cell ablation, and contractility recovery of
 985 multicellular actin star network. In this model, the cell monolayer is represented as a tiling of
 986 polygons, see Figure 6D. The dynamics of cells are determined by force balance equations at
 987 each vertex:

$$988 \quad F_i^{(friction)} + F_i^{(viscous)} + F_i^{(elastic)} + F_i^{(active)} = 0$$

989 where (1) $F_i^{(friction)} = -\xi v_i$ is the friction force between the monolayer and the substrate,

990 with ξ being the friction coefficient and $v_i = d \frac{r_i}{dt}$ being the velocity of the vertex i . (2)

991 $F_i^{(viscous)} = \eta \sum_j C_{ij} \cdot v_j$ is the viscous force at vertex i , which depends on the velocities of the

992 neighbor vertices j and scales proportionally to a viscous modulus η that models dissipation

993 along the cell-cell junction and within the bulk cytoplasm; C_{ij} is a viscous structure tensor that

994 depends on the vertices' positions (r_i), and the topological relation of cells and vertices⁶⁷ (see

995 Supplementary Information); (3) $F_i^{(elastic)}$ is the elastic force stemming from variations in the

996 cell shape, classically expressed as $F_i^{(elastic)} = -\partial \frac{E}{\partial} r_i$ with^{65,68,67,69,70}:

$$997 \quad E = \sum_{J=1}^N \frac{1}{2} K_A (A_J - A_0)^2 + \sum_{J=1}^N \frac{1}{2} K_P (P_J - P_0)^2,$$

998 where K_A and K_P are the rigidities associated with cell area and cell perimeter; A_0 and P_0 are

999 the preferred cell area and the preferred cell perimeter, respectively; A_J and P_J are the actual

1000 area and perimeter of the J -th cell, respectively. (4) the active force $F_i^{(active)}$ corresponds to

1001 the forces induced by the multicellular actin star network; we decompose the actin star network

1002 into two contributions, resulting from: (4.1) an active pulling stress $\sigma_J^{(active,\perp)} = \alpha_J I$ with $\alpha_J \geq$

1003 0 quantifies the intensity of the active pulling stress induced by the contractility of the actin

1004 star network within the J -th cell, which describes the active pulling force normal to cell edges,

1005 see Supplementary Information, Figure S1; and (4.2) an active tension $\chi_J > 0$ parallel to

1006 edges of the J -th cell, see Supplementary Information, Figure S1. We show that the active

1007 pulling stress α_J and the active tension χ_J are equivalent to renormalizing E into E_{eff} with a

1008 renormalized target area $A_{0,J} = A_0 - \frac{\alpha_J}{K_A}$ and a renormalized target perimeter $P_{0,J} = P_0 -$

1009 $\frac{\chi_J}{(2K_P)}$ (see Supplementary Materials). Consequently, we obtain the following dynamic equation

1010 on the velocities:

$$1011 \quad -\xi v_i + \sum_j \eta C_{ij} \cdot v_j = \frac{\partial E_{eff}}{\partial r_i}$$

1012 We then solve the latter equation to estimate the vertex displacement at each simulation time
1013 step. Last, we mention that in the laser ablation simulations, the cells at the k -th row are
1014 defined by the distance d of the cell centre to the ablation site if it satisfies $k-1/2 < d/L_{\text{cell}} <$
1015 $k+1/2$ with $L_{\text{cell}} = 10 \mu\text{m}$ being the cell size.

1016

1017 ***Statistical analysis***

1018 All statistical analyses were performed using Prism (GraphPad Software, San Diego, CA,
1019 USA, version 9.0). Statistical details of experiments can be found in the figure legends. Unless
1020 otherwise stated, experiments were replicated 3 times independently.

1021

1022 **REFERENCES**

1023

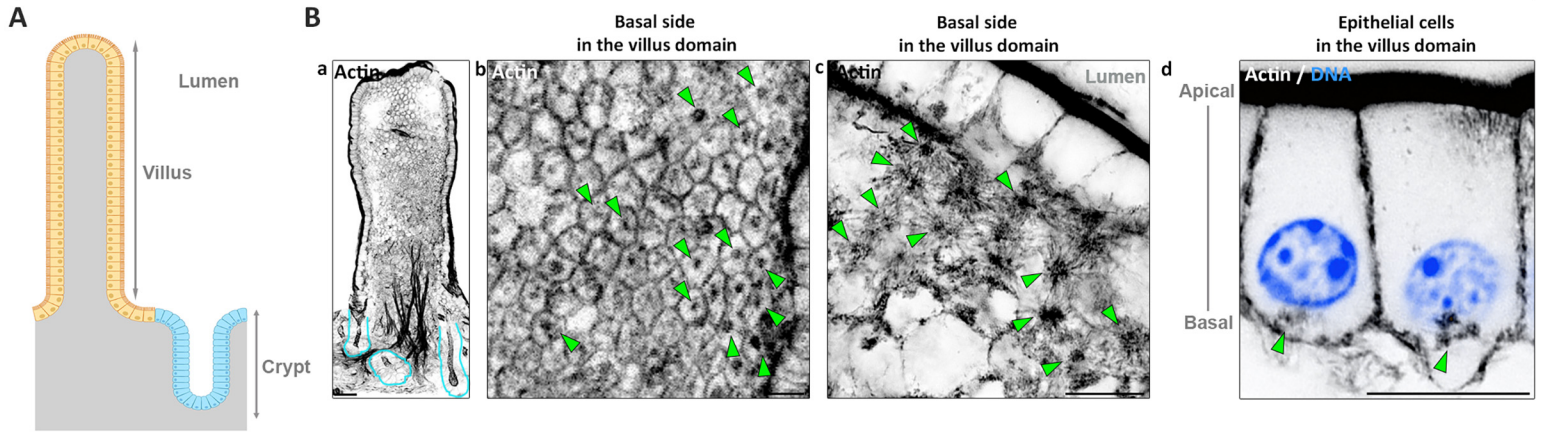
- 1024 1. Lecuit, T., Lenne, P.F., and Munro, E. (2011). Force generation, transmission, and
1025 integration during cell and tissue morphogenesis. *Annu Rev Cell Dev Biol* 27, 157-184.
1026 10.1146/annurev-cellbio-100109-104027.
- 1027 2. Levayer, R., and Lecuit, T. (2013). Oscillation and polarity of E-cadherin asymmetries
1028 control actomyosin flow patterns during morphogenesis. *Dev Cell* 26, 162-175.
1029 10.1016/j.devcel.2013.06.020.
- 1030 3. Sanchez-Corrales, Y.E., and Roper, K. (2018). Alignment of cytoskeletal structures
1031 across cell boundaries generates tissue cohesion during organ formation. *Curr Opin*
1032 *Cell Biol* 55, 104-110. 10.1016/j.ceb.2018.07.001.
- 1033 4. Vicente-Manzanares, M., Ma, X., Adelstein, R.S., and Horwitz, A.R. (2009). Non-
1034 muscle myosin II takes centre stage in cell adhesion and migration. *Nat Rev Mol Cell*
1035 *Biol* 10, 778-790. 10.1038/nrm2786.
- 1036 5. McCaffrey, L.M., and Macara, I.G. (2011). Epithelial organization, cell polarity and
1037 tumorigenesis. *Trends Cell Biol* 21, 727-735. 10.1016/j.tcb.2011.06.005.
- 1038 6. Buckley, C.E., and St Johnston, D. (2022). Apical-basal polarity and the control of
1039 epithelial form and function. *Nat Rev Mol Cell Biol* 23, 559-577. 10.1038/s41580-022-
1040 00465-y.
- 1041 7. Thompson, D.W. (1942). *On growth and form*. Macmillan, Cambridge University
1042 Press.
- 1043 8. Pickett, M.A., Nature, V.F., and Feldman, J.L. (2019). A Polarizing Issue: Diversity in
1044 the Mechanisms Underlying Apico-Basolateral Polarization In Vivo. *Annu Rev Cell Dev*
1045 *Biol* 35, 285-308. 10.1146/annurev-cellbio-100818-125134.
- 1046 9. Furukawa, K.T., Yamashita, K., Sakurai, N., and Ohno, S. (2017). The Epithelial
1047 Circumferential Actin Belt Regulates YAP/TAZ through Nucleocytoplasmic Shuttling of
1048 Merlin. *Cell Rep* 20, 1435-1447. 10.1016/j.celrep.2017.07.032.
- 1049 10. Tepass, U., Truong, K., Godt, D., Ikura, M., and Peifer, M. (2000). Cadherins in
1050 embryonic and neural morphogenesis. *Nat Rev Mol Cell Biol* 1, 91-100.
1051 10.1038/35040042.
- 1052 11. Campas, O., Noordstra, I., and Yap, A.S. (2023). Adherens junctions as molecular
1053 regulators of emergent tissue mechanics. *Nat Rev Mol Cell Biol*. 10.1038/s41580-023-
1054 00688-7.
- 1055 12. Guillot, C., and Lecuit, T. (2013). Mechanics of epithelial tissue homeostasis and
1056 morphogenesis. *Science* 340, 1185-1189. 10.1126/science.1235249.
- 1057 13. Heisenberg, C.P., and Bellaiche, Y. (2013). Forces in tissue morphogenesis and
1058 patterning. *Cell* 153, 948-962. 10.1016/j.cell.2013.05.008.
- 1059 14. Martin, A.C., Kaschube, M., and Wieschaus, E.F. (2009). Pulsed contractions of an
1060 actin-myosin network drive apical constriction. *Nature* 457, 495-499.
1061 10.1038/nature07522.
- 1062 15. Rauzi, M., Lenne, P.F., and Lecuit, T. (2010). Planar polarized actomyosin contractile
1063 flows control epithelial junction remodelling. *Nature* 468, 1110-1114.
1064 10.1038/nature09566.
- 1065 16. Jodoin, J.N., Coravos, J.S., Chanet, S., Vasquez, C.G., Tworoger, M., Kingston, E.R.,
1066 Perkins, L.A., Perrimon, N., and Martin, A.C. (2015). Stable Force Balance between
1067 Epithelial Cells Arises from F-Actin Turnover. *Dev Cell* 35, 685-697.
1068 10.1016/j.devcel.2015.11.018.
- 1069 17. Coravos, J.S., and Martin, A.C. (2016). Apical Sarcomere-like Actomyosin Contracts
1070 Nonmuscle *Drosophila* Epithelial Cells. *Dev Cell* 39, 346-358.
1071 10.1016/j.devcel.2016.09.023.
- 1072 18. Bailles, A., Collinet, C., Philippe, J.M., Lenne, P.F., Munro, E., and Lecuit, T. (2019).
1073 Genetic induction and mechanochemical propagation of a morphogenetic wave.
1074 *Nature* 572, 467-473. 10.1038/s41586-019-1492-9.

- 1075 19. Keller, R. (2006). Mechanisms of elongation in embryogenesis. *Development* 133,
1076 2291-2302. 10.1242/dev.02406.
- 1077 20. Lawson-Keister, E., and Manning, M.L. (2021). Jamming and arrest of cell motion in
1078 biological tissues. *Curr Opin Cell Biol* 72, 146-155. 10.1016/j.ceb.2021.07.011.
- 1079 21. Xi, W., Saleh, J., Yamada, A., Tomba, C., Mercier, B., Janel, S., Dang, T., Soleilhac,
1080 M., Djemat, A., Wu, H., et al. (2022). Modulation of designer biomimetic matrices for
1081 optimized differentiated intestinal epithelial cultures. *Biomaterials* 282, 121380.
1082 10.1016/j.biomaterials.2022.121380.
- 1083 22. Thorne, C.A., Chen, I.W., Sanman, L.E., Cobb, M.H., Wu, L.F., and Altschuler, S.J.
1084 (2018). Enteroid Monolayers Reveal an Autonomous WNT and BMP Circuit Controlling
1085 Intestinal Epithelial Growth and Organization. *Dev Cell* 44, 624-633 e624.
1086 10.1016/j.devcel.2018.01.024.
- 1087 23. Perez-Gonzalez, C., Ceada, G., Greco, F., Matejic, M., Gomez-Gonzalez, M., Castro,
1088 N., Menendez, A., Kale, S., Krndija, D., Clark, A.G., et al. (2021). Mechanical
1089 compartmentalization of the intestinal organoid enables crypt folding and collective cell
1090 migration. *Nat Cell Biol* 23, 745-757. 10.1038/s41556-021-00699-6.
- 1091 24. Murrell, M.P., and Gardel, M.L. (2012). F-actin buckling coordinates contractility and
1092 severing in a biomimetic actomyosin cortex. *Proc Natl Acad Sci U S A* 109, 20820-
1093 20825. 10.1073/pnas.1214753109.
- 1094 25. Sonal, Ganzinger, K.A., Vogel, S.K., Mucksch, J., Blumhardt, P., and Schwille, P.
1095 (2018). Myosin-II activity generates a dynamic steady state with continuous actin
1096 turnover in a minimal actin cortex. *J Cell Sci* 132. 10.1242/jcs.219899.
- 1097 26. Tse, J.R., and Engler, A.J. (2010). Preparation of hydrogel substrates with tunable
1098 mechanical properties. *Curr Protoc Cell Biol Chapter 10*, Unit 10 16.
1099 10.1002/0471143030.cb1016s47.
- 1100 27. Henkes, S., Kostanjevec, K., Collinson, J.M., Sknepnek, R., and Bertin, E. (2020).
1101 Dense active matter model of motion patterns in confluent cell monolayers. *Nat*
1102 *Commun* 11, 1405. 10.1038/s41467-020-15164-5.
- 1103 28. Iskratsch, T., Wolfenson, H., and Sheetz, M.P. (2014). Appreciating force and shape-
1104 the rise of mechanotransduction in cell biology. *Nat Rev Mol Cell Biol* 15, 825-833.
1105 10.1038/nrm3903.
- 1106 29. Wolfenson, H., Yang, B., and Sheetz, M.P. (2019). Steps in Mechanotransduction
1107 Pathways that Control Cell Morphology. *Annu Rev Physiol* 81, 585-605.
1108 10.1146/annurev-physiol-021317-121245.
- 1109 30. Lappalainen, P., Kotila, T., Jegou, A., and Romet-Lemonne, G. (2022). Biochemical
1110 and mechanical regulation of actin dynamics. *Nat Rev Mol Cell Biol* 23, 836-852.
1111 10.1038/s41580-022-00508-4.
- 1112 31. Lazarides, E. (1976). Actin, alpha-actinin, and tropomyosin interaction in the structural
1113 organization of actin filaments in nonmuscle cells. *J Cell Biol* 68, 202-219.
1114 10.1083/jcb.68.2.202.
- 1115 32. Duffy, L., and O'Reilly, S. (2018). Functional Implications of Cross-Linked Actin
1116 Networks in Trabecular Meshwork Cells. *Cell Physiol Biochem* 45, 783-794.
1117 10.1159/000487170.
- 1118 33. Peng, M., Rayana, N.P., Dai, J., Sugali, C.K., Baidouri, H., Suresh, A., Raghunathan,
1119 V.K., and Mao, W. (2022). Cross-linked actin networks (CLANs) affect stiffness and/or
1120 actin dynamics in transgenic transformed and primary human trabecular meshwork
1121 cells. *Exp Eye Res* 220, 109097. 10.1016/j.exer.2022.109097.
- 1122 34. Xia, S., Lim, Y.B., Zhang, Z., Wang, Y., Zhang, S., Lim, C.T., Yim, E.K.F., and
1123 Kanchanawong, P. (2019). Nanoscale Architecture of the Cortical Actin Cytoskeleton
1124 in Embryonic Stem Cells. *Cell Rep* 28, 1251-1267 e1257.
1125 10.1016/j.celrep.2019.06.089.
- 1126 35. Luo, W., Yu, C.H., Lieu, Z.Z., Allard, J., Mogilner, A., Sheetz, M.P., and Bershadsky,
1127 A.D. (2013). Analysis of the local organization and dynamics of cellular actin networks.
1128 *J Cell Biol* 202, 1057-1073. 10.1083/jcb.201210123.

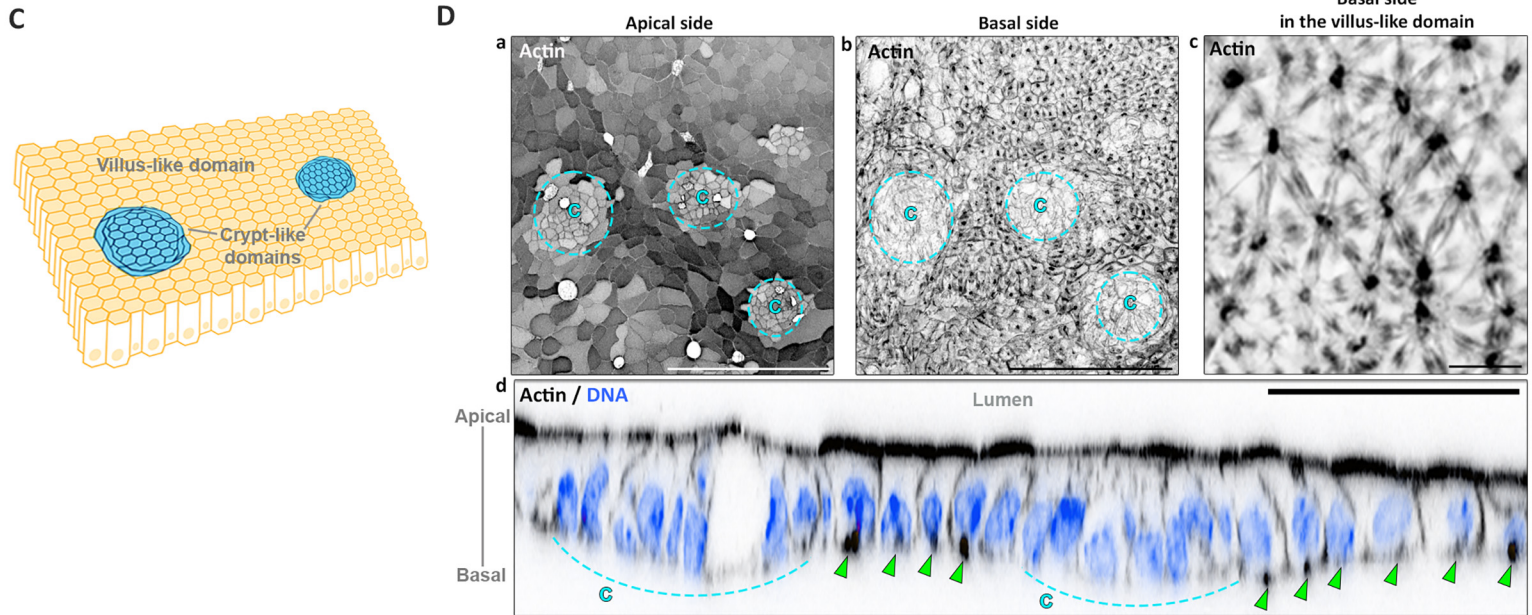
- 1129 36. Vogel, S.K., Heinemann, F., Chwastek, G., and Schwille, P. (2013). The design of
1130 MACs (minimal actin cortices). *Cytoskeleton (Hoboken)* 70, 706-717.
1131 10.1002/cm.21136.
- 1132 37. Muresan, C.G., Sun, Z.G., Yadav, V., Tabatabai, A.P., Lanier, L., Kim, J.H., Kim, T.,
1133 and Murrell, M.P. (2022). F-actin architecture determines constraints on myosin thick
1134 filament motion. *Nat Commun* 13, 7008. 10.1038/s41467-022-34715-6.
- 1135 38. Putra, V.D.L., Kilian, K.A., and Knothe Tate, M.L. (2023). Biomechanical, biophysical
1136 and biochemical modulators of cytoskeletal remodelling and emergent stem cell
1137 lineage commitment. *Commun Biol* 6, 75. 10.1038/s42003-022-04320-w.
- 1138 39. Humphrey, J.D., Dufresne, E.R., and Schwartz, M.A. (2014). Mechanotransduction
1139 and extracellular matrix homeostasis. *Nat Rev Mol Cell Biol* 15, 802-812.
1140 10.1038/nrm3896.
- 1141 40. Paluch, E.K., Nelson, C.M., Biais, N., Fabry, B., Moeller, J., Pruitt, B.L., Wollnik, C.,
1142 Kudryasheva, G., Rehfeldt, F., and Federle, W. (2015). Mechanotransduction: use the
1143 force(s). *BMC Biol* 13, 47. 10.1186/s12915-015-0150-4.
- 1144 41. Elosegui-Artola, A., Trepats, X., and Roca-Cusachs, P. (2018). Control of
1145 Mechanotransduction by Molecular Clutch Dynamics. *Trends Cell Biol* 28, 356-367.
1146 10.1016/j.tcb.2018.01.008.
- 1147 42. Sumigray, K.D., Terwilliger, M., and Lechler, T. (2018). Morphogenesis and
1148 Compartmentalization of the Intestinal Crypt. *Dev Cell* 45, 183-197 e185.
1149 10.1016/j.devcel.2018.03.024.
- 1150 43. Hartl, L., Huelsz-Prince, G., van Zon, J., and Tans, S.J. (2019). Apical constriction is
1151 necessary for crypt formation in small intestinal organoids. *Dev Biol* 450, 76-81.
1152 10.1016/j.ydbio.2019.03.009.
- 1153 44. Yang, Q., Xue, S.L., Chan, C.J., Rempfler, M., Vischi, D., Maurer-Gutierrez, F., Hiragi,
1154 T., Hannezo, E., and Liberali, P. (2021). Cell fate coordinates mechano-osmotic forces
1155 in intestinal crypt formation. *Nat Cell Biol* 23, 733-744. 10.1038/s41556-021-00700-2.
- 1156 45. Barker, N. (2014). Adult intestinal stem cells: critical drivers of epithelial homeostasis
1157 and regeneration. *Nat Rev Mol Cell Biol* 15, 19-33. 10.1038/nrm3721.
- 1158 46. Delacour, D., Salomon, J., Robine, S., and Louvard, D. (2016). Plasticity of the brush
1159 border - the yin and yang of intestinal homeostasis. *Nat Rev Gastroenterol Hepatol*.
1160 10.1038/nrgastro.2016.5.
- 1161 47. Keller, T.C., 3rd, Conzelman, K.A., Chasan, R., and Mooseker, M.S. (1985). Role of
1162 myosin in terminal web contraction in isolated intestinal epithelial brush borders. *J Cell*
1163 *Biol* 100, 1647-1655.
- 1164 48. Meenderink, L.M., Gaeta, I.M., Postema, M.M., Cencer, C.S., Chinowsky, C.R.,
1165 Krystofiak, E.S., Millis, B.A., and Tyska, M.J. (2019). Actin Dynamics Drive Microvillar
1166 Motility and Clustering during Brush Border Assembly. *Dev Cell* 50, 545-556 e544.
1167 10.1016/j.devcel.2019.07.008.
- 1168 49. De Ceccatty, M.P. (1986). Cytoskeletal organization and tissue patterns of epithelia in
1169 the sponge *Ephydatia mulleri*. *J Morphol* 189, 45-65. 10.1002/jmor.1051890105.
- 1170 50. Kroeger, B., Manning, S.A., Fonseka, Y., Oorschot, V., Crawford, S.A., Ramm, G., and
1171 Harvey, K.F. (2024). Basal spot junctions of *Drosophila* epithelial tissues respond to
1172 morphogenetic forces and regulate Hippo signaling. *Dev Cell* 59, 262-279 e266.
1173 10.1016/j.devcel.2023.11.024.
- 1174 51. Efimova, N., and Svitkina, T.M. (2018). Branched actin networks push against each
1175 other at adherens junctions to maintain cell-cell adhesion. *J Cell Biol* 217, 1827-1845.
1176 10.1083/jcb.201708103.
- 1177 52. Pasupalak, A., Yan-Wei, L., Ni, R., and Pica Ciamarra, M. (2020). Hexatic phase in a
1178 model of active biological tissues. *Soft Matter* 16, 3914-3920. 10.1039/d0sm00109k.
- 1179 53. Snippert, H.J., van der Flier, L.G., Sato, T., van Es, J.H., van den Born, M., Kroon-
1180 Veenboer, C., Barker, N., Klein, A.M., van Rheenen, J., Simons, B.D., and Clevers, H.
1181 (2010). Intestinal crypt homeostasis results from neutral competition between
1182 symmetrically dividing Lgr5 stem cells. *Cell* 143, 134-144. 10.1016/j.cell.2010.09.016.

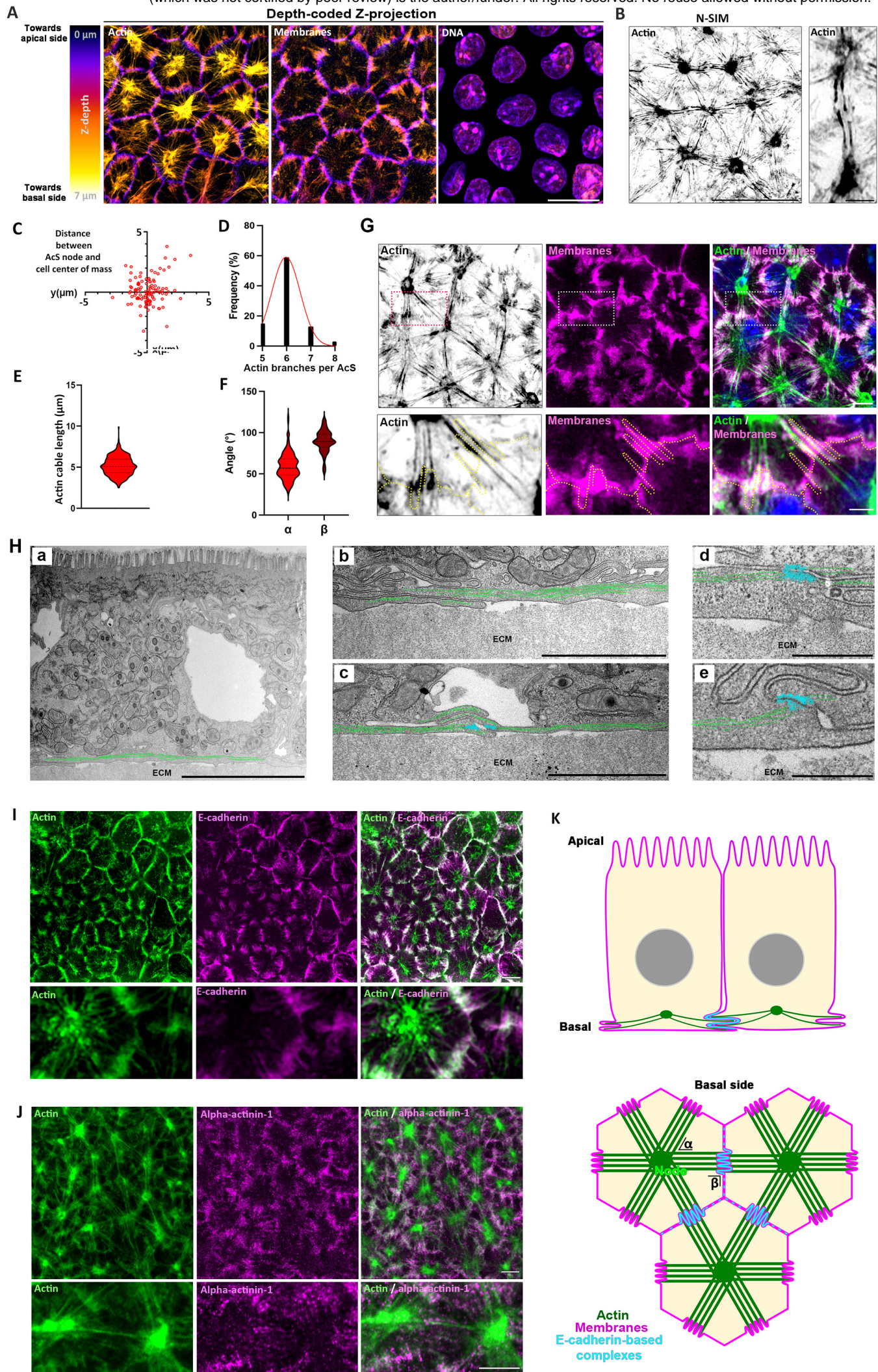
- 1183 54. Krndjija, D., El Marjou, F., Guirao, B., Richon, S., Leroy, O., Bellaiche, Y., Hannezo, E.,
1184 and Matic Vignjevic, D. (2019). Active cell migration is critical for steady-state epithelial
1185 turnover in the gut. *Science* 365, 705-710. 10.1126/science.aau3429.
- 1186 55. Zhang, Y., Conti, M.A., Malide, D., Dong, F., Wang, A., Shmist, Y.A., Liu, C., Zervas,
1187 P., Daniels, M.P., Chan, C.C., et al. (2012). Mouse models of MYH9-related disease:
1188 mutations in nonmuscle myosin II-A. *Blood* 119, 238-250. 10.1182/blood-2011-06-
1189 358853.
- 1190 56. Saleh, J., Fardin, M.A., Barai, A., Soleilhac, M., Frenoy, O., Gaston, C., Cui, H., Dang,
1191 T., Gaudin, N., Vincent, A., et al. (2023). Length limitation of astral microtubules orients
1192 cell divisions in murine intestinal crypts. *Dev Cell* 58, 1519-1533 e1516.
1193 10.1016/j.devcel.2023.06.004.
- 1194 57. Miyoshi, H., and Stappenbeck, T.S. (2013). In vitro expansion and genetic modification
1195 of gastrointestinal stem cells in spheroid culture. *Nat Protoc* 8, 2471-2482.
1196 10.1038/nprot.2013.153.
- 1197 58. Azioune, A., Carpi, N., Tseng, Q., Thery, M., and Piel, M. (2010). Protein
1198 micropatterns: A direct printing protocol using deep UVs. *Methods Cell Biol* 97, 133-
1199 146. 10.1016/S0091-679X(10)97008-8.
- 1200 59. Kepiro, M., Varkuti, B.H., Bodor, A., Hegyi, G., Drahos, L., Kovacs, M., and Malnasi-
1201 Csizmadia, A. (2012). Azidoblebbistatin, a photoreactive myosin inhibitor. *Proc Natl*
1202 *Acad Sci U S A* 109, 9402-9407. 10.1073/pnas.1202786109.
- 1203 60. Pachitariu, M., and Stringer, C. (2022). Cellpose 2.0: how to train your own model. *Nat*
1204 *Methods* 19, 1634-1641. 10.1038/s41592-022-01663-4.
- 1205 61. Schindelin, J., Arganda-Carreras, I., Frise, E., Kaynig, V., Longair, M., Pietzsch, T.,
1206 Preibisch, S., Rueden, C., Saalfeld, S., Schmid, B., et al. (2012). Fiji: an open-source
1207 platform for biological-image analysis. *Nat Methods* 9, 676-682. 10.1038/nmeth.2019.
- 1208 62. Ershov, D., Phan, M.S., Pylvanainen, J.W., Rigaud, S.U., Le Blanc, L., Charles-
1209 Orszag, A., Conway, J.R.W., Laine, R.F., Roy, N.H., Bonazzi, D., et al. (2022).
1210 TrackMate 7: integrating state-of-the-art segmentation algorithms into tracking
1211 pipelines. *Nat Methods* 19, 829-832. 10.1038/s41592-022-01507-1.
- 1212 63. Schmidt U, W.M., Broaddus C and Myers G (2018). Cell detection with star-convex
1213 polygons. *Medical image computing and computer assisted intervention*, 265-273.
1214 doi.org/10.1007/978-3-030-00934-2_30.
- 1215 64. H, N.T.a.H. (2001). A dynamic cell model for the formation of epithelial tissues.
1216 *Philosophical magazine B* 81, 699-719.
- 1217 65. Farhadifar, R., Roper, J.C., Aigouy, B., Eaton, S., and Julicher, F. (2007). The influence
1218 of cell mechanics, cell-cell interactions, and proliferation on epithelial packing. *Curr*
1219 *Biol* 17, 2095-2104. 10.1016/j.cub.2007.11.049.
- 1220 66. Alt, S., Ganguly, P., and Salbreux, G. (2017). Vertex models: from cell mechanics to
1221 tissue morphogenesis. *Philos Trans R Soc Lond B Biol Sci* 372.
1222 10.1098/rstb.2015.0520.
- 1223 67. Bi D, L.J., Schwarz JM and Manning ML (2015). A density-independent rigidity
1224 transition in biological tissues. *Nature Physics* 11, 1074-1074.
- 1225 68. Fletcher, A.G., Osterfield, M., Baker, R.E., and Shvartsman, S.Y. (2014). Vertex
1226 models of epithelial morphogenesis. *Biophys J* 106, 2291-2304.
1227 10.1016/j.bpj.2013.11.4498.
- 1228 69. Lin, S.Z., Ye, S., Xu, G.K., Li, B., and Feng, X.Q. (2018). Dynamic Migration Modes of
1229 Collective Cells. *Biophys J* 115, 1826-1835. 10.1016/j.bpj.2018.09.010.
- 1230 70. Lin, S.Z., Merkel, M., and Rupprecht, J.F. (2023). Structure and Rheology in Vertex
1231 Models under Cell-Shape-Dependent Active Stresses. *Phys Rev Lett* 130, 058202.
1232 10.1103/PhysRevLett.130.058202.
- 1233

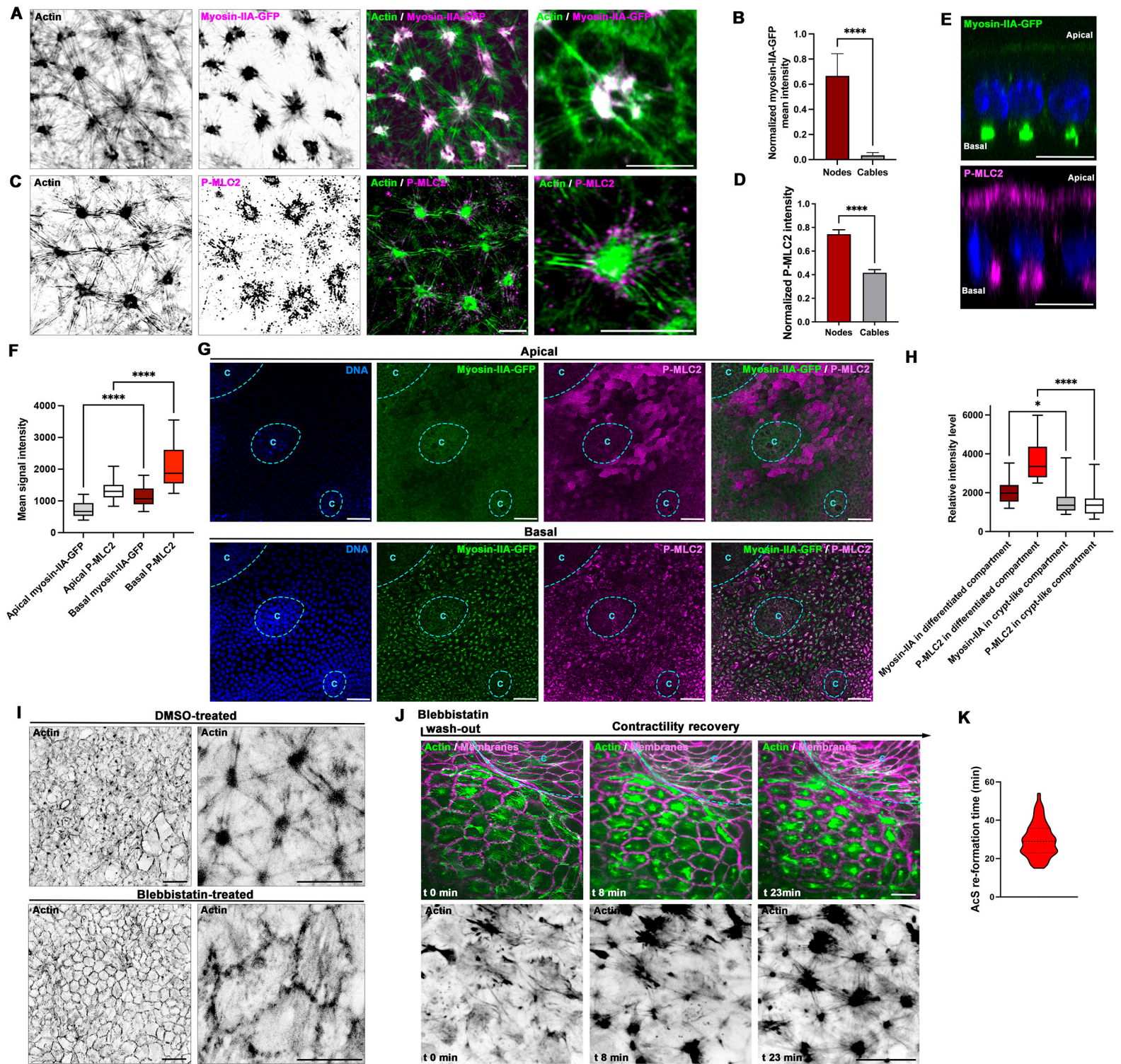
Mouse small intestine



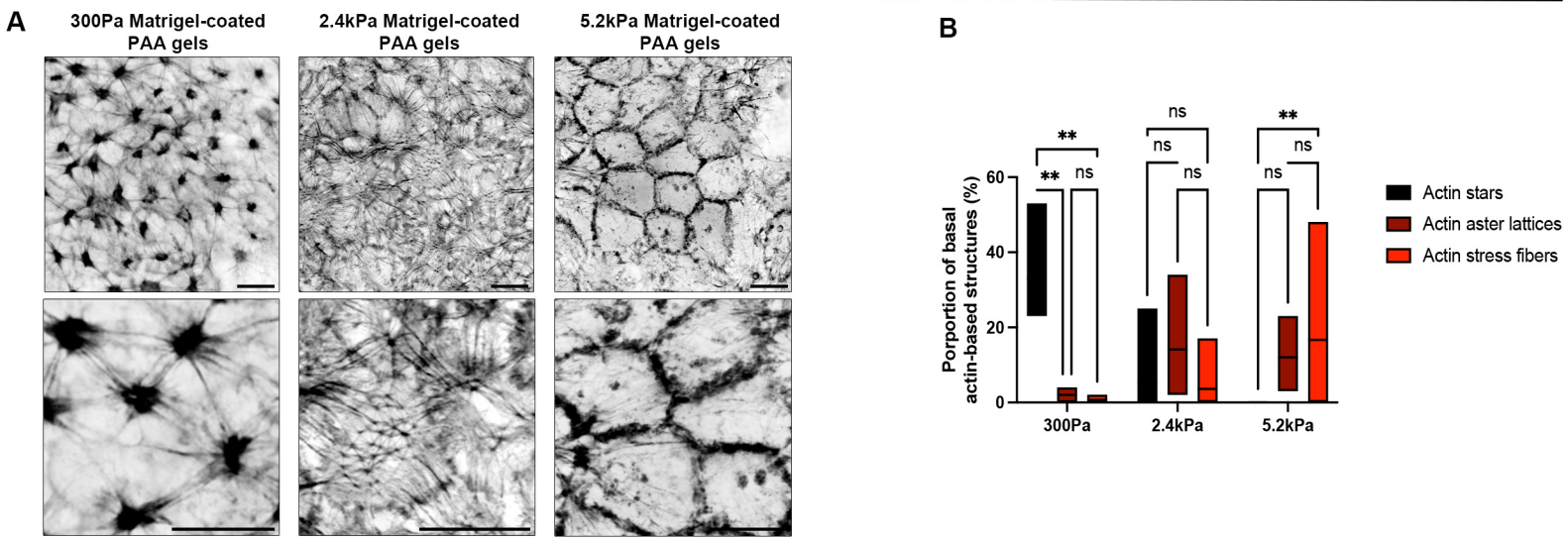
Organoid-derived monolayer



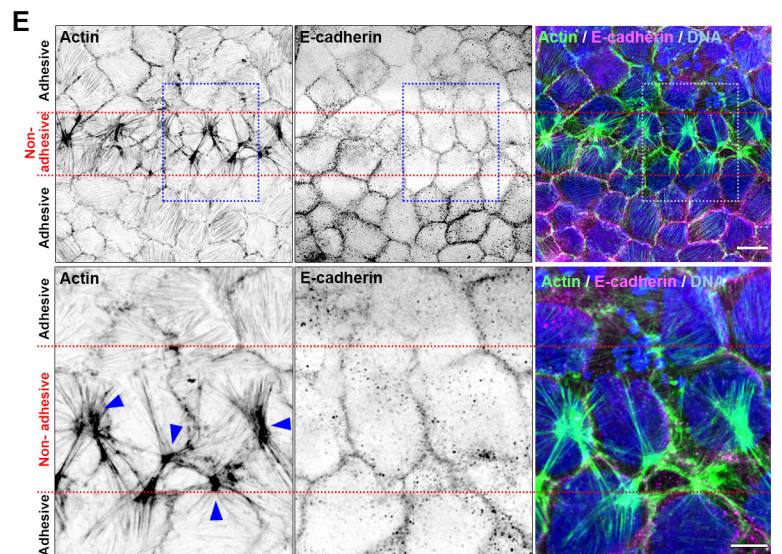
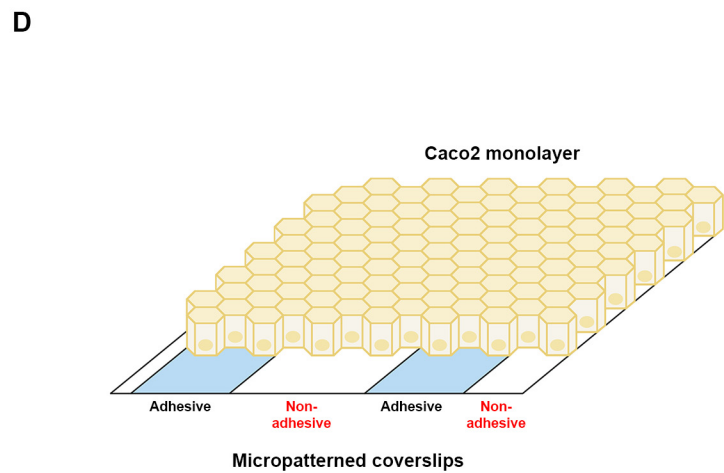
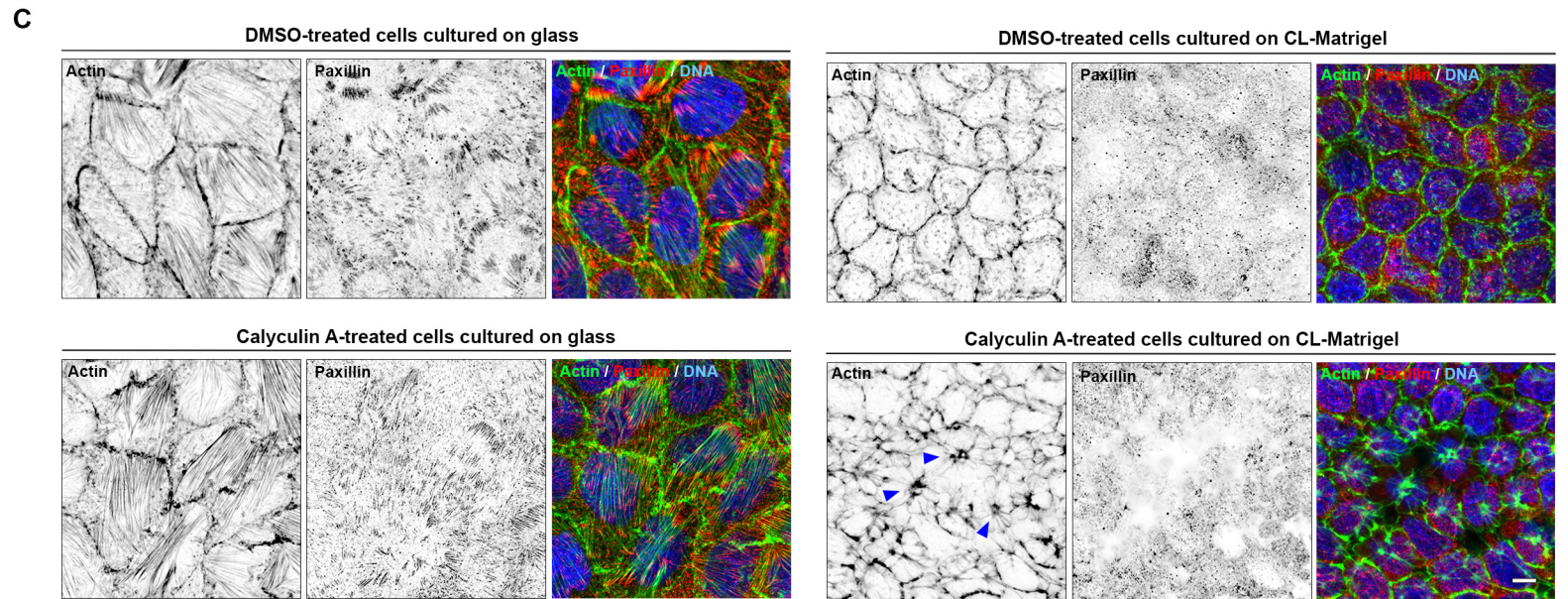


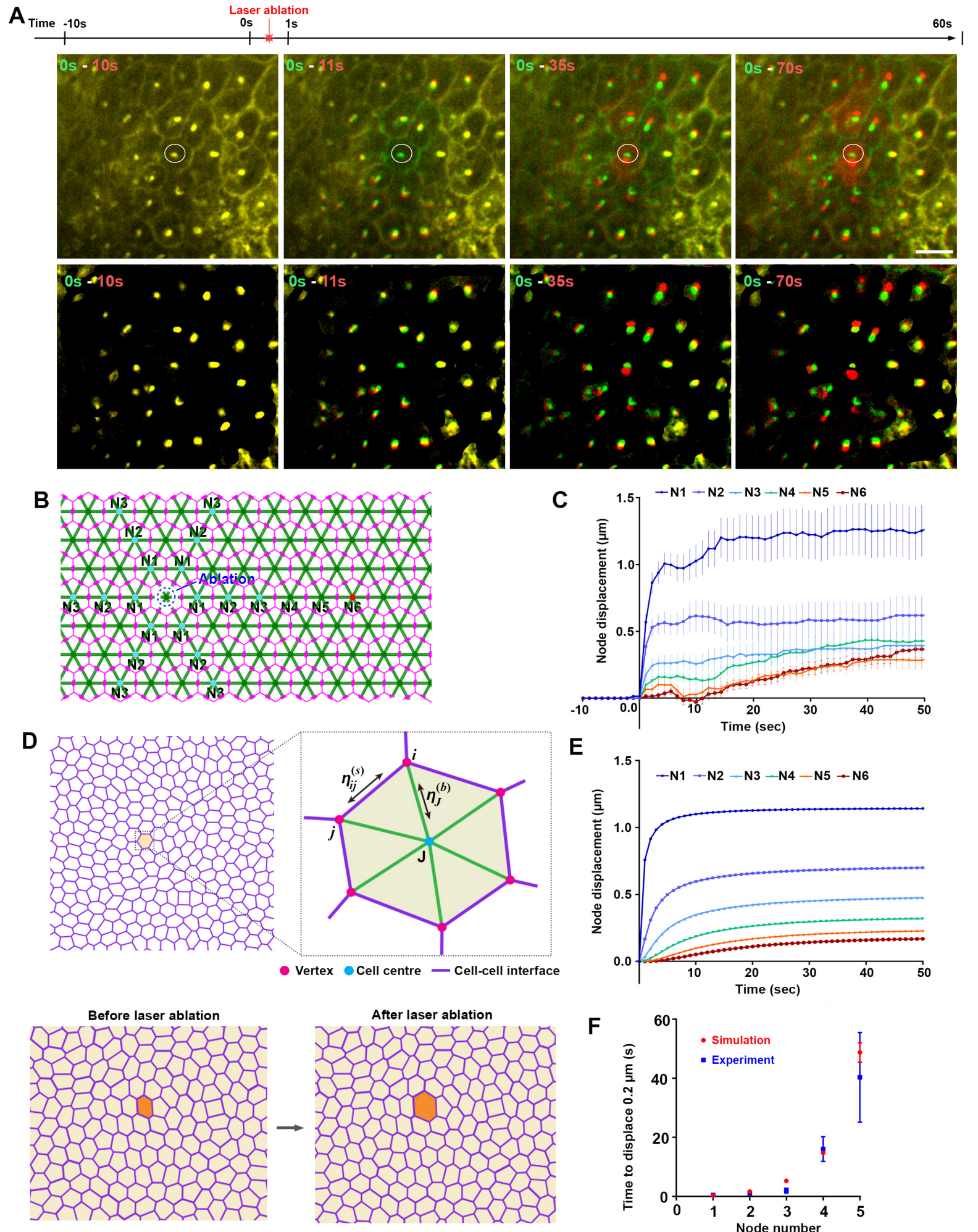


Organoid-derived monolayers

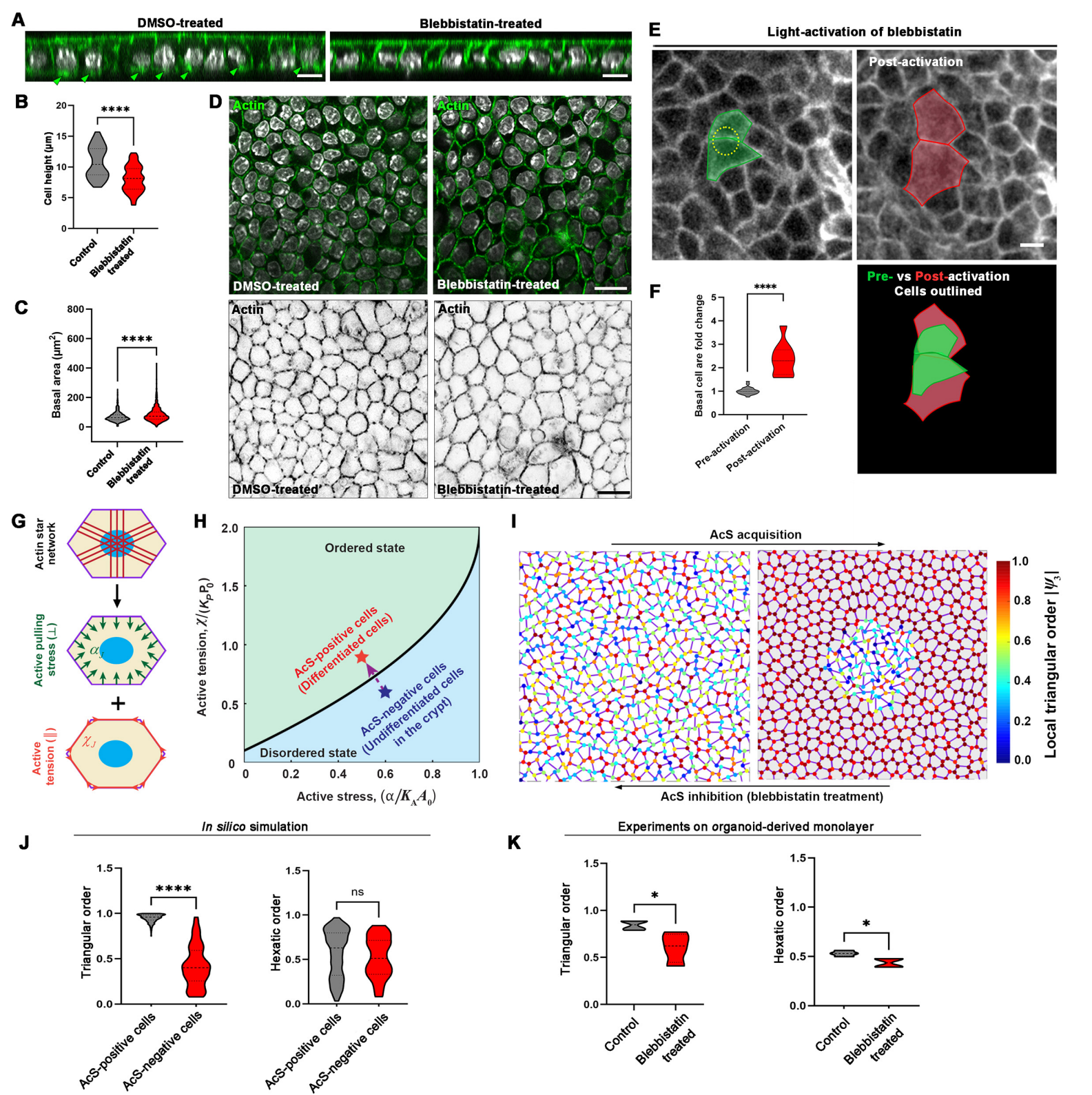


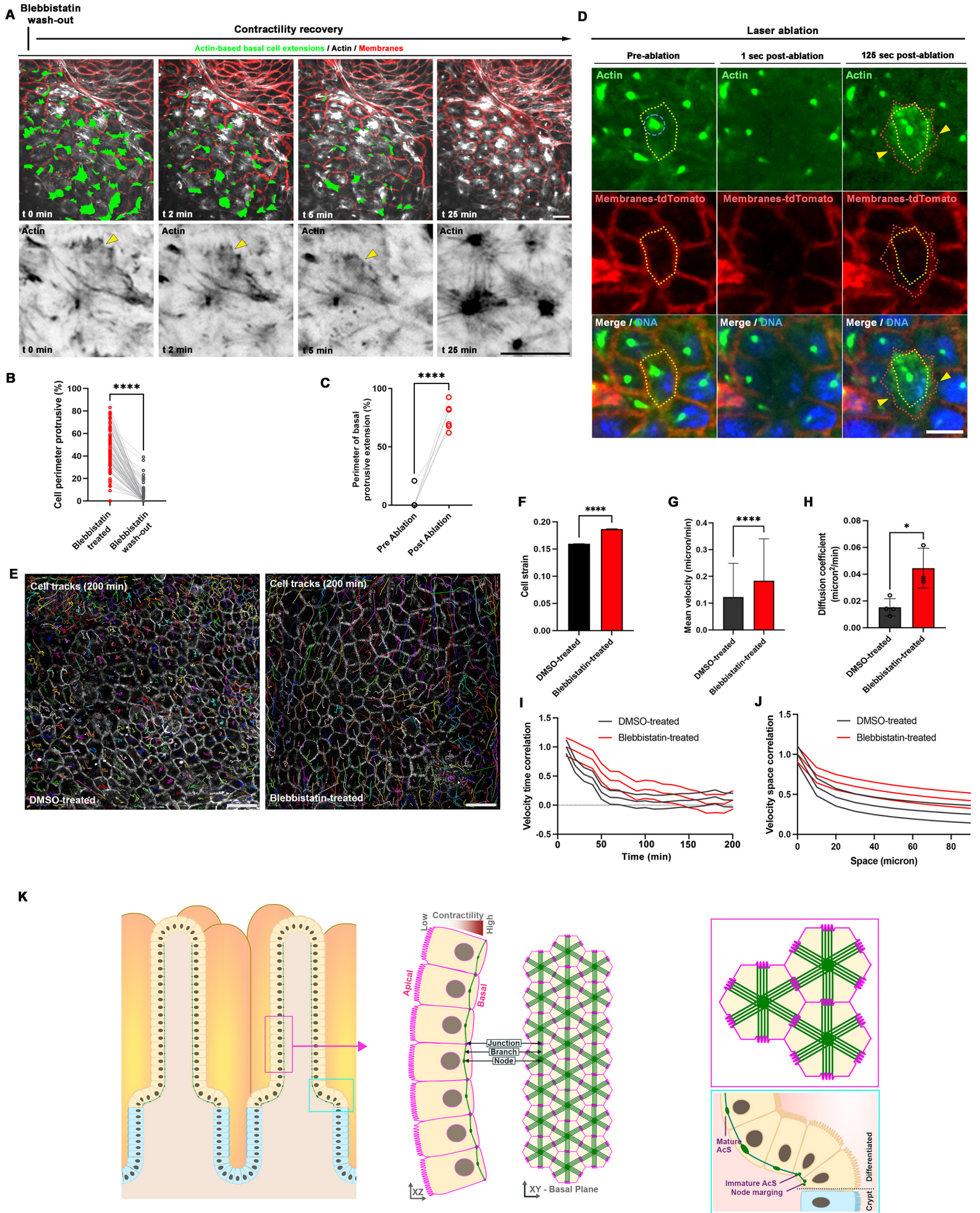
Caco-2 cells





Barai et al. Figure 6





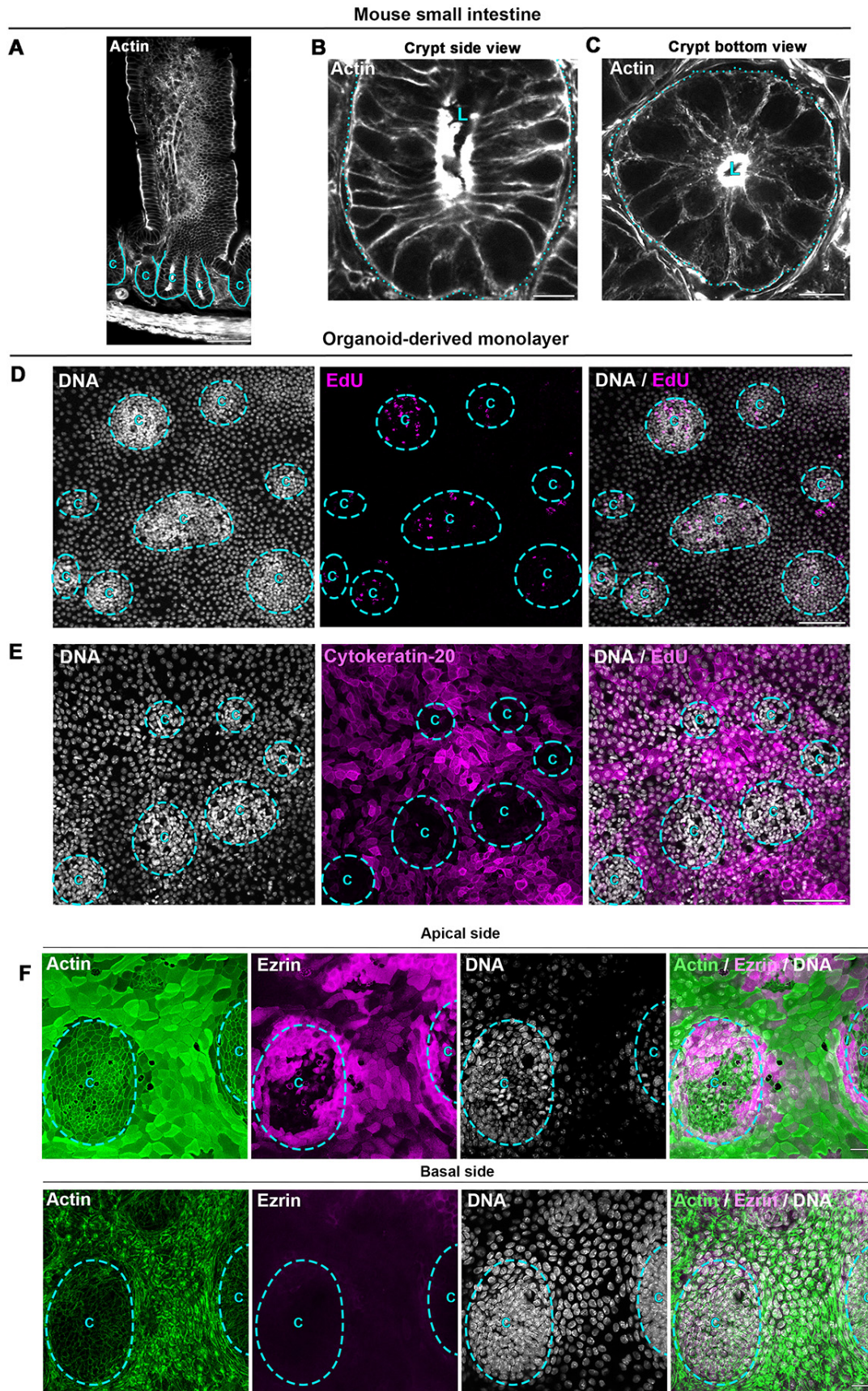
Barai et al.

SUPPLEMENTARY INFORMATION FILE

Supplementary Figures S1- S4

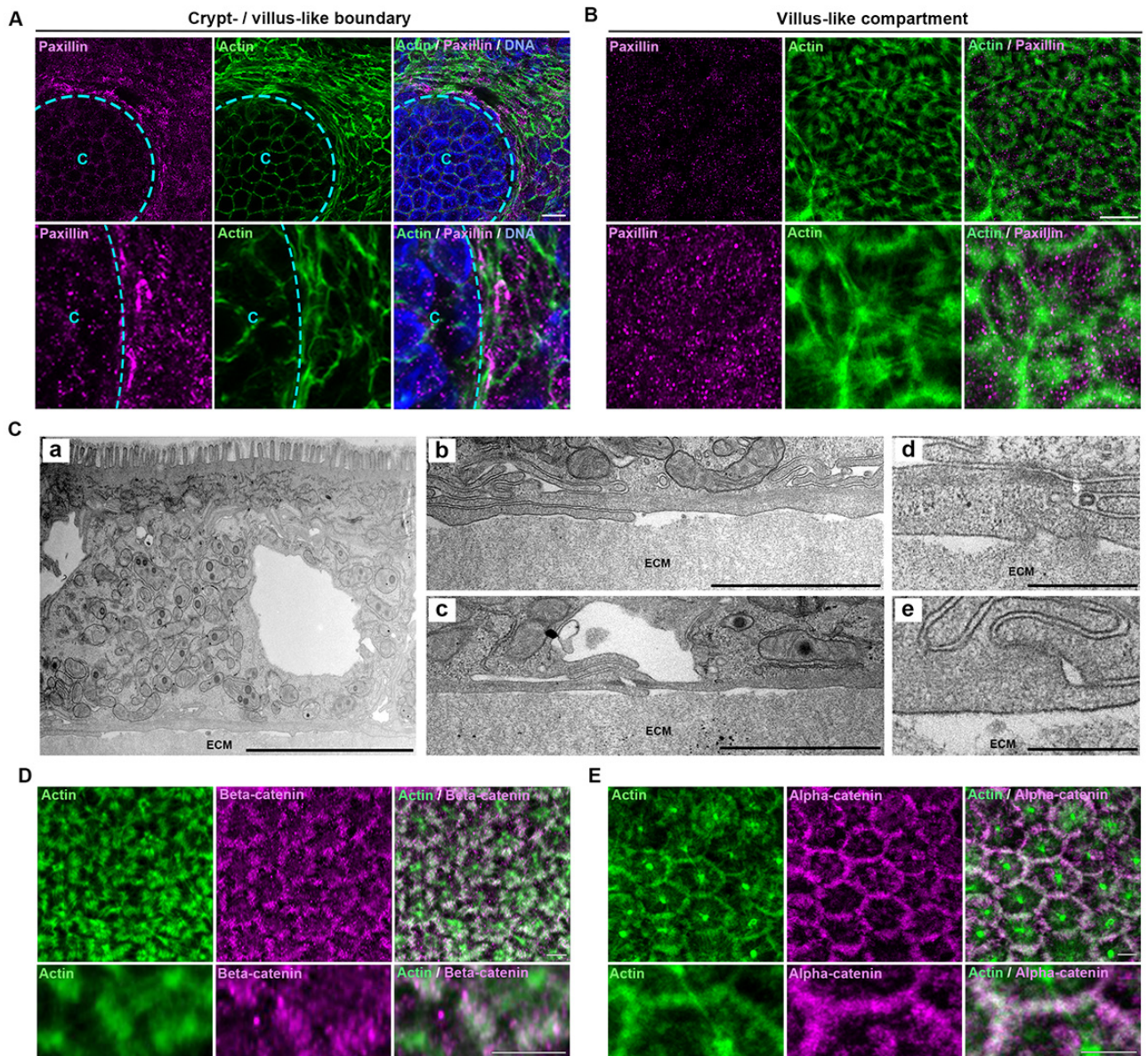
Supplementary Information: File detailing the vertex model simulation procedure are in the online version of the paper.

SUPPLEMENTARY FIGURES



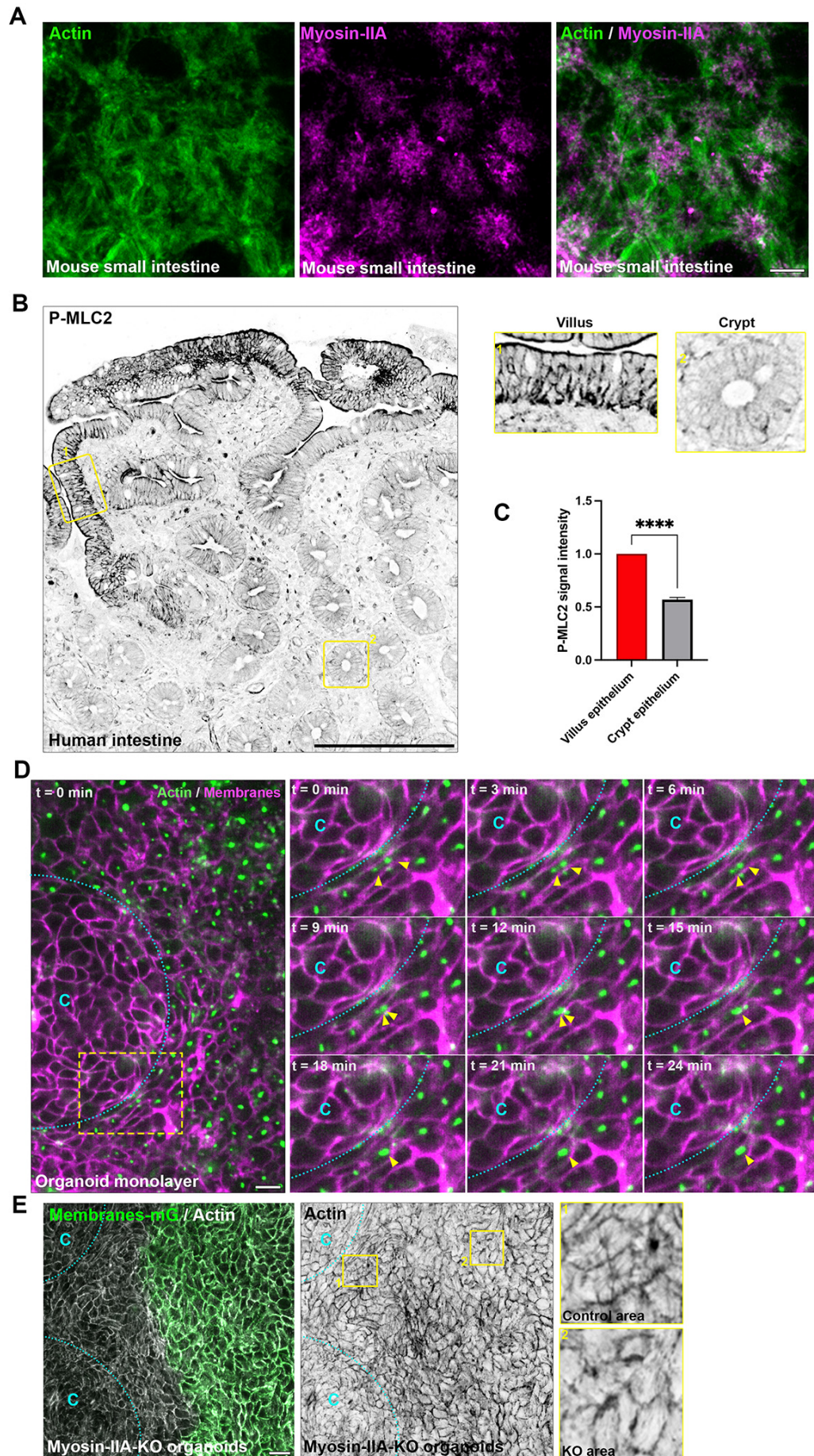
Barai et al., Supplementary Figure 1

Supplementary Figure 1: (A-C) Confocal analysis of actin distribution in the mouse crypt compartment. Crypt side view (B) and bottom view (C) are shown. Crypt domains are delimited with blue line. L, crypt lumen. Scale bar A 100 μm , B-C 10 μm . **(D-E)** Confocal analysis of EdU (D) and cytokeratin-20 (E) distribution in organoid-derived monolayers. Nuclei are shown in gray. Crypt-like domains are delimited in blue. C, crypt-like domain. Scale bar (D), 20 μm , (E) 30 μm . Scale bar, 100 μm . **(F)** Confocal analysis of actin (green), ezrin (magenta) and DNA (gray) in the apical or basal side of organoid-derived monolayers. Crypt-like domains are delimited in blue. C, crypt-like domain. Scale bar, 20 μm .



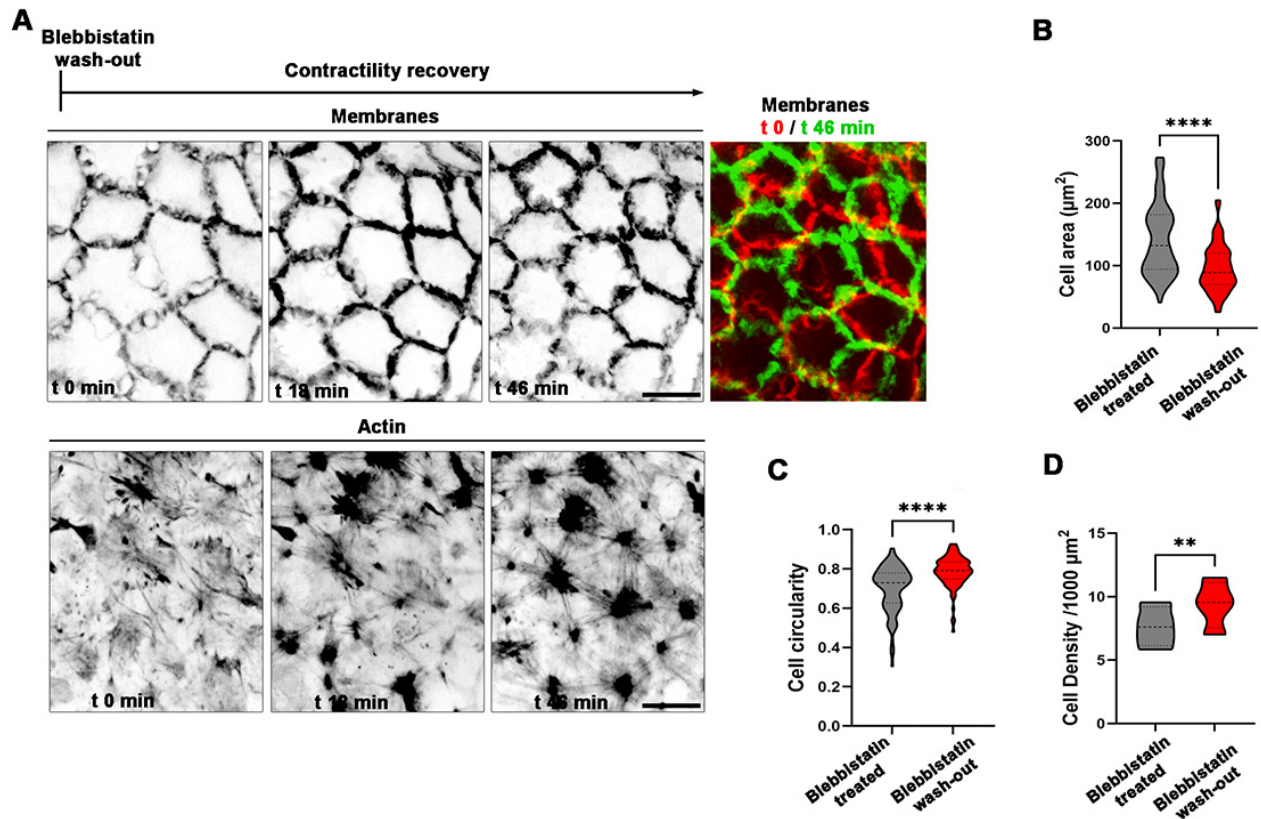
Barai et al., Supplementary Figure 2

Supplementary Figure 2: (A-B) Airy scan confocal analysis of paxillin (magenta) and actin (green) in the area of crypt- / villus-like boundary or in the differentiated compartment. Crypt-like domains are delimited in blue. C, crypt-like domain. Scale bar, 10 μ m. **(Ca-e)** Transmission electron microscopy analysis of the basal domain of differentiated cells in organoid-derived monolayers. ECM, extracellular matrix. Scale bars, (a) 5 μ m, (b-c) 2 μ m, (d-e) 0.5 μ m. **(D-E)** Confocal analysis of β -catenin (magenta) or α -catenin (magenta) and actin (green) in the differentiated compartment of organoid-derived monolayers. Scale bar, 5 μ m.



Barai et al., Supplementary Figure 3

Supplementary Figure 3: **(A)** Confocal analysis of actin (green) and myosin-IIA (magenta) in the basal domain of differentiated cells along the villus of the mouse small intestine. Scale bar, 5 μm . **(B)** Confocal analysis of P-MLC2 distribution in the human intestinal tissue. Areas boxed in yellow are presented on the right. Scale bar, 200 μm . **(C)** Statistical analyses of the signal intensity of P-MLC2 in the villus epithelium and the crypt epithelium in the human small intestine. Mean normalized signal intensity in the villus epithelium = 1, in the crypt epithelium = 0.5691 ± 0.021 . N (intestinal biopsies) = 3. Unpaired t-test, **** $p < 0.0001$. **(D)** Time-lapse analysis of AcS formation at exit of the crypt-like domain in organoid-derived monolayers. Actin (green) and membranes (red) are shown. Yellow arrowheads point toward one AcS formation. Crypt-like domains are delimited in blue. C, crypt. Scale bar, 10 μm . **(E)** Confocal analysis of actin distribution in mosaic myosin-IIA-KO organoid-derived monolayers. Myosin-IIA-KO-induced cells are positive for membranes-mG (green). Crypt-like domains are delimited in blue. C, crypt. Areas boxed in yellow are presented on the right. Scale bar, 20 μm .



Barai et al., Supplementary Figure 4

Supplementary Figure 4: (A) Time-lapse of CellMaskActin and membranes-tdTomato organoid-derived monolayer after 1h blebbistatin treatment and then wash-out (t = 0min). Color-coded t-projection of time-lapse series of membranes-tdTomato signal at the basal domain during contractility recovery in organoid-derived monolayer is shown (t=0min in green, t = 46 min in red). Scale bar, 10 μm. (B) Statistical analysis of basal cell area before and after blebbistatin wash-out. Mean basal area before = 141.75 ± 5.67 (mean \pm S.E.M), after = 95.67 ± 3.69 . N = 4 experiments, n = 100 cells. Paired t-test, ****p < 0.0001. (C) Statistical analysis of basal cell circularity before and after blebbistatin wash-out. Mean basal circularity before = 0.70 ± 0.01 (mean \pm S.E.M), after = 0.79 ± 0.01 . n = 100 cells. Paired t-test, ****p < 0.0001. (D) Statistical analysis of cell density before and after blebbistatin wash-out. Mean cell density before = 7.65 ± 0.79 (mean \pm S.E.M), after = 9.40 ± 0.93 . Paired t-test, **p = 0.004.

Supplementary Information

A multicellular actin star network underpins epithelial organization and connectivity

Barai et al.

In these notes, we present additional details about our numerical vertex model implementation.

Contents

I.	Model 1: AcS formation modelled through a modulation of the bulk active stress	1
	A. Computational model	1
	B. Theoretical analysis: active-stress driven liquid-to-solid phase transition	3
	C. Numerical simulations	5
	1. Simulation 1: laser ablation of an actin star node	5
	2. Simulation 2: blebbistatin treatment (contractility inhibition) and wash-out (contractility recovery)	5
	3. Simulation 3: cell differentiation from crypt cells	6
II.	Model 2: AcS formation modelled through actin cable restoring forces	7
	References	17

I. MODEL 1: ACS FORMATION MODELLED THROUGH A MODULATION OF THE BULK ACTIVE STRESS

A. Computational model

Dynamical equation We consider a vertex model implementation [1-3], with the following dynamics for each vertex,

$$\underbrace{\mathbf{F}_i^{(\text{friction})}}_{\text{Friction}} + \underbrace{\mathbf{F}_i^{(\text{viscous})}}_{\text{Cell viscosity}} + \underbrace{\mathbf{F}_i^{(\text{elastic})}}_{\text{Cell elasticity}} + \underbrace{\mathbf{F}_i^{(\text{active})}}_{\text{Actin star network contractility}} = \mathbf{0}, \quad (\text{S1})$$

where we consider:

1. $\mathbf{F}_i^{(\text{friction})} = -\xi \mathbf{v}_i$ is the friction force between the monolayer and the substrate, ξ being called the friction coefficient and $\mathbf{v}_i = d\mathbf{r}_i/dt$ being the velocity of the vertex i .
2. $\mathbf{F}_i^{(\text{viscous})}$ encompasses both dissipation at the cell-cell interfaces (viscous modulus $\eta_{ij}^{(s)}$) and within the cell bulk (viscous modulus $\eta_J^{(b)}$). We consider:

$$\mathbf{F}_i^{(\text{viscous})} = \sum_{j \in V_i} (\eta_{ij}^{(s)} \mathbf{t}_{i,j} \cdot (\mathbf{v}_j - \mathbf{v}_i)) \mathbf{t}_{i,j} + \sum_{J \in C_i} (\eta_J^{(b)} \mathbf{t}_{i,J} \cdot (\mathbf{v}_J - \mathbf{v}_i)) \mathbf{t}_{i,J}, \quad (\text{S2})$$

where $\mathbf{t}_{i,\alpha} = (\mathbf{r}_\alpha - \mathbf{r}_i) / |\mathbf{r}_i - \mathbf{r}_\alpha|$ is a unit vector from the vertex i to, either a neighbouring vertex ($\alpha = j$), or to the cell geometric centre ($\alpha = J$) with coordinates

$$\mathbf{r}_J = \frac{1}{n_J} \sum_{j \in \text{cell}} \mathbf{r}_j, \quad (\text{S3})$$

where n_J the number of vertices of J -th cell. We refer to ref. [4] for more details on the numerical implementation. In this study, we focus on the case of a uniform viscosity $\eta_{ij}^{(s)} = \eta_J^{(b)} = \eta$.

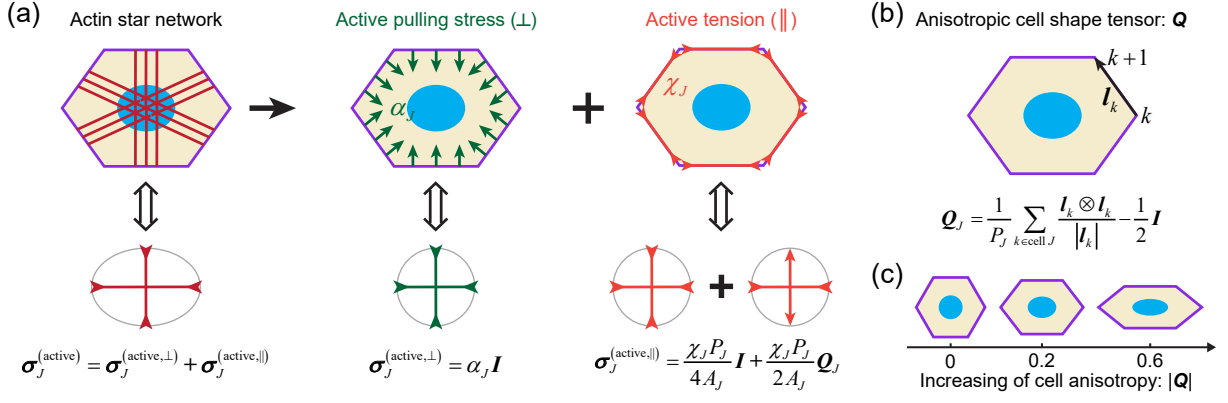


Figure S1: Mechanical characterization of the contractility of the actin star network with a cell by an active pulling stress and an active tension. (a) Mechanical description of the actin star network contractility within a cell by active stresses, $\sigma^{(\text{active})} = \sigma^{(\text{active}, \perp)} + \sigma^{(\text{active}, \parallel)}$ with $\sigma^{(\text{active}, \perp)} = \alpha_J \mathbf{I}$ quantifying the pulling force normal to cell edges and $\sigma^{(\text{active}, \parallel)} = \chi_J P_J / (4A_J) \mathbf{I} + \chi_J P_J / (2A_J) \mathbf{Q}_J$ quantifying an active tension parallel to cell edges. (b) Sketch of the anisotropic cell shape tensor \mathbf{Q} . (c) Examples of cell shapes as a function of the magnitude of the cell anisotropic tensor $|\mathbf{Q}|$.

3. $\mathbf{F}_i^{(\text{elastic})}$ is the elastic force stemming from the variation of the cell shape, which can be expressed by, $\mathbf{F}_i^{(\text{elastic})} = -\partial E / \partial \mathbf{r}_i$ with the mechanical energy [2, 5–8]:

$$E = \underbrace{\sum_{J=1}^N \frac{1}{2} K_A (A_J - A_0)^2}_{\text{Cell area elasticity}} + \underbrace{\sum_{J=1}^N \frac{1}{2} K_P (P_J - P_0)^2}_{\text{Cell perimeter elasticity}}, \quad (\text{S4})$$

where K_A and K_P are the rigidities associated with cell area and cell perimeter; A_0 and P_0 are the preferred cell area and the preferred cell perimeter, respectively; A_J and P_J are the actual area and perimeter of the J -th cell, respectively.

4. the active force $\mathbf{F}_i^{(\text{active})}$ corresponds to the contribution of the multicellular actin; we decompose the actin star network into two contributions, resulting from:

- (4.1) an active pulling stress $\sigma_J^{(\text{active}, \perp)} = \alpha_J \mathbf{I}$ with $\alpha_J \geq 0$ quantifies the intensity of the active pulling stress induced by the contractility of the actin star network within the J -th cell, which describes the active pulling force normal to cell edges, see Fig. S1(a);
- (4.2) an active tension $\chi_J > 0$ parallel to edges of the J -th cell, see Fig. S1(a), which results in the following $\mathbf{F}_k^{(\text{AT})}$ force applied on the k -th vertex of the J -th cell:

$$\mathbf{F}_k^{(\text{AT})} = \frac{1}{2} \chi_J \frac{\mathbf{l}_k}{|\mathbf{l}_k|} - \frac{1}{2} \chi_J \frac{\mathbf{l}_{k-1}}{|\mathbf{l}_{k-1}|}, \quad (\text{S5})$$

where $\mathbf{l}_k = \mathbf{r}_{k+1} - \mathbf{r}_k$ the k -th edge vector of the J -th cell.

B. Theoretical analysis: active-stress driven liquid-to-solid phase transition

In this section, we show that the active pulling stress α_J is equivalent to renormalizing the preferred area of the J -th cell as: $A_{0,J} = A_0 - \alpha_J/K_A$; and that the active tension χ_J is equivalent to renormalizing the preferred perimeter of the J -th cell as: $P_{0,J} = P_0 - \chi_J/(2K_P)$. Our derivation is based on the analytical derivation of the total stresses within cells.

We express the active stress induced by the actin star network by (Fig. S1(a)):

$$\boldsymbol{\sigma}_J^{(\text{active})} = \boldsymbol{\sigma}_J^{(\text{active},\perp)} + \boldsymbol{\sigma}_J^{(\text{active},\parallel)}, \quad (\text{S6})$$

where

$$\boldsymbol{\sigma}_J^{(\text{active},\perp)} = \alpha_J \mathbf{I}, \quad (\text{S7})$$

quantifies the active stress induced by the active pulling stress (i.e., pulling forces normal to the cell edges, Fig. S1(a)), and, using the Batchelor formula [8–11],

$$\boldsymbol{\sigma}_J^{(\text{active},\parallel)} = -\frac{1}{A_J} \sum_{k \in \text{cell } J} \mathbf{r}_k \otimes \mathbf{F}_k^{(\text{AT})}, \quad (\text{S8})$$

quantifies the active stress induced by the active tension parallel to cell edges (Fig. S1(a)). Substituting Eq. (S5) into Eq. (S8), we obtain

$$\begin{aligned} \boldsymbol{\sigma}_J^{(\text{active},\parallel)} &= -\frac{1}{A_J} \sum_{k \in \text{cell } J} \mathbf{r}_k \otimes \left(\frac{1}{2} \chi_J \frac{\mathbf{l}_k}{|\mathbf{l}_k|} - \frac{1}{2} \chi_J \frac{\mathbf{l}_{k-1}}{|\mathbf{l}_{k-1}|} \right) = -\frac{\chi_J}{2A_J} \sum_{k \in \text{cell } J} \mathbf{r}_k \otimes \left(\frac{\mathbf{l}_k}{|\mathbf{l}_k|} - \frac{\mathbf{l}_{k-1}}{|\mathbf{l}_{k-1}|} \right) \\ &= -\frac{\chi_J}{2A_J} \sum_{k \in \text{cell } J} \left(\mathbf{r}_k \otimes \frac{\mathbf{l}_k}{|\mathbf{l}_k|} - \mathbf{r}_k \otimes \frac{\mathbf{l}_{k-1}}{|\mathbf{l}_{k-1}|} \right) = -\frac{\chi_J}{2A_J} \sum_{k \in \text{cell } J} \left(\mathbf{r}_k \otimes \frac{\mathbf{l}_k}{|\mathbf{l}_k|} - \mathbf{r}_{k+1} \otimes \frac{\mathbf{l}_k}{|\mathbf{l}_k|} \right) \\ &= \frac{\chi_J}{2A_J} \sum_{k \in \text{cell } J} \frac{\mathbf{l}_k \otimes \mathbf{l}_k}{|\mathbf{l}_k|} = \frac{\chi_J P_J}{2A_J} \left(\mathbf{Q}_J + \frac{1}{2} \mathbf{I} \right) = \frac{\chi_J P_J}{4A_J} \mathbf{I} + \frac{\chi_J P_J}{2A_J} \mathbf{Q}_J, \end{aligned} \quad (\text{S9})$$

where \mathbf{Q}_J is a traceless anisotropic cell shape tensor (Fig. S1(b)), defined as [8, 12]

$$\mathbf{Q}_J = \frac{1}{P_J} \sum_{k \in \text{cell } J} \frac{\boldsymbol{\ell}_k \otimes \boldsymbol{\ell}_k}{|\boldsymbol{\ell}_k|} - \frac{1}{2} \mathbf{I}. \quad (\text{S10})$$

For isotropic cell shape, e.g., regular hexagonal shape, $\mathbf{Q}_J = \mathbf{0}$; the magnitude $|\mathbf{Q}_J|$ quantifies cell anisotropy (Fig. S1(c)). Overall, the active stress induced by the actin star network can be expressed as:

$$\boldsymbol{\sigma}_J^{(\text{active})} = \boldsymbol{\sigma}_J^{(\text{active},\perp)} + \boldsymbol{\sigma}_J^{(\text{active},\parallel)} = \left(\alpha_J + \frac{\chi_J P_J}{4A_J} \right) \mathbf{I} + \frac{\chi_J P_J}{2A_J} \mathbf{Q}_J. \quad (\text{S11})$$

We recall that the elastic stress corresponding to the mechanical energy Eq. (S4) reads [8, 13]:

$$\boldsymbol{\sigma}_J^{(\text{elastic})} = \left[K_A (A_J - A_0) + \frac{1}{2} \frac{K_P P_J (P_J - P_0)}{A_J} \right] \mathbf{I} + \frac{K_P P_J (P_J - P_0)}{A_J} \mathbf{Q}_J. \quad (\text{S12})$$

Therefore, the total stress within the J -th cell reads:

$$\begin{aligned} \boldsymbol{\sigma}_J &= \boldsymbol{\sigma}_J^{(\text{elastic})} + \boldsymbol{\sigma}_J^{(\text{active})} \\ &= \left[K_A (A_J - A_0) + \alpha_J + \frac{1}{2} \frac{K_P P_J (P_J - P_0)}{A_J} + \frac{1}{4} \frac{\chi_J P_J}{A_J} \right] \mathbf{I} + \left[\frac{K_P P_J (P_J - P_0)}{A_J} + \frac{1}{2} \frac{\chi_J P_J}{A_J} \right] \mathbf{Q}_J \\ &= \left[K_A (A_J - A_{0,J}) + \frac{1}{2} \frac{K_P P_J (P_J - P_{0,J})}{A_J} \right] \mathbf{I} + \frac{K_P P_J (P_J - P_{0,J})}{A_J} \mathbf{Q}_J, \end{aligned} \quad (\text{S13})$$

where

$$A_{0,J} = A_0 - \frac{\alpha_J}{K_A}, \quad (\text{S14})$$

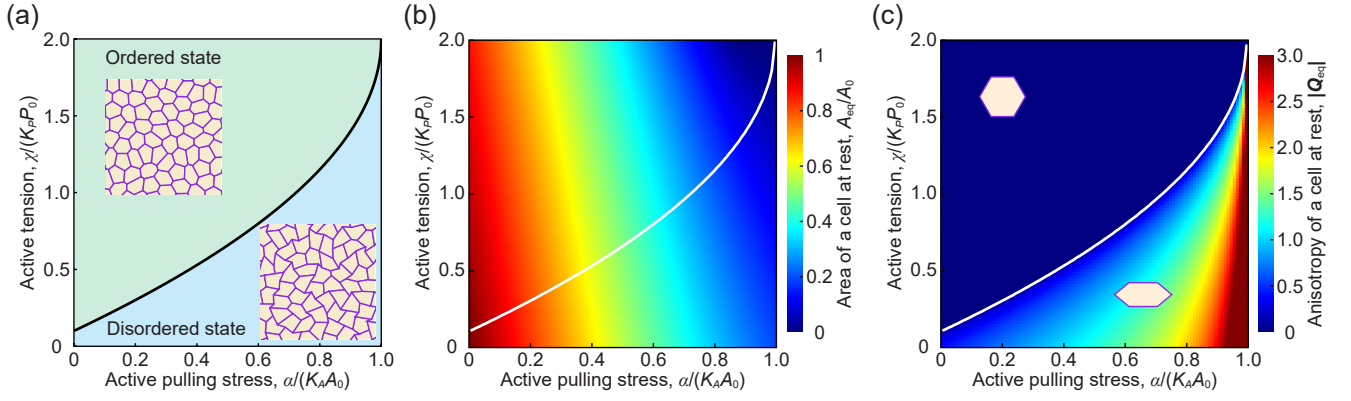


Figure S2: Theoretical analysis of cell area and cell anisotropy dictated by the active pulling stress α and the active tension χ . (a) Critical rigidity transition line Eq. (S19) (solid black line) and typical morphology of a cell monolayer within each phase. (b) The area of a hexagonal cell at rest (white line: rigidity transition line Eq. (S19)) (c) Theoretical prediction [8] of the anisotropy $|\mathbf{Q}|$ of a single cell at rest. (white line: rigidity transition line Eq. (S19)). Parameters: $K_A = 1$, $A_0 = 1$, $K_P = 0.02$, and $P_0 = 4$.

is a rescaled preferred area of the J -th cell, modulated by the isotropic active stress level α_J , and

$$P_{0,J} = P_0 - \frac{\chi_J}{2K_P}, \quad (\text{S15})$$

is a rescaled preferred perimeter of the J -th cell, modulated by the active tension level χ_J .

Effective mechanical energy formalism. The total stress Eq. (S13) corresponds to an effective mechanical energy of the J -th cell,

$$E_J^{(\text{eff})} = \frac{1}{2}K_A(A_J - A_{0,J})^2 + \frac{1}{2}K_P(P_J - P_{0,J})^2, \quad (\text{S16})$$

which satisfies

$$\boldsymbol{\sigma}_J = -\frac{1}{A_J} \sum_{k \in \text{cell } J} \mathbf{r}_k \otimes \left(-\frac{\partial E_J^{(\text{eff})}}{\partial \mathbf{r}_k} \right). \quad (\text{S17})$$

Therefore, the contractility of the actin star network can be mimicked by a renormalized mechanical energy, $E_J^{(\text{eff})}$.

Cellular target shape index modulated by the actin star network. Equations (S14) and (S15) show that the actin star network within cells plays a role in modulating the target shape index of the cell [6],

$$s_{0,J} = \frac{P_{0,J}}{\sqrt{A_{0,J}}} = \frac{P_0}{\sqrt{A_0}} \frac{1 - \frac{\chi_J}{2K_P P_0}}{\sqrt{1 - \frac{\alpha_J}{K_A A_0}}}. \quad (\text{S18})$$

An increase in the active pulling stress α_J leads to an increase in the target shape index $s_{0,J}$, making cells more elongated; while an increase in the active tension χ_J leads to a decrease in the target shape index $s_{0,J}$, making cells more rounded.

Following [6], letting $s_{0,J} = s_0^*$ leads to a critical line of rigidity transition in the (α_J, χ_J) space:

$$\chi_J^* = 2K_P P_0 \left(1 - s_0^* \frac{\sqrt{A_0}}{P_0} \sqrt{1 - \frac{\alpha_J}{K_A A_0}} \right), \quad (\text{S19})$$

where s_0^* is a critical target shape index beyond which the cell monolayer behaves as a disordered liquid; $s_0^* \approx 3.81$ for disordered cellular system [6]. When the active tension is strong enough, i.e., $\chi_J > \chi_J^*$, the cell monolayer behaves as a liquid, exhibiting a disordered and elongated cell shape pattern, see Fig. S2.

C. Numerical simulations

We perform numerical simulations to explore the roles of the multicellular actin star network in the context of

1. the laser ablation of an actin star node,
2. the blebbistatin treatment and wash-out experiment,
3. the progressive cell differentiation.

In all these simulations, we simulated a cell monolayer consisting of $N = 400$ cells in a square box of size $L = \sqrt{NA_0}$, using periodic boundary conditions, see Fig. S4(a). We initialize our simulations from a random Voronoi cell pattern and let the system relax toward an equilibrium state, using the procedure as described in our previous study [8]. We then (i) solve the force balance equation to obtain the motion velocity of each vertex $\{\mathbf{v}_i\}$; (ii) move the vertices to new positions using a forward Euler scheme,

$$\mathbf{r}_i(t + \Delta t) = \mathbf{r}_i + \mathbf{v}_i \Delta t, \quad (\text{S20})$$

and (iii) perform T1 topological transitions for all short cell-cell junctions ($l_{ij} < \ell_{T1} = 0.01\sqrt{A_0}$).

1. Simulation 1: laser ablation of an actin star node

Method In such simulations, the activities of all cells are set to be the same before the laser ablation, $\alpha_J = \alpha^{(\text{control})} > 0$ and $\chi_J = \chi^{(\text{control})}$ for $J = 1, 2, 3, \dots, N$. To model the effect of the laser ablation, we select a cell at the center of the simulation box and set its activity to be zero $\alpha_J = \alpha^{(\text{ablation})} = 0$ and $\chi_J = \chi^{(\text{ablation})} = 0$, see Fig. S4(a). We then let the system relax to a new equilibrium state. We track and measure the displacement of each cell during such a relaxation process. We provide the parameter values in simulations in Table I.

Result We find that the delay in the strain propagation scales with the distance to the ablated cell according to $\tau \sim L^2/K$, i.e. with an effective diffusion of elasticity, denoted K , which is inversely proportional to the friction, i.e. $K \propto 1/\xi$ (see Fig. S4(e)). In the presence of a finite friction, the evolution of the strain is only marginally dependent on the cell-cell viscosity value, see Fig. S4(d). In the limit of vanishing friction ($\xi \rightarrow 0$), the strain is propagated at large distances ($N = 8$) in less than a second (blue curve in Fig. S4(e)).

Discussion Diffusion of elasticity is also observed in an optical tweezer mechanical perturbation of cell membranes in the *Drosophila* embryo [14]. There, the time delay in the strain is measured at $\tau_1 = 150 \pm 85$ ms at a one-cell distance ($\sim 7\mu\text{m}$) to the mechanical perturbation site. Such value lies within the time resolution of our experiments. Based on the diffusion of elasticity scaling, we expect that the corresponding value at the ten-cell distance should scale as $\tau_{10} = 100\tau_1$, corresponding to $\tau_8 \approx 15 \pm 8$ s. Such an estimate is compatible with the value at the ten-cell distance measured in one of our experiments, called experiment 1, see Fig. XX; in most other experiments of laser dissection, however, the time delay in the strain remains lower than a few seconds, suggesting a significantly reduced friction as compared to the experiment 1, as depicted in Fig. S4(e). Overall, the observation that the strain propagation is very rapid is compatible with a very low friction to the substrate.

2. Simulation 2: blebbistatin treatment (contractility inhibition) and wash-out (contractility recovery)

Method Here, the activities of all cells are set to be the same before the blebbistatin treatment, $\alpha_J = \alpha^{(\text{control})} > 0$ and $\chi_J = \chi^{(\text{control})} > 0$ for $J = 1, 2, 3, \dots, N$. To model the effect of the blebbistatin treatment, we select a group of cells with a number $N_{\text{blebbistatin}} = 50$ at the center region of the simulation box and set their activities to zero $\alpha_J = \alpha^{(\text{blebbistatin})} = 0 < \alpha^{(\text{control})}$ and $\chi_J = \chi^{(\text{blebbistatin})} = 0 < \chi^{(\text{control})}$ for cells being treated with blebbistatin, see Fig. S5(a). We then let the system relax to a new equilibrium state. Subsequently, to model the effect of blebbistatin wash-out, we recover the activity level of these cells being treated with blebbistatin. We provide the parameter values in simulations in Table II.

Result With our set of parameter values, the cell area and cell anisotropy are both increased in the blebbistatin-treated cells; the cell area increase is chosen to match the values observed in experiments (Fig. SX). In the blebbistatin wash-out experiment, the recovery of the actin star network leads to a progressive return of the cell area to the pre-blebbistatin treatment value (Fig. 5D). This experiment is important in setting the values of α and χ associated to the onset of the actin star network.

3. Simulation 3: cell differentiation from crypt cells

Method Here, to mimic the process of cell differentiation, the activities of all cells are set to be the same before differentiation, $\alpha_J = \alpha^{(\text{undifferentiated})}$ and $\chi_J = \chi^{(\text{undifferentiated})}$ for $J = 1, 2, 3, \dots, N$.

We keep constant the (α_J, χ_j) parameters within a group of cells with a number $N_{\text{differentiated}} = 50$ at the center region of the simulation box - to mimic the onset of crypt-like cells domains - while switching the (α_J, χ_j) parameters to $\alpha_J = \alpha^{(\text{differentiated})}$ and $\chi_J = \chi^{(\text{differentiated})}$ within the rest of the tissue, mimicking differentiation into villus-like cells, see Fig. S6(a).

We then let the system relax to a new equilibrium state. We provide the parameter values in simulations in Table III and IV.

Result We test two possible cell differentiation paths in the (α, χ) space, see Fig. S6(b,c).

- in the cell differentiation path I differentiation path, the cells within the interior domain increase their area, akin to cells subjected to the blebbistatin treatment experiments.
- in the cell differentiation path II, the cells within the interior domain display a lower area than differentiated ones, as crypt-like cells. We also observe a progressive increase of the triangular order within the differentiated cells, see Fig. S6(g). As in experiments, the hexatic order, Eq. (??), remained relatively unchanged throughout the cell differentiation process, while the triangular order, Eq. (??), evolved significantly, see Fig. S6(f-g).

II. MODEL 2: ACS FORMATION MODELLED THROUGH ACTIN CABLE RESTORING FORCES

So far, we have considered a generic model in which the active pulling stress α_J and active tension χ_J are two independent parameters.

Here, we propose to focus on a more specific microscopic model which encompasses the observation that the actin star seemingly connects each of the junction mid-points to the cell center, see Fig. S3. We express the relation of this new model to the former one described above in terms of a linear relation between the actin star tension ξ (new model) with the active pressure α_J and active tension χ_J (former model).

New model description Here, we propose to model the actin star network through a set of active forces, denoted \mathbf{T}_i , each applied to the junction mid-points and pointing toward the cell center, $\mathbf{r}_C = \sum_{i \in \text{cell}} \mathbf{r}_i / n$, with n the number of edges of the cell. Based on the Batchelor formula [8–11], the coarse-grained active stress reads

$$\boldsymbol{\sigma}^{(\text{active})} = -\frac{1}{A} \sum_{i \in \text{cell}} \mathbf{s}_i \otimes \mathbf{T}_i. \quad (\text{S21})$$

where $\mathbf{s}_i = \boldsymbol{\rho}_i + \mathbf{l}_i/2 = \mathbf{r}_i - \mathbf{r}_C + (\mathbf{r}_{i+1} - \mathbf{r}_i)/2 = (\mathbf{r}_i + \mathbf{r}_{i+1})/2 - \mathbf{r}_C$ is the length vector \mathbf{s}_i of the i -th actin cable, assumed to connect the cell center to the junction mid-point.

Here, we focus on the case of a linear relationship between the active force \mathbf{T}_i and the i -th actin cable vector \mathbf{s}_i

$$\mathbf{T}_i = -\zeta \mathbf{s}_i, \quad (\text{S22})$$

where $\zeta > 0$ quantifies the contractility of the actin star network. Substituting Eq. (S22) into Eq. (S21), the active stress then takes the expression:

$$\boldsymbol{\sigma}^{(\text{active})} = \zeta \mathbf{W}, \quad (\text{S23})$$

where \mathbf{W} is what we call the mid-point cell shape tensor (Fig. S3), defined as:

$$\mathbf{W} = \frac{1}{A} \sum_{i \in \text{cell}} \mathbf{s}_i \otimes \mathbf{s}_i. \quad (\text{S24})$$

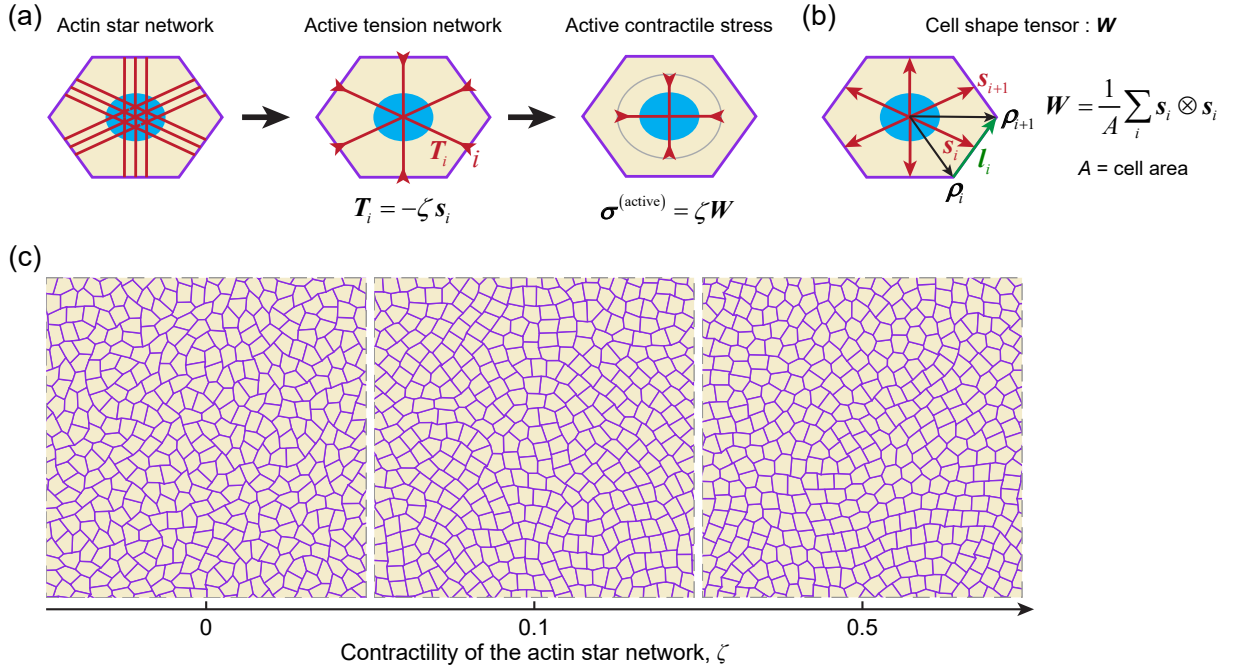


Figure S3: Alternative active stress description of the actin star network. (a, b) Model sketches of the actin star network, active stresses, and cell shape tensor. (a) Mechanical description of the actin star network contractility within a cell by active stresses, $\boldsymbol{\sigma}^{(\text{active})} = \zeta \mathbf{W}$ with $\zeta > 0$ quantifying the contractility level and \mathbf{W} a cell shape tensor. (b) Sketch of the cell shape tensor \mathbf{W} . (c) Numerical simulations using the alternative stress description (Eq. (S23)). An increase in the contractility parameter ζ leads to more rounded cell shapes. Parameters: $K_A = 1$, $A_0 = 1$, $K_P = 0.02$, and $P_0 = 4$.

In particular, for a regular hexagonal cell shape, $\mathbf{W} = (\sqrt{3}/2)\mathbf{I}$.

Let us here consider a regular hexagonal cell undergoing affine transformation, $(x, y) \rightarrow (\lambda_1 x, \lambda_2 y)$, with λ_1 and λ_2 stretches along the x -axis and the y -axis. In this case, the mid-point cell shape tensor \mathbf{W} reads

$$\mathbf{W} = \frac{\sqrt{3}}{2} \frac{\lambda_1}{\lambda_2} \hat{\mathbf{x}} \otimes \hat{\mathbf{x}} + \frac{\sqrt{3}}{2} \frac{\lambda_2}{\lambda_1} \hat{\mathbf{y}} \otimes \hat{\mathbf{y}}, \quad (\text{S25})$$

while the \mathbf{Q} tensor defined in Eq. (S10) reads:

$$\mathbf{Q} = \left(\frac{\lambda_1}{\sqrt{\lambda_1^2 + 3\lambda_2^2}} - \frac{1}{2} \right) \hat{\mathbf{x}} \otimes \hat{\mathbf{x}} - \left(\frac{\lambda_1}{\sqrt{\lambda_1^2 + 3\lambda_2^2}} - \frac{1}{2} \right) \hat{\mathbf{y}} \otimes \hat{\mathbf{y}}. \quad (\text{S26})$$

For small pure shear deformations, $\lambda_1 = 1 + \varepsilon$ and $\lambda_2 = 1 - \varepsilon$ with $\varepsilon \ll 1$, we find that

$$\mathbf{W} \approx \frac{\sqrt{3}}{2} \mathbf{I} + \sqrt{3}\varepsilon(\hat{\mathbf{x}} \otimes \hat{\mathbf{x}} - \hat{\mathbf{y}} \otimes \hat{\mathbf{y}}), \quad (\text{S27})$$

while

$$\mathbf{Q} \approx \frac{3}{4}\varepsilon(\hat{\mathbf{x}} \otimes \hat{\mathbf{x}} - \hat{\mathbf{y}} \otimes \hat{\mathbf{y}}). \quad (\text{S28})$$

Thus, we find that, at first order in the pure shear amplitude,

$$\boldsymbol{\sigma}^{(\text{active})} \approx \frac{\sqrt{3}\zeta}{2} \mathbf{I} + \frac{4\sqrt{3}\zeta}{3} \mathbf{Q}. \quad (\text{S29})$$

Comparing it to Eq. (S11) and taking $A_J = A_0$ and $P_J = P_0$, we get relationships between the contractility activity parameter ζ , α_J and χ_J :

$$\begin{cases} \alpha_J \approx -\frac{\sqrt{3}}{6}\zeta \\ \chi_J \approx \frac{8\sqrt{3}}{3} \frac{A_0}{P_0} \zeta \end{cases} \quad (\text{S30})$$

We, therefore, expect that the forces defined in Eq. (S22) can be recast into the formalism of Eq. (S11): an increase in the contractility parameter ζ then maps into a decrease in α and an increase in χ ; a sufficiently large increase in ζ thus can trigger a transition from a liquid to a solid regime, see Fig. S2(a) and Fig. S3(c).

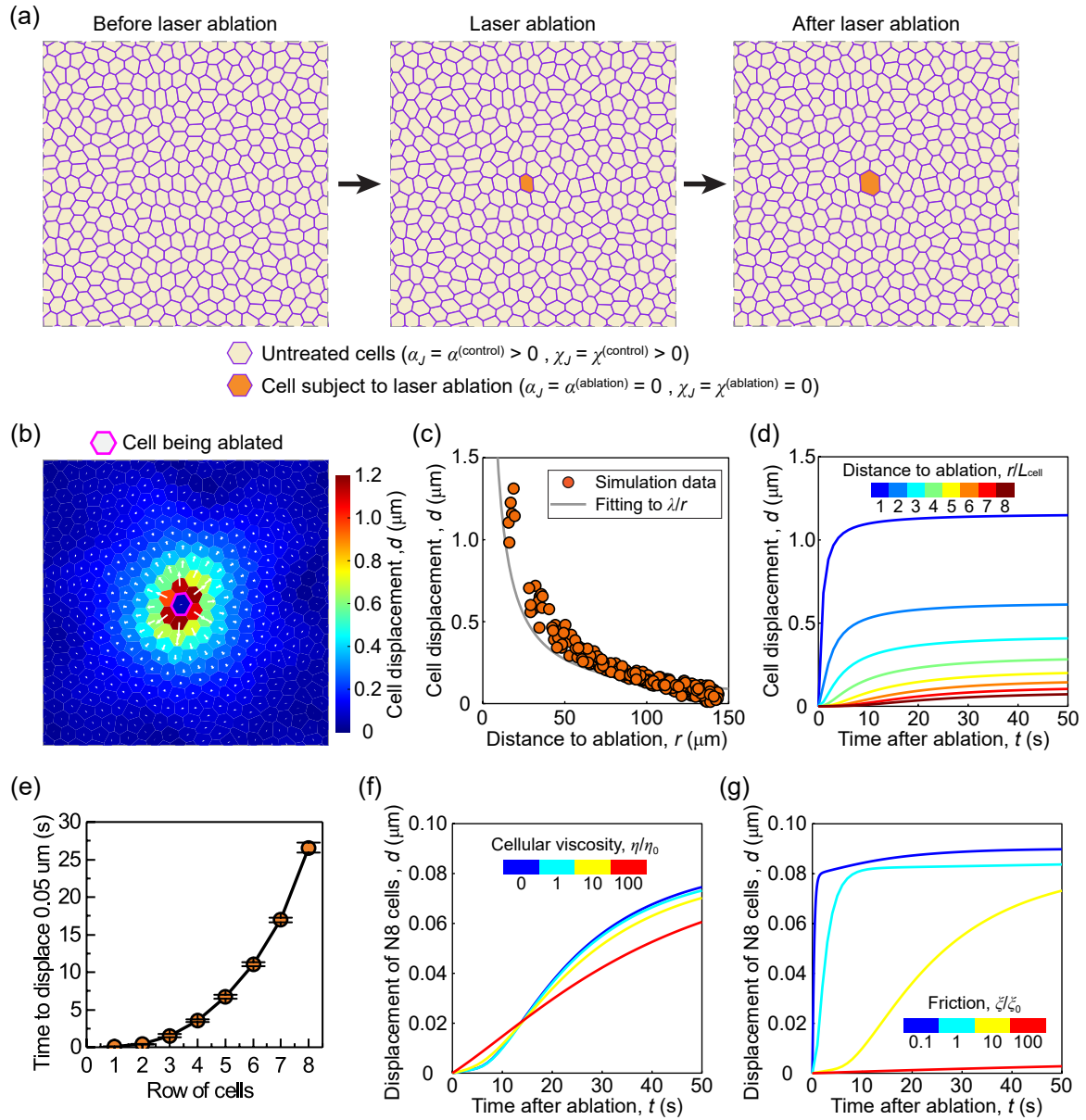


Figure S4: **Simulation 1: the laser ablation of an actin star node.** (a) Sketch of the active vertex model to simulate the laser ablation response of an intestinal epithelial monolayer. Vertex model description of an intestinal epithelial cell monolayer by a two-dimensional tiling of polygons. To mimic the effect of laser ablation, we set the activity of the cell being ablated to zero (i.e., $\alpha_J = 0$ and $\chi_J = 0$). (b-f) Simulation results of the laser ablation response of an intestinal epithelial monolayer. (b) The displacement of cells at time $t = 50$ s in response to the laser ablation (applied at $t = 0$). The color code represents the magnitude of cell displacement, while the white arrows refer to the cell displacement vector. The cell being ablated is marked by the magenta contour. (c) Scatter plot of the cell displacement magnitude as a function of the distance of the cell center to the ablation site. Symbols: simulation data. Gray solid line: fitting to λ/r with $\lambda = 13.5 \mu\text{m}^2$ fitted by the least squares method. (d) The average displacement magnitude of cells at the k -th row as a function of time t after ablation. The cells at the k -th row are defined by the distance d of the cell center to the ablation site if it satisfies $k - 1/2 < d/L_{\text{cell}} < k + 1/2$ with $L_{\text{cell}} = 10 \mu\text{m}$ being the cell size. (e) Time to displace $0.05 \mu\text{m}$, $t_{0.05 \mu\text{m}}$, as a function of the row of cells (i.e., distance to the laser ablation site). Averaged over $n = 5$ independent simulations. Data = mean \pm SD. (f) The average displacement magnitude of cells at the 8-th row (denoted N8 cells) as a function of time t after ablation, for different levels of cellular viscosities expressed in the unit of $\eta_0 = 0.01 \text{ nN} \cdot \text{s} \cdot \mu\text{m}^{-1}$, with fixed friction $\xi = 0.1 \text{ nN} \cdot \text{s} \cdot \mu\text{m}^{-1} = 10\eta_0$; (g) The average displacement magnitude of cells at the 8-th row (denoted N8 cells) as a function of time t after ablation, for different levels of friction expressed in units of $\xi_0 = 0.01 \text{ nN} \cdot \text{s} \cdot \mu\text{m}^{-1}$, with fixed cellular viscosity $\eta = 0.01 \text{ nN} \cdot \text{s} \cdot \mu\text{m}^{-1} = \xi_0$. Other parameters are set in Table I.

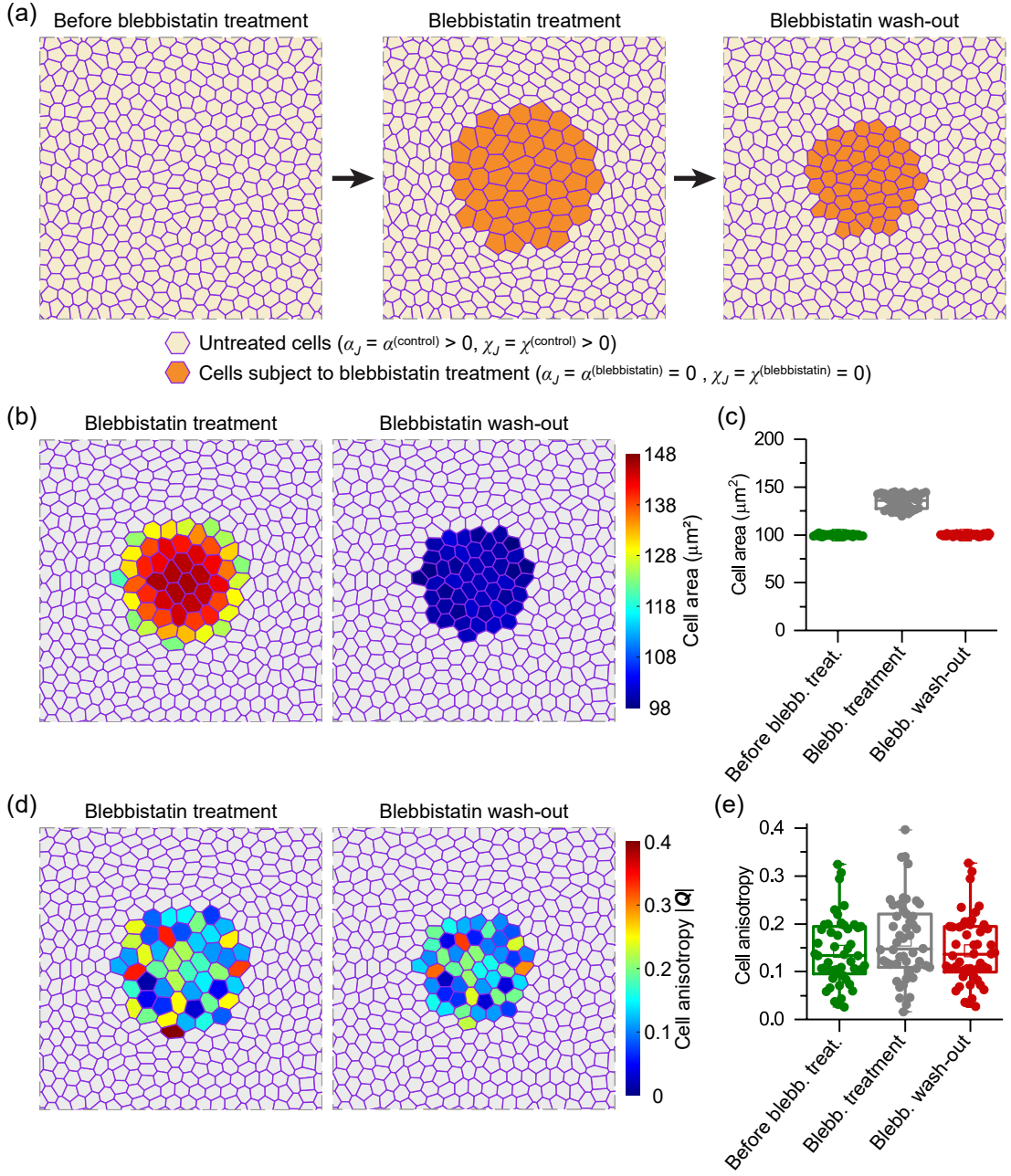


Figure S5: **Simulation 2: contractility recovery by blebbistatin wash-out.** (a) Sketch of the active vertex model to simulate the effect of blebbistatin treatment and the subsequent contractility recovery process by blebbistatin wash-out. The blebbistatin treatment is mimicked by a decrease in the contractility activity of the actin star network within the cells being treated. The blebbistatin wash-out effect is mimicked by recovering the contractility activity with the cells being treated. (b-e) Simulation results. (b) The cell area field after blebbistatin treatment (*left*) and the cell area field after blebbistatin wash-out (*right*). Here, we show the area of cells being treated. (c) Statistical analysis of cell area before blebbistatin treatment, after blebbistatin treatment, and after blebbistatin wash-out. The cell area are $99.8 \pm 1.0 \mu\text{m}^2$ (mean \pm S.D.), $134.1 \pm 7.7 \mu\text{m}^2$ (mean \pm S.D.) and $99.9 \pm 1.0 \mu\text{m}^2$, in turn. $n = 50$ cells. (d) The cell anisotropy field after blebbistatin treatment (*left*) and the cell area field after blebbistatin wash-out (*right*). Here, we show the anisotropy of cells being treated. (e) Statistical analysis of cell anisotropy before blebbistatin treatment, after blebbistatin treatment, and after blebbistatin wash-out. The cell anisotropy are $0.142 \pm 0.070 \mu\text{m}^2$ (mean \pm S.D.), $0.165 \pm 0.084 \mu\text{m}^2$ (mean \pm S.D.) and $0.143 \pm 0.070 \mu\text{m}^2$, in turn. $n = 50$ cells. Simulation parameters are provided in Table II.

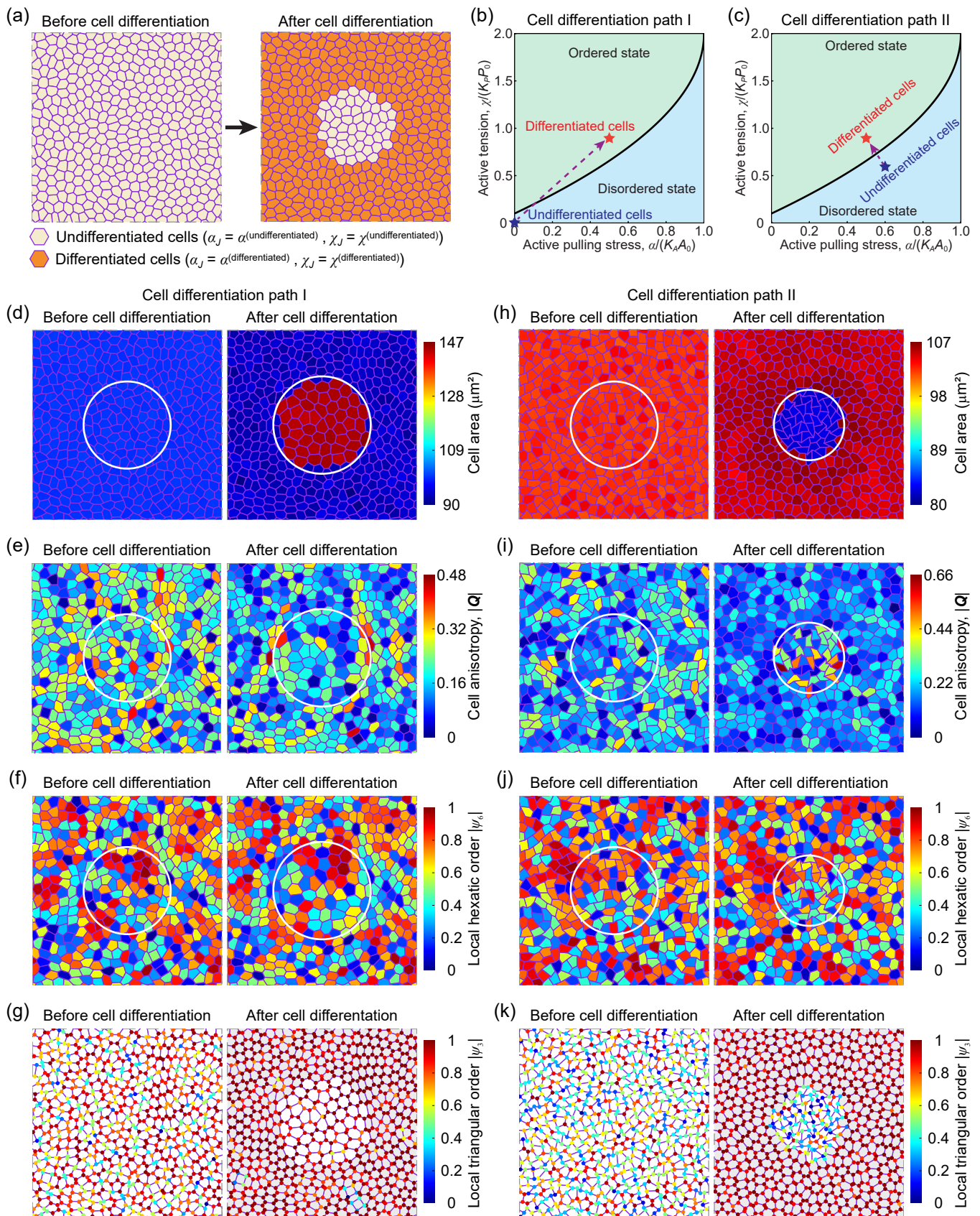


Figure S6: (Caption on the next page.)

Figure S6: (Previous page.) **Simulation 3: cell differentiation from crypt-like cells to villus-like cells.** (a) Sketch of the active vertex model to simulate the process of cell differentiation from crypt-like cells (light yellow) to villus-like cells (orange). Initially, cells are all the same. We mimic the cell differentiation effect by selecting a group of cells and setting up a different level of activity. (b, c) Two possible cell differentiation paths in the (α, χ) space. (d-k) Simulation results of (d, h) the cell area field, (e, i) the anisotropy field, (f, j) the local hexatic order parameter field, and (g, k) the local triangular order parameter field (*left*) before and (*right*) after cell differentiation. Here, the cell anisotropy is quantified by the magnitude of the anisotropic cell shape tensor $|\mathbf{Q}|$. In (g, k), differentiated cells are marked as grey. Results (d-g) correspond to the path shown in (b); while results (h-k) correspond to the path shown in (c). Parameter values used in such simulations are given in Table III and IV.

TABLE I: List of default parameter values used in our simulation 1 of laser cell ablation, Sec. IC1.

Parameter	Description	Value
$\ell = \sqrt{A_0}$	Length scale	10 μm
τ	Time scale	0.1 s
$f = K_A A_0^{3/2}$	Force scale	1 nN
K_A	Cell area stiffness	$10^6 \text{ N} \cdot \text{m}^{-3}$
A_0	Preferred cell area	100 μm^2
K_P	Cell perimeter stiffness	$0.002 \text{ nN} \cdot \mu\text{m}^{-1}$
P_0	Preferred cell perimeter	40 μm
ξ	Cell-substrate friction	$0.1 \text{ nN} \cdot \text{s} \cdot \mu\text{m}^{-1}$
η	Viscosity of cells	$0.01 \text{ nN} \cdot \text{s} \cdot \mu\text{m}^{-1}$
$\alpha^{(\text{control})}$	Active pulling stress level of control cells	$0.05 \text{ nN} \cdot \mu\text{m}^{-1}$
$\alpha^{(\text{ablation})}$	Active pulling stress level of the ablated cell	0
$\chi^{(\text{control})}$	Active tension level of control cells	0.064 nN
$\chi^{(\text{ablation})}$	Active tension level of the ablated cell	0
Δt	Simulation time step	0.001 s

TABLE II: List of default parameter values used in simulation 2, contractility recovery, Sec. IC2.

Parameter	Description	Value
$\ell = \sqrt{A_0}$	Length scale	10 μm
τ	Time scale	0.1 s
$f = K_A A_0^{3/2}$	Force scale	1 nN
K_A	Cell area stiffness	$10^6 \text{ N} \cdot \text{m}^{-3}$
A_0	Preferred cell area	100 μm^2
K_P	Cell perimeter stiffness	$0.002 \text{ nN} \cdot \mu\text{m}^{-1}$
P_0	Preferred cell perimeter	40 μm
ξ	Cell-substrate friction	$0.1 \text{ nN} \cdot \text{s} \cdot \mu\text{m}^{-1}$
η	Viscosity of cells	$0.01 \text{ nN} \cdot \text{s} \cdot \mu\text{m}^{-1}$
$\alpha^{(\text{blebbistatin})}$	Active pulling stress level of cells after blebbistatin treatment	0
$\alpha^{(\text{control})}$	Active pulling stress level of cells before blebbistatin treatment or after blebbistatin wash-out	$0.05 \text{ nN} \cdot \mu\text{m}^{-1}$
$\chi^{(\text{blebbistatin})}$	Active tension level of cells after blebbistatin treatment	0
$\chi^{(\text{control})}$	Active tension level of cells before blebbistatin treatment or after blebbistatin wash-out	0.064 nN
Δt	Simulation time step	0.001 s

TABLE III: List of default parameter values used in simulation 3, cell differentiation (path I), Sec. IC3.

Parameter	Description	Value
$\ell = \sqrt{A_0}$	Length scale	10 μm
τ	Time scale	0.1 s
$f = K_A A_0^{3/2}$	Force scale	1 nN
K_A	Cell area stiffness	$10^6 \text{ N} \cdot \text{m}^{-3}$
A_0	Preferred cell area	100 μm^2
K_P	Cell perimeter stiffness	$0.002 \text{ nN} \cdot \mu\text{m}^{-1}$
P_0	Preferred cell perimeter	40 μm
ξ	Cell-substrate friction	$0.1 \text{ nN} \cdot \text{s} \cdot \mu\text{m}^{-1}$
η	Viscosity of cells	$0.01 \text{ nN} \cdot \text{s} \cdot \mu\text{m}^{-1}$
$\alpha^{(\text{undifferentiated})}$	Active pulling stress level of undifferentiated cells (crypt-like cells)	0
$\alpha^{(\text{differentiated})}$	Active pulling stress level of differentiated cells (villus-like cells)	$0.05 \text{ nN} \cdot \mu\text{m}^{-1}$
$\chi^{(\text{undifferentiated})}$	Active tension level of undifferentiated cells (crypt-like cells)	0
$\chi^{(\text{differentiated})}$	Active tension level of differentiated cells (villus-like cells)	0.064 nN
Δt	Simulation time step	0.001 s

TABLE IV: List of default parameter values used in simulation 3, cell differentiation (path II), Sec. IC3.

Parameter	Description	Value
$\ell = \sqrt{A_0}$	Length scale	10 μm
τ	Time scale	0.1 s
$f = K_A A_0^{3/2}$	Force scale	1 nN
K_A	Cell area stiffness	$10^6 \text{ N} \cdot \text{m}^{-3}$
A_0	Preferred cell area	100 μm^2
K_P	Cell perimeter stiffness	$0.002 \text{ nN} \cdot \mu\text{m}^{-1}$
P_0	Preferred cell perimeter	40 μm
ξ	Cell-substrate friction	$0.1 \text{ nN} \cdot \text{s} \cdot \mu\text{m}^{-1}$
η	Viscosity of cells	$0.01 \text{ nN} \cdot \text{s} \cdot \mu\text{m}^{-1}$
$\alpha^{(\text{undifferentiated})}$	Active pulling stress level of undifferentiated cells (crypt-like cells)	$0.06 \text{ nN} \cdot \mu\text{m}^{-1}$
$\alpha^{(\text{differentiated})}$	Active pulling stress level of differentiated cells (villus-like cells)	$0.05 \text{ nN} \cdot \mu\text{m}^{-1}$
$\chi^{(\text{undifferentiated})}$	Active tension level of undifferentiated cells (crypt-like cells)	0.056 nN
$\chi^{(\text{differentiated})}$	Active tension level of differentiated cells (villus-like cells)	0.064 nN
Δt	Simulation time step	0.001 s

-
- [1] T. Nagai and H. Honda, *Philosophical Magazine B* **81**, 699 (2001).
 - [2] R. Farhadifar, J. C. Röper, B. Algouy, S. Eaton, and F. Jülicher, *Current Biology* **17**, 2095–2104 (2007).
 - [3] S. Alt, P. Ganguly, and G. Salbreux, *Philosophical Transactions of the Royal Society B: Biological Sciences* **372**, 20150520 (2017).
 - [4] C. Fu, F. Dilasser, S.-Z. Lin, M. Karnat, A. Arora, H. Rajendiran, H. T. Ong, N. M. H. Brenda, S. W. Phow, T. Hirashima, M. Sheetz, J.-F. Rupprecht, S. Tlili, and V. Viasnoff, *bioRxiv*, 2023.12.04.570034 (2024).
 - [5] A. G. Fletcher, M. Osterfield, R. E. Baker, and S. Y. Shvartsman, *Biophysical Journal* **106**, 2291–2304 (2014).
 - [6] D. Bi, J. Lopez, J. Schwarz, and M. L. Manning, *Nature Physics* **11**, 1074–1079 (2015).
 - [7] S.-Z. Lin, S. Ye, G.-K. Xu, B. Li, and X.-Q. Feng, *Biophysical Journal* **115**, 1826 (2018).
 - [8] S.-Z. Lin, M. Merkel, and J.-F. Rupprecht, *Physical Review Letters* **130**, 058202 (2023).
 - [9] G. Batchelor, *Journal of Fluid Mechanics* **41**, 545 (1970).
 - [10] A. W. C. Lau and T. C. Lubensky, *Physical Review E* **80**, 011917 (2009).
 - [11] S.-Z. Lin, M. Merkel, and J.-F. Rupprecht, *The European Physical Journal E* **45**, 4 (2022).
 - [12] S. Sonam, L. Balasubramaniam, S.-Z. Lin, Y. M. Y. Ivan, I. Pi-Jaumà, C. Jebane, M. Karnat, Y. Toyama, P. Marcq, J. Prost, *et al.*, *Nature Physics* **19**, 132 (2023).
 - [13] A. Nestor-Bergmann, G. Goddard, S. Woolner, and O. E. Jensen, *Mathematical Medicine and Biology: A Journal of the IMA* **35**, i1 (2018).
 - [14] K. Bambardekar, R. Clément, O. Blanc, C. Chardès, and P.-F. Lenne, *Proceedings of the National Academy of Sciences of the United States of America* **112**, 1416 (2015).